Electron Spectroscopy Using Metastable Atoms as Probes for Solid Surfaces

Yoshiya Harada,*,† Shigeru Masuda,‡ and Hiroyuki Ozaki§

Department of Materials Science, Faculty of Engineering, Chiba University, Inage, Chiba 263, Japan, Department of Chemistry, Graduate School of Arts and Sciences, University of Tokyo, Komaba, Meguro, Tokyo 153, Japan, and Department of Material Systems Engineering, Faculty of Technology, Tokyo University of Agriculture and Technology, Koganei, Tokyo 184, Japan

Received July 16, 1996 (Revised Manuscript Received April 29, 1997)

Contents

I. Introduction

When a slow, rare gas, metastable atom, a long-lived, electronically excited atom, is introduced onto a solid surface, most of its excitation energy is used to eject electrons from the surface. Since the rare gas atom usually does not react on the solid surface, the kinetic energy distribution of ejected electrons, which is called metastable atom electron spectrum in this review, contains the information on the electronic state of the solid surface. Unlike photons or electrons used for ordinary electron spectroscopies such as photoelectron spectroscopy (PES), Auger electron spectroscopy (AES), electron energy loss spectroscopy (EELS), etc., metastable atoms do not penetrate into the bulk of the solid. Metastable atom electron spectroscopy (MAES), therefore, probes the outermost surface layer selectively. Further, MAES is essentially nondestructive, because metastable atoms are usually introduced only with thermal kinetic energies. The fact that metastable atoms deexcite with nearly unit probability at solid surfaces (cf., section III.B.1) also makes MAES useful for surface analysis.

In this review we discuss the interaction between the metastable atom and solid surface, focusing primarily on the unique characteristics of MAES when applied to various clean and adsorbed surfaces. The MAES of liquid samples will be described briefly in connection with the solid MAES. Table 1 lists some characteristics of rare gas metastable atoms together with the energies of resonance lines used as excitation sources for ultraviolet photoelectron spectroscopy (UPS).

Historically, the ionization process due to the collisions between target atoms T and metastable atoms A*:

$$T + A^* \rightarrow T^+ + A + e^- \quad \text{Penning ionization} \quad (1)$$

was suggested by Penning in 1927, when he was studying discharge phenomena in rare gases.[1] An energy analysis of electrons ejected through reaction 1 was initiated by Čermák[2] and is now called Penning

† Chiba University.
‡ University of Tokyo.
§ Tokyo University of Agriculture and Technology.

S0009-2665(94)00315-8 CCC: $28.00

Yoshiya Harada was born in Bofu, Japan, in 1934. He received his B.S., M.S., and Ph.D. degrees in chemistry at the University of Tokyo. He was a Research Associate at Institute for Solid State Physics, the University of Tokyo, from 1961 to 1969. He was appointed Associate Professor in 1969 and Professor in 1983 at College of Arts and Sciences, the University of Tokyo. He received the 1984 Chemical Society of Japan Award in physical chemistry. In 1994 he moved to Chiba University, where he is currently a Professor of the Faculty of Engineering. His research interests center on the electronic structure and electron spectroscopy of solid surfaces.

Shigeru Masuda was born in 1955 in Kakogawa, Japan, and graduated from Kobe University in 1977. He received his Master's and Ph.D. degrees from Kyoto University in 1980 and 1983, respectively. After a year postdoctoral stay in Kyoto University, he became a Research Associate at the University of Tokyo in 1984 and was promoted to Associate Professor in 1994. He has been the recipient of the 1994 Award for young chemist of Silicon Photochemical Society of Japan. His research interests cover surface science, especially the metastable atom–surface interactions.

ionization electron spectroscopy (PIES). Since Čermák's work, PIES has been extensively applied to study the electronic states of various atoms and molecules as well as their interactions with rare gas atoms (in the following the abbreviations, MAES, PIES, and UPS, will be used to stand for the electron spectroscopies as well as for the electron spectra). As for the Penning ionization and related phenomena of atoms and molecules, several reviews are available.[3−13]

The electron ejection from the solid by impact of metastable atoms was observed prior to Penning's work described above. In 1924 Webb found electron emission from a nickel plate by impact of mercury metastable atoms produced in an electrode tube containing mercury vapor.[14] Later Oliphant first measured the velocity distribution of electrons ejected from metals by metastable helium atoms.[15] Further investigations on the electron emission from

Hiroyuki Ozaki was born in 1959 in Ueda, Japan, but was educated in Urawa, Japan, where he received his B.S. degree from Saitama University. He received M.S. and Ph.D. degrees in Penning spectroscopy of organic surfaces at the University of Tokyo. During 1987–1991 he was a Research Associate at Nagoya University. Since 1991, he has been an Assistant Professor at Tokyo University of Agriculture and Technology. His research interests include the electronic structure, aggregation, and behavior of organic molecules in extrathin films as well as construction of superstructure by surface reactions.

metals[16−22] did not provide clear conclusions, owing to the inadequate data analyses and the use of contaminated surfaces. In the period between 1975 and 1983 a number of groups started the measurement of the MAES that could be compared with UPS and obtained meaningful results for clean and adsorbed surfaces.[23−27] Now MAES has been established as one of the most surface-sensitive methods and is being applied to the study of the electronic states of various solid and liquid surfaces.

As will be described in section III.B.1, on the solid surface rare gas metastable atoms deexcite through resonance ionization (RI) followed by Auger neutralization (AN)[28] in addition to direct Penning ionization (PI):

$$T + A^* \rightarrow T^- + A^+ \quad \text{resonance ionization} \tag{2}$$

$$T^- + A^+ \rightarrow T^+ + A + e^- \quad \text{Auger neutralization} \tag{3}$$

The RI+AN process proceeds at the surfaces of ordinary metals and semiconductors. In RI the electron in the outer orbital of the metastable atom tunnels into an empty level of the surface. The positive ion thus formed is then neutralized through AN, in which an electron in the solid transfers to the vacant inner orbital of the ion and another electron in the solid is ejected. When an empty level of the surface is not present opposite to the outer level of the metastable atom as in the case of insulators, the metastable atom is deexcited through PI (or Auger deexcitation (AD)), in which an electron in the solid transfers to the inner vacant orbital of the metastable atom and the electron of the outer orbital is ejected. (The PI of gas-phase molecules also corresponds to Auger process (cf., section III.A).) (It should be noted that under special conditions, i.e., for samples with very low work function, a third channel via negative ion formation may come into play[29] as outlined in section III.B.3.) In this review we use MAES as a general term for electron spectroscopy due to metastable atoms. Therefore, MAES of solids refers to the

Table 1. Characteristics of Metastable Rare Gas Atoms Together with the Energies of Resonance Lines Used for UPS[a]

atom	state	excitation energy, eV	ionization energy, eV	life time, s	polarizability, Å^3		energy, eV
He(1s2s)	2^1S	20.616	3.972	1.97×10^{-2} [b]	118.9[c]	He I	21.218
	2^3S	19.820	4.768	9.0×10^{3} [d]	46.9[c]		
Ne($2p^5 3s$)	$^3P_0$	16.715	4.849	4.3×10^{2} [e]		Ne I	16.848
	$^3P_2$	16.619	4.945	2.4×10^{1} [e]	27.8[f]		16.671
Ar($3p^5 4s$)	$^3P_0$	11.723	4.036	4.5×10^{1} [e]		Ar I	11.828
	$^3P_2$	11.548	4.211	5.6×10^{1} [e]	47.9[f]		11.623
Kr($4p^5 5s$)	$^3P_0$	10.562	3.437	4.9×10^{-1} [e]		Kr I	10.643
	$^3P_2$	9.915	4.084	8.5×10^{1} [e]	50.7[f]		10.032
Xe($5p^6 6s$)	$^3P_0$	9.447	2.683	7.8×10^{-2} [e]		Xe I	9.447
	$^3P_2$	8.315	3.815	1.5×10^{2} [e]	63.6[f]		8.436

[a] Refer to refs 7 and 78 for other metastable states of atoms and molecules used for collision experiments. [b] Van Dyck, R. S., Jr.; Johnson, C. E.; Shugart, H. A. *Phys. Rev. Lett.* **1970**, *25*, 1403; *Phys. Rev.* **1971**, *A4*, 1327; **1972**, *A5*, 991. [c] Victor, G. A.; Dalgarno, A.; Taylor, A. J. *J. Phys.* **1968**, *B1*, 13. [d] Woodworth, J. R.; Moos, H. W. *Phys. Rev.* **1975**, *A12*, 2455. [e] Small-Warren, N. E.; Chiu, L.-C. Y. *Phys. Rev.* **1975**, *A11*, 1777. [f] Molof, R. A.; Schwartz, H. L.; Miller, T. M.; Bederson, B. *Phys. Rev.* **1974**, *A10*, 1131.

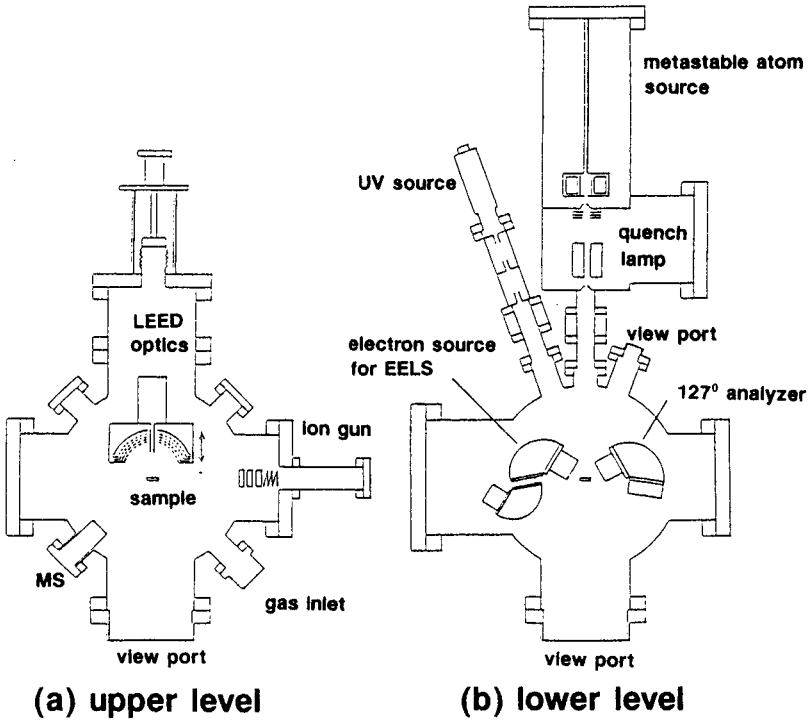

Figure 1. Schematic diagram of an apparatus for MAES, UPS, and HREELS. (Reprinted with permission from ref 41. Copyright 1990 Elsevier.)

energy analysis of electrons ejected through RI+AN or PI (AD) process. MAES is a term after the particle used for electron ejection as in photoelectron spectroscopy. Other workers use different terms like metastable deexcitation spectroscopy (MDS),[25,30] metastable quenching spectroscopy (MQS),[27] or metastable impact electron spectroscopy (MIES).[31]

In this review we discuss the experimental methods for surface MAES in section II and the deexcitation process of the metastable atom in section III. Sections IV and V cover studies on inorganic and organic surfaces, respectively. In section VI we give a new topic, the observation of surface topology. Finally section VII contains our conclusions. We wish to warrant that this review is complete up to the end of 1995, but must warn the reader that some newly developing work may have escaped notice. As for earlier reviews of the MAES of solids the reader should refer to literatures.[32−36]

II. Experimental Methods

In this section the experimental methods for measuring metastable atom electron spectra (MAES) of solids will be briefly described. The apparatus for MAES is essentially the same as that for UPS except that a light source for UPS is replaced by a metastable atom source.[27,35,37−44] Figure 1 shows an example of the surface analysis system equipped with an MAES and a UPS source.[41] The main chamber (base pressure, $\sim 6 \times 10^{-11}$ Torr) has two levels: An optics for low-energy electron diffraction (LEED) and Auger electron spectroscopy (AES), an Ar^+ ion gun, and a quadrupole mass filter are on the upper level, while a monochromatic electron source for electron energy loss spectroscopy (EELS) and a 127°-type electron energy analyzer commonly used for MAES, UPS, and EELS are on the lower level, being mounted on a rotatable base. The position of the sample is adjusted by a precision manipulator. For the mea-

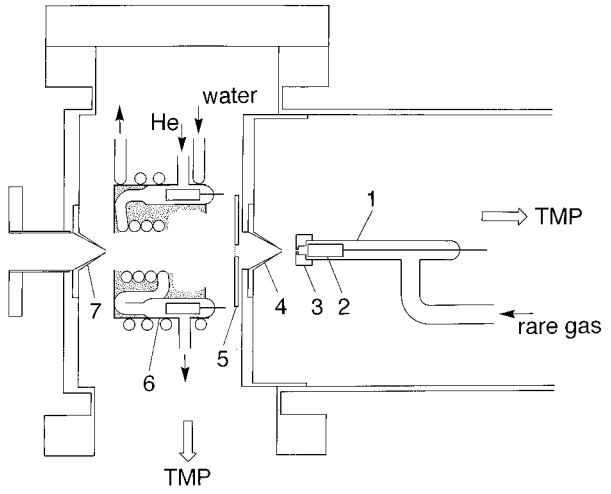

Figure 2. Metastable atom source: (1) Pyrex tube, (2) tantalum cathode, (3) boron nitride nozzle, (4) skimmer, (5) repeller grid, (6) quench lamp, and (7) skimmer.

surement of liquid samples a special liquid inlet system has been devised.[45,46]

Rare gas metastable beams are usually produced by three types of source, electron bombardment and cold and hot discharge types.[6,7] In metastable helium operation cold and hot cathode discharges give mainly He*(2^3S) species, while electron bombardment produces some amount of He*(2^1S), whose intensity depends on the collision energy of electrons. Figure 2 shows a cold cathode discharge source,[47] originally designed by Leasure et al.[48] and Fahey et al.[49] The discharge is maintained between a tantalum hollow cathode 2 and stainless-steel skimmer 4 across a pressure gradient created by differential pumping. Electrons due to discharge are removed with a repeller grid 5. For the measurement of He*(2^3S) spectra, He*(2^1S) atoms are quenched via the transition of $2^1S \rightarrow n^1P \rightarrow 1^1S$ ($n = 2, 3, 4$, etc.) with the light from a helium discharge lamp 6. More than 99% of the He*(2^1S) atoms are quenched with this type of lamp.[7,50]

The He*(2^1S) spectrum can be derived by taking the difference of the two spectra obtained with the quench lamp on and off. With the use of a high-speed pumping system (3000 L s^{-1} for the discharge-lamp chamber, 330 L s^{-1} for the quench-lamp chamber) the discharge source gives very high flux beam of the order of 10^{16} atoms s^{-1} sr^{-1} and is used as a metastable source for an electron emission microscope (cf., section VI).

Recently MAES using spin-polarized metastable atoms has been developed by Dunning and his collaborators, who named the method SPMDS (spin-polarized metastable-atom deexcitation spectroscopy).[51] Their apparatus is shown in Figure 3.[52] A ground-state helium beam formed by a multichannel array is partly excited to the 2^1S and 2^3S states by a coaxial electron gun, which utilizes a solenoid to focus impact electrons. A mechanical chopper is used, in combination with time-of-flight techniques, to eliminate effects due to electron ejection by photons and fast ground state atoms that might be contained in the metastable beam. The 2^1S atoms and charged particles produced by electron impact are removed by a helium discharge lamp and deflection plates, respectively. A weak (~0.5 G) magnetic field is applied perpendicular to the beam to establish a quantization axis. Circularly polarized radiation ($2^3P \rightarrow 2^3S$, 1.08 μm) obtained by passing the light of an rf-excited He lamp through a polarizer and a quarter wave plate are used to optically pump the 2^3S atoms to increase the relative populations in the $M_s = +1$, or -1 magnetic sublevels (the $M_s = +1$ and -1 sublevels are populated by right-hand and left-hand circularly polarized radiations, respectively).[53] The beam polarization is defined by

$$P_z = \frac{n_+ - n_-}{n_+ + n_0 + n_-} \tag{4}$$

where n_+, n_0, and n_- are numbers of atoms in the $M_s = +1$, 0, and -1 sublevels, respectively. The value of P_z is measured by a Stern–Gerlach analyzer[53] and is about 0.45.[54] The MAES of a sample is measured by a retarding-potential analyzer.

The polarizations of ejected electrons are measured using a Mott polarimeter,[55,56] which detects the left–right scattering asymmetry produced as a result of spin–orbit coupling when high-energy electrons are scattered from the nuclei in a target metal. The polarimeter includes a retarding-potential energy analyzer, which enables energy-resolved measurements. The electron polarization is defined as

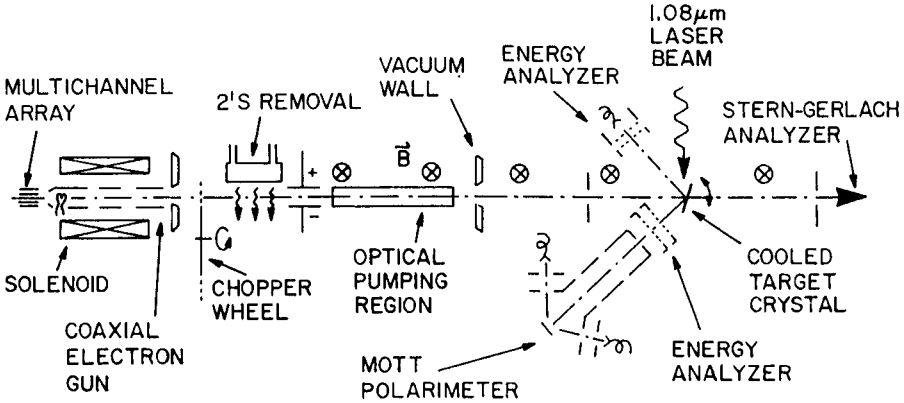

Figure 3. Schematic diagram of an apparatus for spin-polarized MAES. A Ti:sapphire laser (1.08 μm) is used to produce He*(2^3P, 20.96 eV) atoms by illuminating the 2^3S beam at the target surface. (Reprinted with permission from ref 52. Copyright 1994 The American Physical Society.)

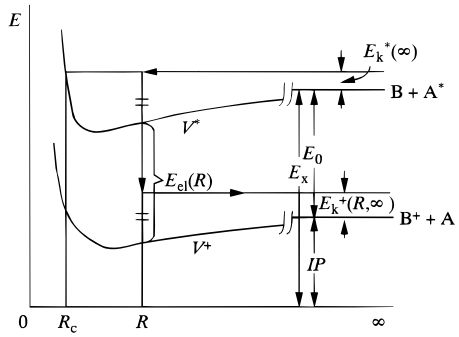

Figure 4. Potential curve model of Penning ionization: $B + A^* \rightarrow B^+ + A + e^-$.

$$P = \frac{n_\uparrow - n_\downarrow}{n_\uparrow + n_\downarrow} \tag{5}$$

where $n_\uparrow$ and $n_\downarrow$ are the numbers of electrons with spin up ($m_s = {}^1/_2$) and spin down ($m_s = -{}^1/_2$), respectively.

III. Deexcitation Process of Metastable Atoms

A. Deexcitation in Collision with Atoms or Molecules

In this section we first describe the deexcitation process of metastable atoms colliding with atoms and molecules. The process of Penning ionization can be analyzed on the basis of a potential curve model,[4,6,57,58] which is shown in Figure 4 for an atomic target B. In the figure the excitation energy of a metastable atom A*, E_x, is assumed to be considerably larger than the ionization potential of B, *IP*. Curves *V** and V^+ denote the potential curves for the entrance (B + A*) and exit ($B^+ + A$) channels, respectively. Since the energy of the final state corresponding to the system ($B^+ + A + e^-$) is continuous, having the lower boundary of potential V^+, the transition can occur at all atomic distances larger than that for the classical turning point, R_c. The transition rate $W(R)$ corresponding to the decay of the discrete electronic state into the continuous electronic state degenerate with it is associated with the energy width Γ of *V** by $W(R) = \Gamma(R)/h$. W(R) is roughly an exponential function of R and vanishes at infinite separation.

The separate conservation of the electronic and nuclear energies in the transition at a distance R (Born−Oppenheimer approximation) leads to

$$V^*(R) = E_{el}(R) + V^+(R) \tag{6}$$

or

$$E_{el}(R) = V^*(R) - V^+(R) \tag{7}$$

and

$$E_k^*(\infty) + E_x - V^*(R) = E_k^+(R,\infty) + IP - V^+(R) \tag{8}$$

where $E_{el}(R)$ is the energy of Penning electrons, and $E_k^*(\infty)$ and $E_k^+(R,\infty)$ are the relative kinetic energies between B and A* and between B^+ and A at infinite separations, respectively. Using the "nominal energy" $E_0 = E_x - IP$, eqs 7 and 8 give

$$E_{el}(R) = E_0 - \Delta E(R) \tag{9}$$

and

$$E_k^+(R,\infty) = E_k^*(\infty) + E_0 - E_{el}(R) \tag{10}$$

where

$$\Delta E(R) = (E_x - V^*(R)) - (IP - V^+(R)) \tag{11}$$

From eq 9 it can be seen that the PIES peak exhibits a shift from the nominal energy and also a natural broadening due to the dependence of ΔE on R. Thus, the shift and width of the PIES band contain information on the interparticle potentials, $V^*(R)$ and $V^+(R)$.

In the potential curve model, the potentials, $V^*(R)$ and $V^+(R)$, and the transition rate, $W(R)$, are three basic physical quantities which enable us to provide a complete description of Penning ionization. A quantum mechanical calculation of these quantities, however, has been made only for the simplest systems, such as He* + H[59] and He* + Li.[60,61] Analyses of the PIES of other systems involving atomic and diatomic molecular targets have been made, more or less, semiempirically. For the targets of polyatomic molecules, the above treatment does not seem to be feasible, since three-dimensional and highly anisotropic potential surfaces must be known and collision trajectories are very complex in these cases. Thus, we introduced the following approach for the ionization of polyatomic molecules without taking into account details of the collision trajectories.[12,62,63]

In general, transition probability $W(R)$ is given by

$$W(R) = \frac{2\pi}{\hbar}|T(R)|^2\rho \tag{12}$$

where ρ is the density of the final state and $T(R)$ is the transition matrix element between the initial and final states and is given by

$$T(R) = \langle\Psi_i|H-E|\Psi_f\rangle \tag{13}$$

If we approximate the functions Ψ_i and Ψ_f in terms of antisymmetrized products of orthogonal orbital functions, we have the following expressions for the collision between a closed shell molecule M (MO; ϕ_1, ϕ_2, ..., ϕ_n) and a metastable singlet or triplet atom A* (inner vacant shell AO, χ_a and outer shell AO, χ_b):

$$^{1,3}\Psi_i = \frac{1}{\sqrt{2}}[|\phi_1\bar{\phi}_1 \ldots \phi_i\bar{\phi}_i \ldots \phi_n\bar{\phi}_n\chi_a\bar{\chi}_b| \mp |\phi_1\bar{\phi}_1 \ldots \phi_i\bar{\phi}_i \ldots \phi_n\bar{\phi}_n\bar{\chi}_a\chi_b|] \tag{14}$$

and

$$^{1,3}\Psi_f = \frac{1}{\sqrt{2}}[|\phi_1\bar{\phi}_1 \ldots \phi_i\bar{\psi}_e \ldots \phi_n\bar{\phi}_n\chi_a\bar{\chi}_a| \mp |\phi_1\bar{\phi}_1 \ldots \bar{\phi}_i\psi_e \ldots \phi_n\bar{\phi}_n\chi_a\bar{\chi}_a|] \tag{15}$$

where an electron is removed from MO ϕ_i into a continuum state ψ_e in the final state. From eqs 13−15 $T(R)$ becomes

$$T(R) = \theta J - K \quad (16)$$

in which J and K are Coulomb and exchange-type integrals:

$$J = \int\int \phi_i^*(1)\psi_e(1)\frac{1}{r_{12}}\chi_b^*(2)\chi_a(2)\,d\nu_1\,d\nu_2 \quad (17)$$

$$K = \int\int \phi_i^*(1)\chi_a(1)\frac{1}{r_{12}}\chi_b^*(2)\psi_e(2)\,d\nu_1\,d\nu_2 \quad (18)$$

In eq 16, $\theta = 2$ for the singlet and $\theta = 0$ for the triplet (initial and final) states. For triplet metastable atoms such as He*(2^3S) and Ne*($^3P_0$,$^3P_2$) the J term needs not be considered. Also in general the value of J is very small since χ_a is orthogonal to χ_b. This is supported by the experimental finding that the Penning ionization cross sections for He*(2^3S) and He*(2^1S) are not much different.[4,6] Thus, the transition probability $W_i(R)$ for the ejection of an electron from the MO ϕ_i is given by

$$W_i(R) \propto |K|^2 = |\int\int \phi_i^*(1)\chi_a(1)\frac{1}{r_{12}}\chi_b^*(2)\psi_e(2)\,d\nu_1\,d\nu_2|^2 \quad (19)$$

the value of which depends on the differential overlaps $\phi_i^*(1)\chi_a(1)$ and $\chi_b^*(2)\psi_e(2)$. This is schematically shown in Figure 5, in which an electron in an orbital of M, ϕ_i transfers to the vacant inner orbital of A*, χ_a, and an electron is ejected from the outer orbital of A*, χ_b.[64] Equation 19 indicates that the relative transition probability from MO ϕ_i largely depends on the overlap of the relevant orbital ϕ_i and the inner orbital χ_a. The metastable atom A* can approach up to the repulsive surface of the molecule M, where the distance between A* and M corresponds to that for the classical turning point R_c. If we take into account the localization of the atomic wave functions, χ_a and χ_b, along with the diffuseness of the continuum function ψ_e, the relative transition probability P_i ($W_i(R)$ integrated over all possible R), i.e., the relative band intensity of PIES is considered to be essentially proportional to the exterior electron density (EED) for each MO ϕ_i

$$P_i \propto (EED)_i = \int_\Omega |\phi_i(\boldsymbol{r})|^2\,d\boldsymbol{r} \quad (20)$$

The integration is taken over the region Ω outside the repulsive molecular surface.[12,63] As the repulsive surface we can take a surface estimated from the van der Waals (VDW) radii of the atoms in the molecule. Thus, an outer orbital "exposed" outside the molecular surface (VDW surface) of the molecule gives a larger EED value and, hence, a stronger band in PIES than an inner orbital localized inside the surface (see Figure 6 illustrated for the case of the (M + He*) system). We have successfully applied this feature of PIES to the assignments of UPS bands as well as to the study of the spatial electron distribution of "individual" molecular orbitals in various gas-phase molecules.[10,12] Figure 7 shows the He*(2^3S) PIES of styrene and a theoretical PIES obtained from the Gaussian-type bands with area proportional to the respective EED's.[63] Electron density maps for the π and some σ orbitals are also shown. As can be seen from the figure, the theoretical spectrum well explains the observed ones. The π bands distributed outside the molecule are seen to be clearly distinguished from the other σ bands.

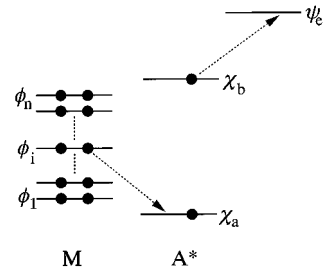

Figure 5. Process of Penning ionization.

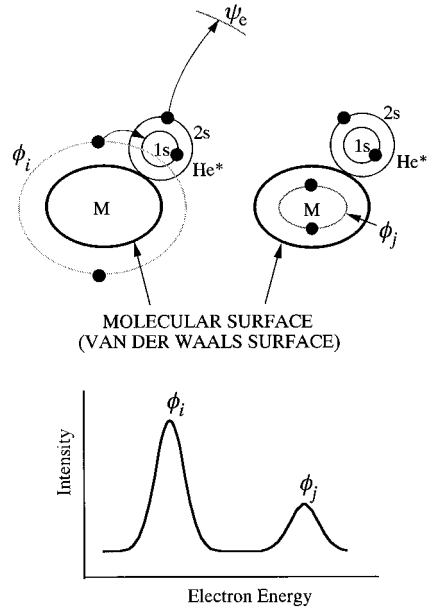

Figure 6. Schematic diagram showing the relation between the distribution of the molecular orbital and the intensity of the corresponding PIES band.

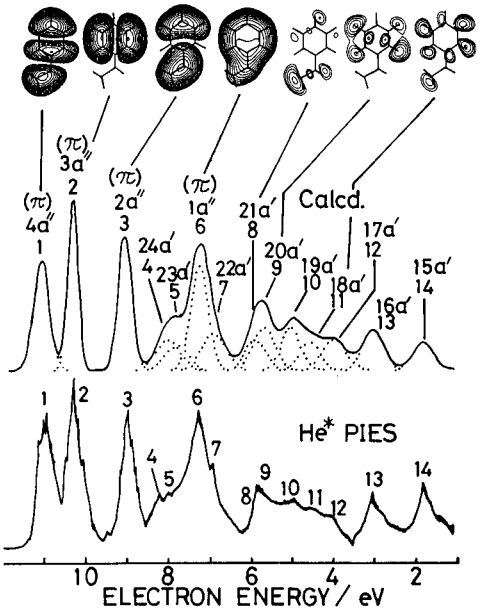

Figure 7. He*(2^3S) PIES and theoretical spectrum for styrene, and electron density maps. The maps are drawn for some MO's for a plane 1.7 Å above the molecular plane. (Reprinted with permission from ref 63. Copyright 1984 The American Physical Society.)

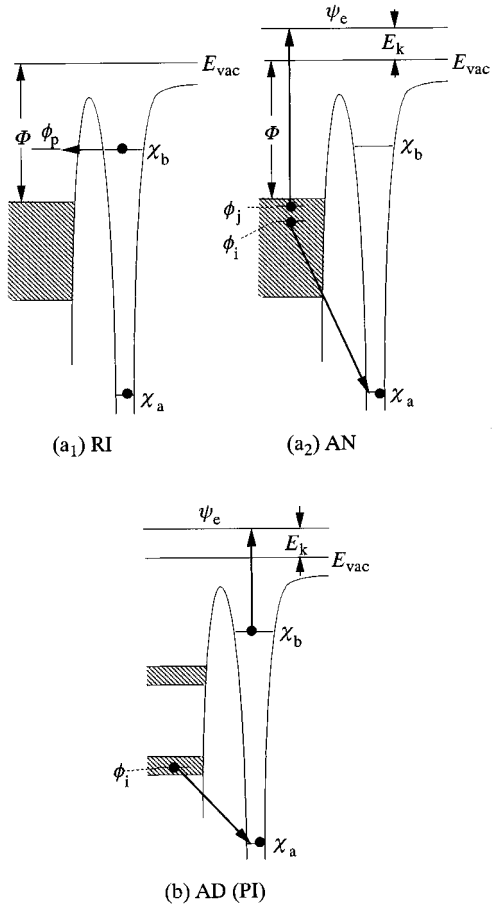

Figure 8. Deexcitation mechanisms of a metastable atom (a_1 and a_2) resonance ionization (RI) followed by Auger neutralization (AN) on a metal surface, and (b) Auger deexcitation (AD) or Penning ionization (PI) on an insulator surface.

B. Deexcitation on Solid Surfaces

1. Deexcitation Process

The deexcitation mechanism of metastable atoms on a solid surface depends on the value of the work function of the solid and also the distribution of the surface orbitals. Figure 8 shows the two types of the deexcitation mechanisms[36,65,66] described in section I. First, on an ordinary metal or semiconductor surface the electron in the outer orbital χ_b of the metastable atom tunnels into an empty level (wave function ϕ_p) of the surface. This process is called resonance ionization (RI, Figure 8a_1). The rate of the RI process at the atom-surface separation R is governed by the square of the overlap integral

$$I(R)_{RI} = \int \phi_p^*(1)\chi_b(1)\, d\nu_1 \qquad (21)$$

The positive ion formed by RI is then neutralized through an Auger process as shown in Figure 8a_2 (Auger neutralization (AN)). In this process an electron (wave function ϕ_i) in the solid loses its energy to fill the vacant inner orbital χ_a of the ion, whereas another electron (wave function ϕ_j) in the solid gains the energy and is ejected from the solid with kinetic energy E_k if it has sufficient momentum normal to the surface. The rate of the AN process is governed by the square of the following matrix (cf., eq 18):

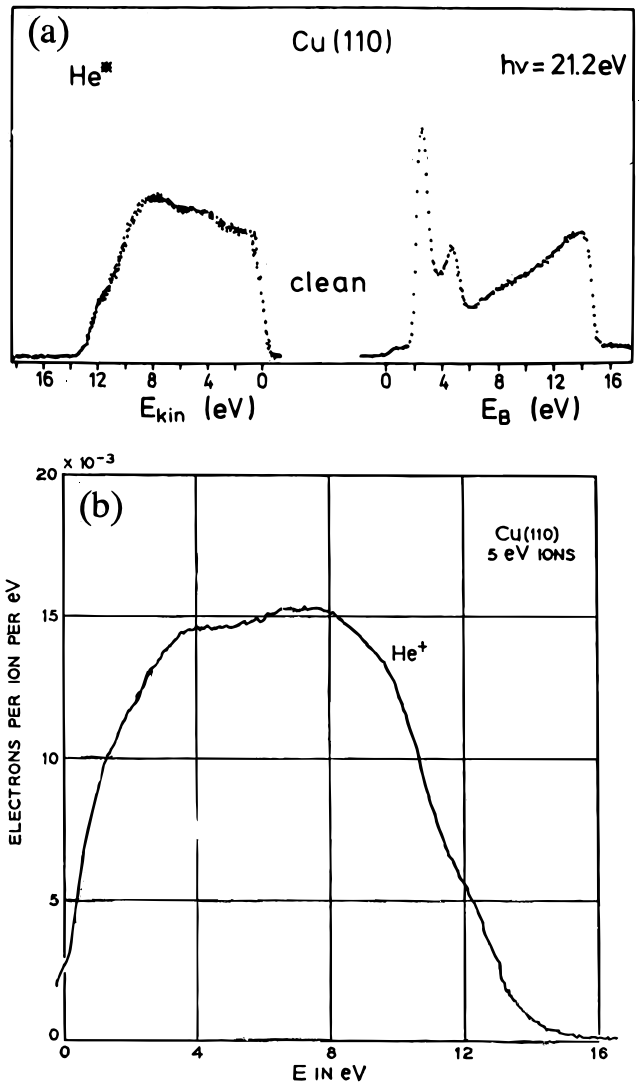

Figure 9. Electron spectra of Cu(110) (a) He*(2^1S) MAES and He I UPS and (b) He^+ INS. (Part a: Reprinted from ref 67. Copyright 1987 American Institute of Physics. Part b: Reprinted with permission from ref 68. Copyright 1966 The American Physical Society.)

$$M_{AN}(R) = \int\int \phi_i^*(1)\chi_a(1)\frac{1}{r_{12}}\phi_j^*(2)\psi_e(2)\, d\nu_1\, d\nu_2 \qquad (22)$$

The AN process also proceeds in ion neutralization spectroscopy (INS),[36,65,66] in which the energy of electrons emitted from solids by impact of rare gas ions is analyzed. Thus, electron spectra of the solid surface due to the RI+AN process give broad self-convoluted features similar to the ion neutralization spectra, because the energy of the rare gas ion formed in the RI process is shared by two electrons in the AN process. Figure 9a shows the He* MAES of a Cu(110) surface compared with the He I UPS.[67] Owing to the RI+AN process the structures in the UPS are smeared out in the MAES, whose shape is seen to be similar to that of the ion neutralization spectrum shown in Figure 9b.[68] Sometimes the deconvolution of AN spectra is carried out to obtain the main features of the surface electronic density of states. The techniques of the deconvolution will be described in section IV.A.1.

The second deexcitation mechanism proceeds on the surfaces of insulators (Figure 8b). In this case,

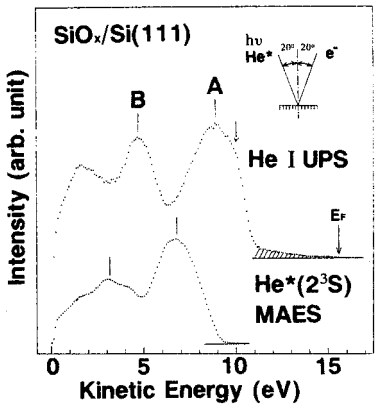

Figure 10. He I UPS and He*(2^3S) MAES of a thin oxide layer (~6 Å) formed on a Si(111)-7×7 surface. The hatched region in the UPS indicates the contribution from the underlying bulk Si. (Reprinted with permission from ref 41. Copyright 1990 Elsevier.)

the RI process is suppressed because an empty level of the solid is absent opposite to the excited level of the metastable atom. Thus, metastable atoms are quenched by Auger deexcitation (AD) or Penning ionization (PI) process, in which an electron (wave function ϕ_i) from the filled band of the solid transfers to the inner orbital χ_a with the simultaneous electron ejection from the outer orbital χ_b (see Figure 8b). For the AD process the matrix element becomes

$$M_{AD}(R) = \int\int \phi_i^*(1)\chi_a(1)\frac{1}{r_{12}}\chi_b^*(2)\psi_e(2)\,d\nu_1\,d\nu_2 \quad (23)$$

Since AD is a process of one-electron transfer from the valence band, the electron spectrum shows the bands corresponding to those of the UPS. Figure 10 shows the He*(2^3S) MAES and He I UPS of an oxide layer (thickness ~6 Å) formed on a Si(111) surface.[41] A good correspondence between the MAES and UPS bands indicates that the oxide layer has an insulating nature, deexciting metastables through the AD process. Note that the UPS gives a weak tail (hatched part) due to the bulk Si while the MAES that probes only the outermost layer does not show such a structure.

In molecular crystals such as organic solids molecules are held together by van der Waals forces. Therefore, the electronic structure of the individual molecules in the solid phase is essentially unchanged from that in the vapor phase and metastable atoms deexcite at the surface through Penning ionization process. Figure 11 shows the interaction between a metastable atom A* and molecules BC in the gas and solid phases. The corresponding PIES are shown below in each case. In Figure 11a the gas-phase molecules are randomly oriented with respect to the direction of the metastable atom beam. The relative intensity of the PIES bands, therefore, reflects the overall spread of individual orbitals; an orbital ϕ_2 extending on the average more widely than an orbital ϕ_1 gives a stronger band in PIES. In the case of a solid surface (Figure 11b), on the other hand, a metastable atom interacts with the outermost part (shaded part in the figure) of a regular array of molecules. Hence, if molecules BC are oriented so as to expose the atom C end outside the surface (left

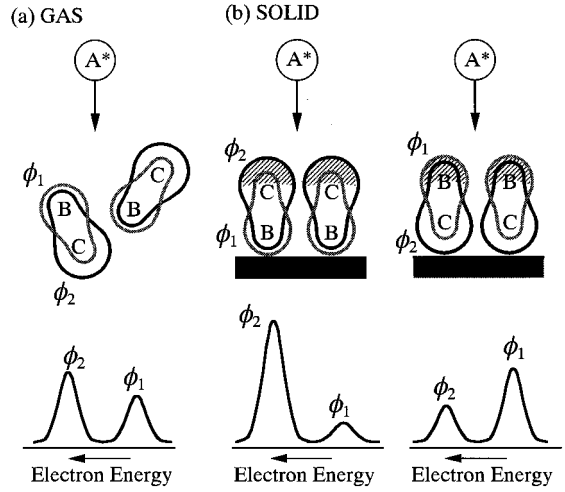

Figure 11. Interaction between a metastable atom A* and molecules BC in the gas (a) and solid phases (b). The corresponding PIES is shown below in each case.

of Figure 11b), the orbital ϕ_2, distributed largely on atom C, gives a stronger band; also, orbital ϕ_1, distributed predominantly on atom B, gives a weaker band compared to the case of the gas-phase spectrum. If the molecular orientation is reversed (right of Figure 11b), the PIES shows a tendency opposite to the above case. Thus, an analysis of the relative intensity of the PIES bands provides information on the geometrical orientation of molecules at the outermost layer. The detail will be discussed in section V.

When the work function of metal is low enough so that the Fermi level is located above the excited level of the metastable atom, the RI process is also suppressed and the direct AD process occurs. This has been observed in alkali metal surfaces, where a complicated process occurs especially in the singlet helium atom (see sections III.B.3 and IV.A.2).

Next we discuss the deexcitation probability of metastable rare gas atoms at the solid surface. The probability of the metastables reflected without deexcitation, the survival probability (SP), was unclear for some time,[69−74] the observed values ranging from 0.5[71] to less than 10^{-4}.[74] In 1982 Conrad et al. obtained reliable SP for clean and adsorbate-covered surfaces applying time-of-flight technique by the use of a detector (channeltron) fully rotatable around the sample within the scattering plane.[75,76] According to their results, SP values are always very small in quite contrast to the case of gas phase scattering;[5] SP for He* and Ar* are 10^{-6} to 10^{-4} in clean surfaces and 10^{-3} in adsorbed and oxidized layers. This was qualitatively explained on the basis of a "dimensionality effect" as follows.[75,77] Owing to the translational invariance parallel to the surface, the elastic movement of a rare gas atom can be described in a one-dimensional subspace of the total Hilbert space, while the inelastic motion is three dimensional. For example, in a perfectly flat surface the only open elastic channel is specular reflection. In this case there is only one possible state for elastic scattering but $(L/a)^2 \approx 10^{14}$ possible states for inelastic scattering using box normalization (L, the size of the box; a, the separation between neighboring atoms).[77] In gas-phase elastic scattering, on the other hand, the

movement of the colliding atom is three dimensional and the density of local states has the same dimensionality, which yields much higher SP compared to the case of the solid surface. The increase of SP for adsorbed and oxidized layers is also explained by the dimensionality effect, because the translational invariance parallel to the surface is expected to break down in these less perfect surfaces. Further, it was observed that the deexcitation process (RI+AN or PI) is not strongly reflected in the SP value.[75,76] Conrad et al. also measured the angular distributions of SP for metastable atoms and found that the values vary considerably from those of the respective ground state atoms showing the marked change of the interaction potentials.[75,76]

Incidentally the electron emission coefficient γ, defined by the number of electrons per incident metastable particle, depends strongly on the excitation energy and the nature of the target surface.[7,78] For example, the γ values for a clean tungsten surface are about 0.3, 0.2, and 0.08 for He*(2^1S,2^3S), Ne*($^3P_{2,0}$), and Ar($^3P_{2,0}$), respectively. That for contaminated stainless steel is 0.5−0.95 for He*(2^1S,2^3S). The measurement of γ and the detection of metastable atoms and molecules are described in ref 78.

When localized spins are present on the surface, the decay of a He*(2^3S) atom with spin orientation parallel to the local electron spins is prevented as a consequence of the Pauli exclusion principle. Therefore, a periodic local spin ordering on the surface leads to a periodic modulation of the beam attenuation, which is reflected in the corresponding diffraction pattern of the elastically scattered He*(2^3S) atoms. Applying this effect, Swan et al. determined the long-range spin ordering on the surface of an antiferromagnetic insulator, NiO(100).[79−81]

Finally we will discuss the interaction between a slow rare gas ion and a solid surface.[36,65,66] As stated above, the ion can be neutralized at the surface through the AN process. However, when the work function of the solid is low enough so that the Fermi level is located above an excited level of the ion (for example, 2s level for He^+), an electron tunnels from a filled level in the solid into the excited level at the same energy. This process is called resonance neutralization (RN). As in eq 21, the rate of the RN process is governed by the square of the overlap integral:

$$I(R)_{RN} = \int \phi_i^*(1)\chi_b(1)\, d\nu_1 \qquad (24)$$

where ϕ_i and χ_b are the wave functions of the filled level of the solid and the excited level of the ion, respectively.

The transition probability of RN becomes appreciable at larger atom−surface distance than that of AN because the wave function of the excited level χ_b is more spatially extended than that of the ground level χ_a (cf., eqs 22 and 24). Therefore, at a surface with low work function an ion converts to a metastable atom through RN before the AN process occurs. The metastable atom thus formed is finally deexcited through AD.

Recently the electron emission due to collisions between solids and slow ionized atoms has aroused much interest.[82] Electron spectra of solid surfaces by impact of multiply charged rare gas ions are analyzed in terms of the following processes:[83]

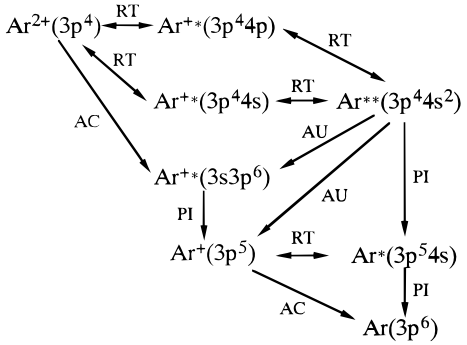

Figure 12. Neutralization scheme for collisions of Ar^{2+} and Pb(111).

(i) Resonant transition (RT) in which either an electron of the target is captured by the projectile (RC) or an electron in an excited level of the projectile is transferred to the target leading to the ionization of the projectile (RI). Thus, RN for a singly charged ion is generalized to RC to include the electron capture processes in multiply charged ions.

(ii) Auger capture (AC) process in which an electron of the target is nonresonantly captured and another target electron is ejected. Here, AN for a singly charged ion is generalized to AC.

(iii) Auger deexcitation process (AD or PI).

(iv) Autoionization of the projectile (AU). This process is possible after the capture of two electrons into excited levels of the projectile.

For example, the effective neutralization scheme proposed for collisions of Ar^{2+} and Pb(111) is shown in Figure 12.[84]

Niehaus et al. developed a model which enables one to simulate electron spectra due to processes i−iv using semiempirical model functions for distance-dependent transition rates and transition energies, and a known surface density of states.[84,85] The transition rate of RT was assumed to be proportional to the square of the overlap of one electron orbitals relevant for the capture process (cf., eqs 21 and 24 for the overlaps in RI and RN). For AC and AD the rate was taken to be proportional to the squared overlap integral between the initial and final one-electron wave functions of only the "down electron" of the corresponding transition (cf., eqs 22 and 23, the initial and final wave functions are ϕ_i and χ_a, respectively, for AN and AD). Further, the rate of AU was assumed to be independent of the distance between the projectile and surface and was determined so as to fit the observed spectrum. To obtain transition energies the one electron energies of the projectile were estimated assuming that the distance-dependent energy shifts are determined mainly by the polarization interaction of a point charge with an ideal conductor, i.e., by the charge−image charge interaction (cf., section III.B.2). Kempter and his collaborators have applied the above model by Niehaus et al. to the simulation of some MAES.[86−88]

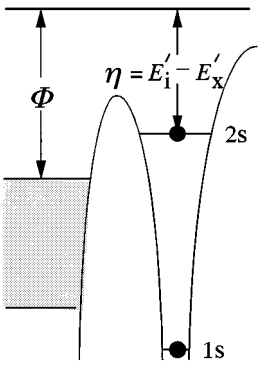

Figure 13. Energy diagram for a metal surface interacting with a helium metastable atom.

2. Energy Levels of the Metastable Atom Near the Solid Surface

As described in the last section, the deexcitation mechanism of the metastable atom is determined by the position of its excited level relative to the Fermi level of the solid. In this section the variation of the energy levels of the metastable atom near the solid surface will be discussed. Figure 13 shows the energy diagram of a metal surface interacting with a He* atom. In a one-electron scheme the position of the 2s level of He* is estimated using the effective ionization energy of the metastable atom near the surface $\eta = E_i' - E_x'$, where E_i' is the effective ionization energy of the ground state He atom and E_x' the effective excitation energy of the He* atom near the surface. The value of E_i' is reduced from its gas-phase value (E_i = 24.6 eV), owing to the interaction between the solid surface and the He^+ ion. This interaction is mainly due to the image force effect,[36,65,66] if the He^+ ion is not very close to the surface (R > 2 Å). For the metal the lowering of E_i caused by the image potential is

$$\Delta E_i = -\frac{e^2}{4(R-d)} = -\frac{3.6}{(R-d)/\text{Å}}\text{eV} \qquad (25)$$

Here R is the distance between the center of the ion and the jellium edge of the metal in which the positive ions of the metal are replaced by a uniform background and d is the distance to correct the classical image force effect. The value of d is estimated to be about 0.6 Å.[89,90] For example, if we take R = 3 Å (the radius of the metastable atom is estimated to be 2.9 Å for He* and 3.2 Å for Ne* [91]) and d = 0.6 Å, ΔE_i = −1.5 eV, which gives 23.1 eV for E_i'. We take the value of E_x' to be equal to its gas phase value E_x (20.6 eV for He*(2^1S) and 19.8 eV for He*(2^3S)), because the difference between E_x' and E_x mainly due to the polarization effect near the metal surface is small. Figure 14 shows the energy curves of the ground and excited levels of He interacting with the metal surface. In the figure the energies $\eta = E_i' - E_x'$ are plotted below the vacuum level.

As stated in the last section, when a metastable atom approaches an ordinary metal or semiconductor surface having a large work function, the RI(+AN) process due to the tunneling of the electron in the outer orbital χ_b takes place before the AD process involving electron transfer to the hole of the inner

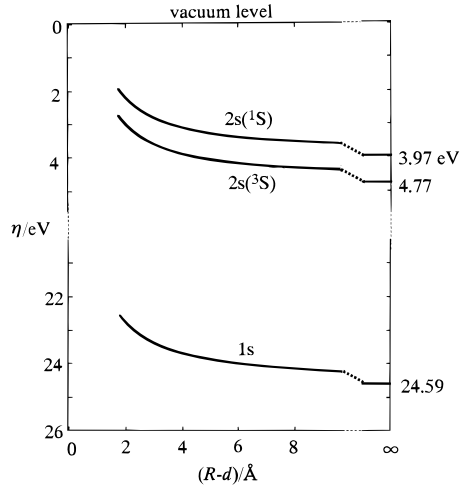

Figure 14. Energy diagram for the ground and two excited levels of helium near a metal surface.

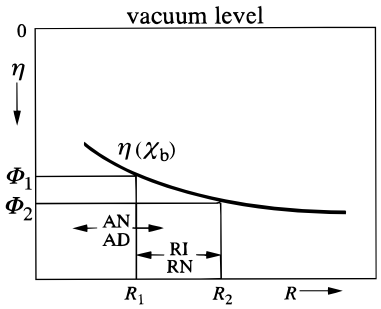

Figure 15. Energy diagram of the excited level of a metastable atom or an ion near a solid surface. The ranges of the atom−surface separations, in which the resonance (RI or RN) and Auger processes(AN or AD) occur, are shown.

orbital χ_a. This is because χ_b is much more spatially expanded and, in general, has much larger overlap with the surface wave function ϕ_p than χ_a (cf., Figure 8 and eqs 21 and 23). However, for some reasons, when the overlap integral between χ_b and ϕ_p is not large enough to induce the RI process, the AD process proceeds. This is observed in the surfaces of graphite[92,93] and $LaCoO_3$,[94,95] as will be discussed in section IV.A.3.

The situation of the predominance of RI over AD (if RI is allowed) is similar to the case of the ion-surface interaction, in which the RN(+AD) process involving χ_b occurs before the AN involving χ_a for low work function surfaces (cf., section III.B.1). Figure 15 shows the effective ionization energy of χ_b, η near the surface. In the figure the interval between R_1 and R_2 corresponds to the atom−surface separations at which the RI or RN process effectively occurs. If the work function of the surface Φ is larger than the critical work function Φ_2 corresponding to R_2, RI is possible but RN is not. In this case, both metastables and ions eject electrons through AN (metastables through RI+AN and ions directly through AN). On the other hand, if Φ is smaller than Φ_1 corresponding to R_1, RN is possible but RI is not. Thus, metastables and ions eject electrons through AD (metastables undergo only AD and ions RN+AD). When Φ is between Φ_1 and Φ_2, RI or AD is possible for metastables and RN or AN is possible for ions. According to Sesselmann et al.,[67] for metastable

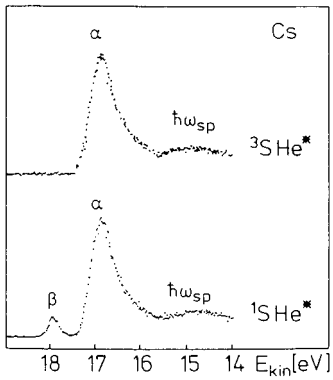

Figure 16. He*(2^1S) and He*(2^3S) MAES of a clean Cs surface. The peaks denoted by $h\omega_{sp}$ are due to surface plasmons. (Reprinted with permission from ref 99. Copyright 1987 Elsevier.)

atoms AD occurs with high probability between 3 and 5 Å (relative to the jellium edge), while RI occurs with appreciable probability already from distances larger than 5 Å if it is energetically allowed.

3. Singlet–Triplet Conversion of Metastable He Atoms

The conversion of He*(2^1S) to He*(2^3S) on alkali metal surfaces has been the subject of intense experimental[29,96−102] and theoretical[103−113] studies in the past years. Roussel found for the first time the experimental evidence for the singlet−triplet conversion.[96] He studied the scattering of He*(2^3S) and He*(2^1S) atoms as He^+ ions from a Ni(111) surface as a function of the work function lowered by K adsorption. On the clean surface ions are not detected because those formed by the resonance ionization of metastable atoms are neutralized by the AN process. As K atoms are adsorbed there appear an increasing number of K^+ sites, which repel ions formed by the RI process before the AN takes place. In this case the ion signal rises from zero for the clean surface and becomes zero again in the region, where the Fermi level is higher than the 2s levels of He* (the surface work function is lower than the ionization energies of metastables) and the RI process is suppressed. The curve for He*(2^3S) shows a monotonous change with one peak, while the curve for He*(2^1S) has two peaks, one of which corresponds to the He*(2^3S) curve. The presence of this peak was regarded as evidence for the conversion of He*(2^1S) to He*(2^3S).[96] Later the two curves for He*(2^1S) and He*(2^3S) were analyzed by a theoretical calculation on the basis of the resonant tunneling process.[103]

Figure 16 shows the He*(2^3S) and He*(2^1S) spectra of Cs (10 or more layers) on a Cu(110) surface.[99] In the figure the He*(2^1S) spectrum displays a very small peak β at higher kinetic energy originating from the interaction between singlet species and the Cs derived states. The much stronger peak α located at lower energy in the He*(2^1S) spectrum is identical to that given in the He*(2^3S), demonstrating that almost all the singlet atoms are converted to the triplet before the AD process occurs.

Several mechanisms have been proposed for the singlet−triplet conversion. Lee et al. proposed a two-step process as shown in Figure 17a.[97] In the first step the 2s electron of a He*(2^1S) atom tunnels into an empty state of the solid to form a He^+ ion, which

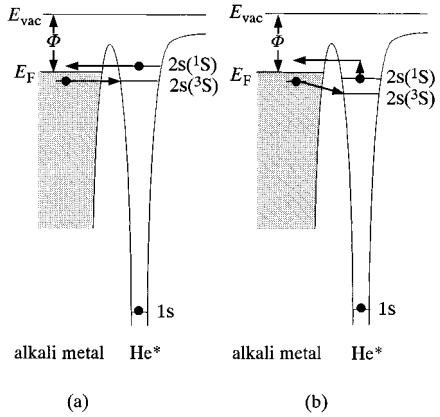

Figure 17. Energy diagrams showing two mechanisms of the singlet−triplet conversion of metastable He atoms (a) two-step resonance process and (b) one-step Auger process.

is then neutralized by the transition of a solid electron into the 2s level with opposite spin in the second step. This process is only possible in the very narrow range of atom−surface distances, where the Fermi level of the surface is lower than the 2s level of He*(2^1S) and higher than that of He*(2^3S). Furthermore, this process is unlikely on a very low work function surface, because it would be necessary that the He*(2^1S) atom approach very near the surface to make the 2s level shift upward in energy. At present the following two conversion mechanisms are generally accepted.

Mechanism I:[98] This is an Auger-type process shown in Figure 17b. A valence electron from the surface fills the hole in the 2s level of He* and the 2s electron with opposite spin is raised to an energy above the Fermi level where it can tunnel into the solid. This spin−flip process competes with the ordinary AD process involving the transfer of a valence electron of the surface to the 1s hole of He*-(2^1S). The former process, however, occurs with much higher probability because the 2s electron is much more diffuse and thus overlaps much effectively with a surface orbital. Mechanism I is supported by various theoretical calculations.[104−109,112]

Mechanism II:[29] The mechanism is illustrated in Figure 18. In the figure the energy positions of the occupied and affinity 2s levels of He*(2^1S) and He*-(2^3S) are shown as a function of atom−surface distance. When the He* atom approaches the surface, the image force field shifts the occupied levels up and the affinity levels down from their asymptotic positions (the electron affinities of the He*(2^1S) and He*(2^3S) atoms are 1.3 and 0.5 eV, respectively[114]). For low work function surfaces the affinity level of He*(2^1S) eventually crosses the Fermi level and can be resonantly ionized by a surface electron to form a negative ion $He^-(1s2s^2,{}^2S)$ (Figure 18a). This core-excited He^- ion undergoes rapid autodetachment to form a He*(2^3S) atom, giving an electron to the solid (Figure 18b) or a ground-state He(1^1S) atom emitting an electron outside. The He*(2^3S) atom thus formed can be resonantly ionized and autodetached again. The formation of $He^-(1s2s^2)$ from He*($2^{1,3}$S) corresponds to the RC process described in relation to the collision between the surface and ion, while the autodetachments of $He^-(1s2s^2)$, giving He*(2^3S) and He(1^1S) are related to the RT and AU processes,

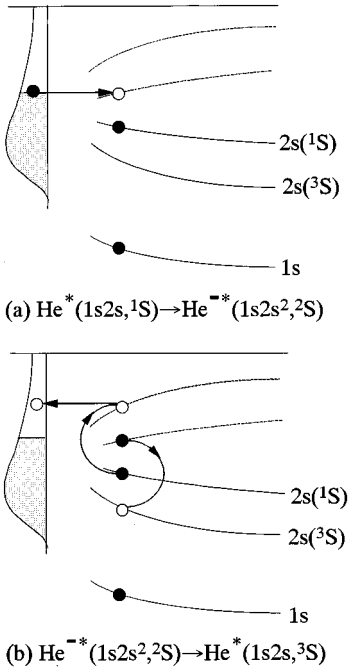

Figure 18. Energy diagram for the singlet−triplet conversion of He* involving He^-: (a) the formation of $He^-(1s2s^2,^2S)$ due to the resonance ionization of He*(2^1S), and (b) the formation of He*(2^3S) by the autodetachment of an electron from $He^-(1s2s^2,^2S)$.

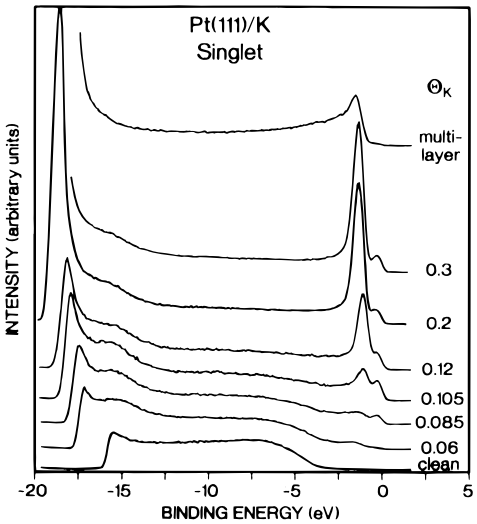

Figure 19. He*(2^1S) MAES of K adsorbed on Pt(111). (Reprinted with permission from ref 29. Copyright 1991 The American Physical Society.)

respectively (cf., section III.B.1). Mechanism II involving the affinity level of He* is applicable when the work function of the surface is small enough (~2 eV[102]) and generally proceeds at a larger distance from the surface than that required for efficient operation of mechanism I. Theoretical treatments for mechanism II involving $He^-(1s2s^2,^2S)$ as a virtual or real intermediate have been reported.[106,110,111,113]

Figure 19 shows the He*(2^1S) spectra of K adsorbed on Pt(111).[29] The spectrum of the clean surface shows the smooth electron distribution, indicating that the RI+AN process occurs because of the high work function of Pt. For potassium coverages up to $\theta = 0.1$ two K 4s bands due to He*(2^1S) and He*-(2^3S) appear and grow at low binding energies. In this region the conversion by mechanism I proceeds.

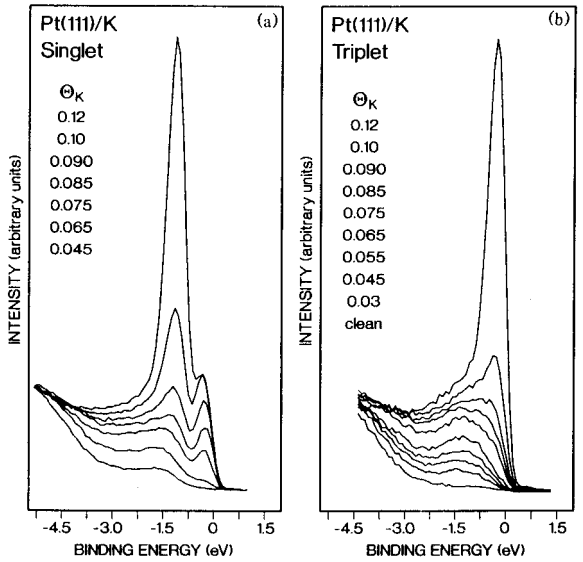

Figure 20. MAES of K adsorbed on Pt(111) by impact of (a) He*(2^1S) and (b) He*(2^3S) atoms. (Reprinted from ref 29. Copyright 1991 The American Physical Society.)

Between $\theta = 0.1$ and 0.2 the triplet peak intensity suddenly increases very strongly and is virtually unchanged on further increase in potassium coverage. After the potassium multilayer formation the peak becomes broad and weak with a tail due to plasmon losses and Auger transitions of solid K. The above abrupt increase in intensity is more evident in the singlet and triplet spectra for the low coverage region (Figure 20).[29] Especially, Figure 20b measured with He*(2^3S) clearly indicates that the sharp increase in the triplet peak intensity is due to an additional very narrow peak at the Fermi level on top of the broad peak at $E_B = 1.4$ eV already present at lower coverages. The above spectral changes shown in Figures 19 and 20 suggest that the autodetachment decay of $He^-(1s2s^2,^2S)$ by mechanism II takes place in intermediate coverages with low work functions. The formation of $He^-(1s2s^2,^2S)$ has also been shown in the electron spectra from He^+ and He^{2+} colliding with alkali metal covered W(110)[101,115] and Cu(111)[116] surfaces.

The singlet−triplet conversion efficiently occurs when occupied and unoccupied states of the surface located near the Fermi level have high densities because these states are directly involved in both mechanisms I and II. This is indicated in Figure 21.[102] In the figure the upper panel shows the intensities of the singlet and triplet valence peaks in the He*(2^1S) spectrum of a Ru(0001) surface covered with different concentrations of Na. The lower panel shows the ratio of the triplet to singlet intensities R, a measure for the singlet−triplet conversion efficiency together with work function Φ as a function of Na coverage. The variation of Φ showing a minimum is typical of alkali metal overlayers and is related to the continuous phase transition of the adsorbate from the isolated ("ionic") to the condensed ("metallic") state. As is seen in Figure 21, the conversion efficiency R starts to increase around Φ = min. where the "metalization" begins[117] and reaches a saturation value of 30 around 0.8 ML (monolayer) where the overlayer is essentially metal-

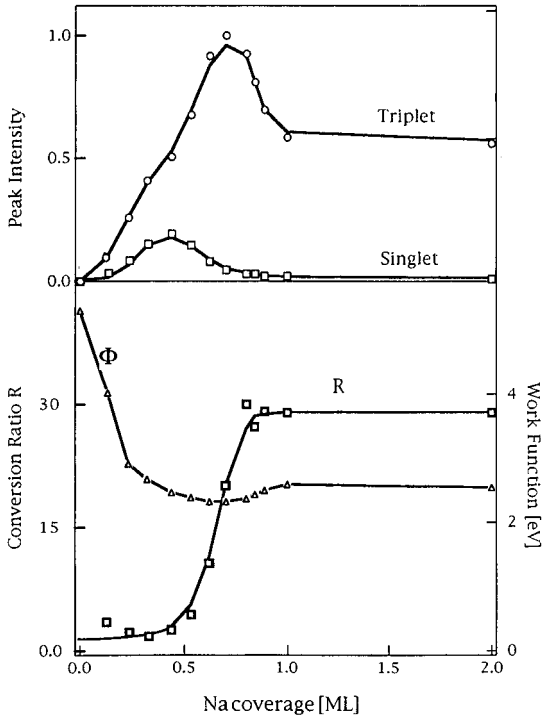

Figure 21. Intensities of the singlet and triplet peaks in the He*(2^1S) spectrum of Na/Ru(0001) (top panel) compared with the singlet−triplet conversion ratio *R* and the work function Φ (bottom panel) as a function of Na coverage. (Reprinted with permission from ref 102. Copyright 1994 The American Physical Society.)

lic. Thus, the value of *R* is closely related to the density of states near the Fermi level which increases in the process of the metallization. In fact, a Si(100) surface covered with Cs that is metallic in character causes the singlet−triplet conversion,[118] while the surface covered with K displaying semiconductive behavior scarcely does.[119]

The singlet−triplet conversion in Na overlayers on Ru mentioned above proceeds by mechanism I because the work function of the surface is higher than 2.5 eV (cf., Figure 21). For the Cs/Ru(0001) system with a lower work function the conversion by mechanism II takes place.[102] Figure 22a shows the changes of singlet and triplet intensities, as well as of *R* and Φ with Cs coverage.[102] In contrast to the case of Na/Ru the conversion ratio *R* exhibits a sharp maximum around Φ = min., which is less than 2 eV. The upper panel of Figure 22a shows that this maximum is essentially due to a lowering of the singlet intensity, which suggests that mechanism II is dominant in this region, because the singlet−triplet conversion by mechanism II involving the affinity level occurs at larger distance from the surface than that by mechanism I and thus Auger deexcitation into the ground state is less efficient. Figure 22b shows the MAES corresponding to points A and B in the *R* curves. The FWHM (full width at half maximum) of the triplet peak for A (FWHM of 0.4 eV is considered to be due to the instrumental resolution) is much narrower than that for B, which indicates that mechanism II is operating in the high *R* region (A), while both mechanisms I and II proceed in the region near B.

IV. Inorganic Surfaces

A. Clean Surfaces

1. Transition and Noble Metals

In 1954, Hagstrum postulated that a rare-gas metastable atom incident on a metal surface would be deexcited to the ground state via resonance ionization (RI) followed by Auger neutralization (AN)[91] (see section III.B.1). After some controversy on the possibility of direct Auger deexcitation (AD) or Penning ionization (PI),[25,71−73,120−122] it is now well-established that Hagstrum's prediction is correct, namely, the RI+AN process operates predominantly on clean Fe(110),[123] Ni(100),[124] Ni(110),[125,126]

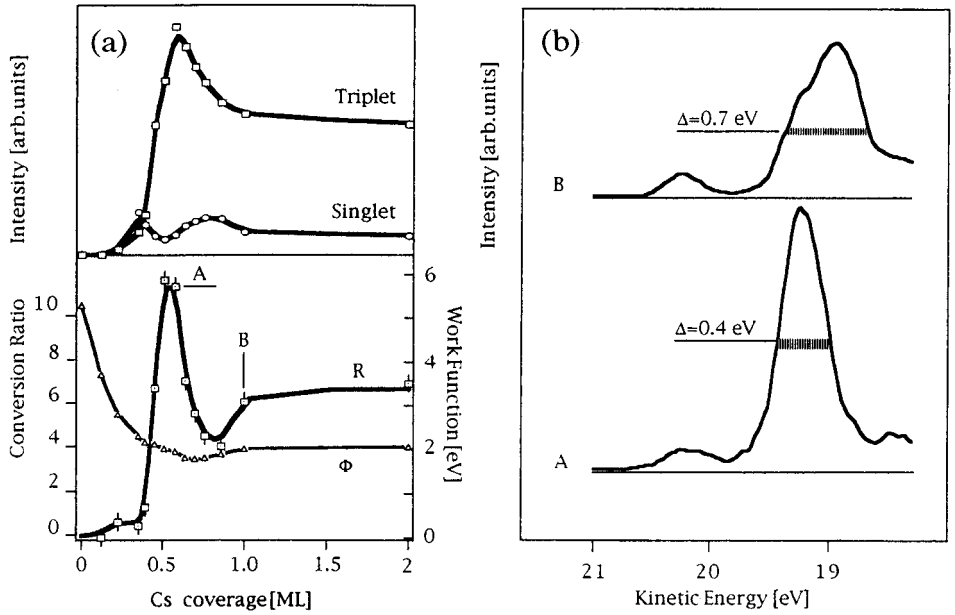

Figure 22. (a) Intensities of the singlet and triplet peaks in the He*(2^1S) spectrum of Cs/Ru(0001) compared with the singlet−triplet conversion ratio *R* and the work function Φ as a function of Cs coverage, and (b) the MAES corresponding to points A and B in the *R* curve in a. (Reprinted with permission from ref 102. Copyright 1994 The American Physical Society.)

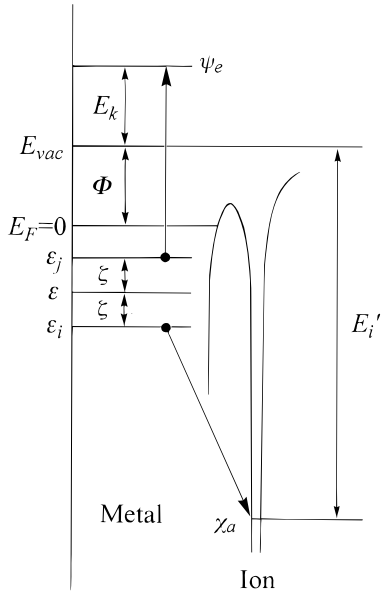

Figure 23. Energy diagram of Auger neutralization process.

Ni(111),[27,74] Cu(100),[127,128] Cu(110),[67,129,130] Mo(110),[25,37] Pd(100),[131] Pd(110),[38,67,127] Pd(111),[24,67,129,130] Ru(0001),[132] Ag(100),[133] Ag(110),[134] Pt(111),[29] W(110),[42] and Au(100)[135] surfaces. As described in section III, the AN process produces two holes in the valence bands and therefore the analysis of data is not so direct as in the case of the PI process.

In this section, we will describe first what information can be derived from the AN spectrum following to the simple theory developed by Hagstrum,[65] although several theories have been reported.[136−140] Second, we take up a clean Pd(111) surface as a typical analysis of the surface electronic states[129,130] and a ferromagnetic Ni(110) surface as an example probing the surface magnetism.[125]

The energy-level diagram of the AN process at a metal surface is shown in Figure 23. The AN process is regarded as two-electron transfer, where a metal electron at binding energy ϵ_i (referred to the Fermi energy, E_F) transfers to the lowest unoccupied orbital (χ_a) of the rare-gas ion and an another metal electron at ϵ_j is emitted to an empty state (ψ_e), simultaneously. If the energy transfer is sufficiently large, the second electron may escape from the metal. The kinetic energy of the emitted electron, E_k, is then given by the energy balance

$$E_i' - \epsilon_i - \Phi = E_k + \Phi + \epsilon_j \qquad (26)$$

or

$$E_k = E_i' - \epsilon_i - \epsilon_j - 2\Phi \qquad (26')$$

where E_i' is the effective ionization potential of the (ground-state) rare-gas atom in front of the surface and Φ is the work function of the metal. For convenience, eq 26 is also written by the following form:

$$E_k = E_i' - (\epsilon - \zeta) - (\epsilon + \zeta) - 2\Phi = E_i' - 2(\epsilon + \Phi) \qquad (27)$$

Here, ϵ is the mean binding energy of the two valence electrons and 2ζ is the respective difference in binding energy, i.e., $\epsilon = (\epsilon_i + \epsilon_j)/2$ and $\zeta = (\epsilon_i - \epsilon_j)/2$. Equation 27 indicates that (i) E_k is independent of ζ, namely, pairs of transitions with different ζ give an identical E_k, and (ii) if the AN process involves two electrons at E_F ($\epsilon = \zeta = 0$), the emitted electron has the maximum kinetic energy, E_k (max) $= E_i' - 2\Phi$, yielding the high energy cutoff of the spectrum.

The transition rate $P(\epsilon)$ of the AN process is given by integrating over all combinations of transitions

$$P(\epsilon) \approx \int |H_{fi}|^2 N(\epsilon - \zeta) N(\epsilon + \zeta)\, d\zeta \qquad (28)$$

Here, $N(\epsilon)$ is the local density of states (DOS) at which the AN process occurs. H_{fi} is the matrix element of the form

$$H_{fi} = \int\int \chi_a^*(\boldsymbol{r}_2)\psi_e^*(\boldsymbol{r}_1)F(|\boldsymbol{r}_1 - \boldsymbol{r}_2|)\phi_j(\boldsymbol{r}_1)\phi_i(\boldsymbol{r}_2)\, d\boldsymbol{r}_1\, d\boldsymbol{r}_2 \qquad (29)$$

where ϕ_i and ϕ_j are the orbitals of the surface electrons involved and $F(|\boldsymbol{r}_1 - \boldsymbol{r}_2|)$ is a screened Coulomb potential between the two surface electrons. If the electronic structure of the surface is known, one may calculate in principle the matrix element and also the transition probability. In general, however, it is just opposite, since we wish to know information on the surface electronic states from the measured AN spectrum. As a first approximation, it is assumed that the matrix element depends only on the initial energies of the two surface electrons, i.e.,

$$|H_{fi}|^2 = |H(\epsilon - \zeta)H(\epsilon + \zeta)| \qquad (30)$$

Then $P(\epsilon)$ is transformed into a self-convolution integral

$$P(\epsilon) \approx \int U(\epsilon - \zeta)U(\epsilon + \zeta)\, d\zeta \qquad (31)$$

Equation 31 gives the mathematically unique solution, $U(\epsilon)$ ($= H(\epsilon)N(\epsilon)$), which is referred to the transition density. To obtain $U(\epsilon)$ from $P(\epsilon)$ several methods have been developed on the basis of a step-by-step deconvolution technique,[141] discrete Fourier transformation,[142] interpolating spline functions,[25,143] etc. The formalisms and limitations of the deconvolution procedure were discussed in detail by Hagstrum and Becker,[141] Boiziau et al.,[25] and Sesselmann et al.[67] As was emphasized by these authors, the physical meaning of $U(\epsilon)$ should be discussed carefully, since it reflects not the surface DOS itself but that modified by transition matrix elements. The electron transfer to the ion approaching the surface depends essentially on the differential overlap between the wave functions of the ion and surface, $\langle\chi_a(r)|\phi_i(r)\rangle$, at which the AN process takes place (typically at the distance of ~3 Å in front of the first atomic layer).[67] Therefore, an electronic wave function exposed further outside the surface gives more effective overlap compared with that distributed inside the surface. If we take a short-range nature of the screened Coulomb potential in eq 29 into account, the second electron is considered to be

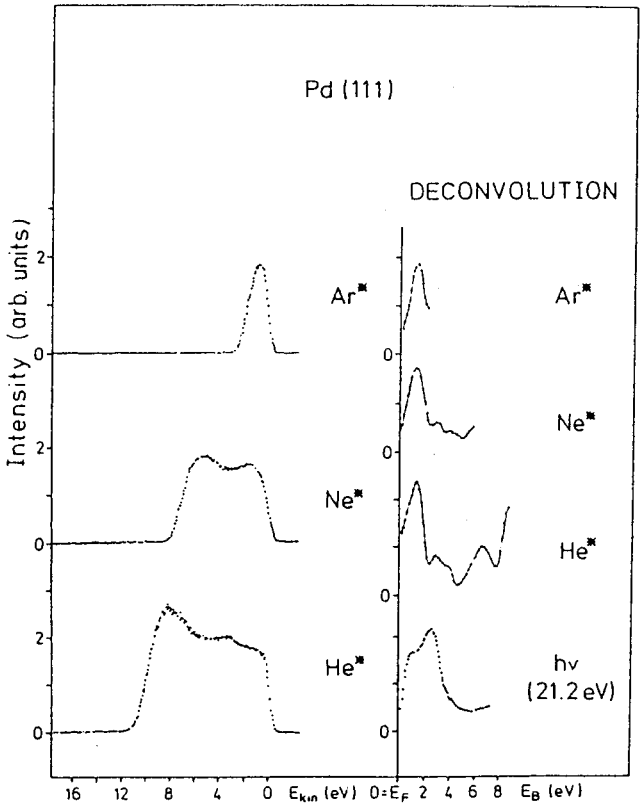

Figure 24. Auger neutralization spectra of a clean Pd(111) surface using He*, Ne*, and Ar* metastable atoms, the deconvolution of these spectra, and a photoemission spectrum using the He I resonance line (21.2 eV). (Reprinted with permission from ref 130. Copyright 1987 The American Physical Society.)

emitted also from the local area at the outermost layer. Consequently, the transition rate is determined largely by the spatial electron distribution exposed outside the surface.

As described in section III.B.1, the AN process also proceeds when a rare-gas ion beam is incident on a metal surface in ion neutralization spectroscopy (INS). The AN process produces two holes in the valence band as in the usual core−valence−valence Auger transition. The intrinsic and technical advantages of MAES are summarized as follows:

(i) The AN spectrum is extremely surface sensitive, because the AN process takes place just outside the surface.

(ii) In INS rare-gas ions with appreciable kinetic energy cause some complications such as broadening effect.[65] MAES is free from these complications, because it uses metastable atoms with thermal kinetic energy (<0.1 eV).

(iii) The band shape near the threshold in the AN spectrum is not affected by the background due to secondary electrons encountered in the usual core−valence−valence Auger spectrum.[144]

(iv) If spin-polarized metastable atoms are used as the excitation source, the AN spectrum reflects the magnetic properties of the surface.[123,125]

a. Pd(111). Figure 24 shows the electron emission spectra of a clean Pd(111) surface using the He*, Ne*, and Ar* metastable atoms measured by Sesselmann et al.[130] The photoemission spectrum using the He I resonance line is also shown in the figure, where two

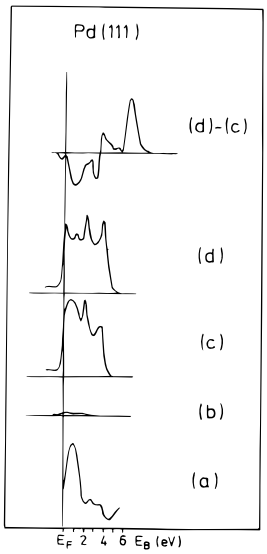

Figure 25. Deconvolution of the He* spectrum from a clean Pd(111) surface and the calculated local density of states of the clean Pd(111) surfaces (a) deconvoluted spectrum, (b) calculated local density of states at a distance of 2.74 Å in front of the first metal layer, (c) at the first layer (surface density of states, SDOS), and (d) at the fourth layer (bulk density of states, BDOS). The difference d−c of the calculated BDOS and SDOS is also shown. (Reprinted with permission from ref 130. Copyright 1987 The American Physical Society.)

peaks just below E_F are due to direct emissions from the Pd 4d valence bands. The maximum kinetic energy of emitted electrons E_k(max) in the He*, Ne*, and Ar* spectra is 11.1, 8.1, and 2.6 eV, respectively. Since the work function Φ of the Pd(111) surface is 5.6 eV, these values are too low to be regarded as the PI process. In the case of the RI+AN mechanism, E_k(max) is given by $E_i' - 2\Phi$, where E_i' is the effective ionization potential of the rare-gas atom in the ground state (cf., eq 27). E_i' is reduced by about 2 eV from its gas-phase value mainly owing to image force effect, i.e., 24.6 − 2 = 22.6 (eV) for He, 21.6 − 2 = 19.6 (eV) for Ne, and 15.8 − 2 = 13.8 (eV) for Ar. These values yield E_k(max) = 11.4, 8.4, and 2.6 eV for He, Ne, and Ar, which agree fairly well with the experimentally observed values and indicate the operation of the RI+AN mechanism.

As mentioned above, the AN spectrum reflects essentially the self-convolution of the local DOS at the surface layer. The deconvolution of the data is shown in Figure 24. All the deconvoluted spectra are in agreement with each other and indicate the reliability of the deconvolution procedure. Sesselmann et al. compared the deconvoluted spectrum of He* with the local DOS calculated by a self-consistent pseudo-potential method.[145] The results are shown in Figure 25. The peak positions in the spectrum (a) correspond well to the calculated surface DOS (c) rather than the bulk DOS (d). It is seen in the figure, however, that the first peak just below E_F is much enhanced in the experimental spectrum. This is due to the matrix element effects:

(i) Within the free electron model, the wave function tail extending outside the surface is proportional to $\exp(-E_B^{1/2}R)$ where E_B is the binding energy of the valence electron with respect to E_F.[99] Therefore, the overlap of the Pd sp wave functions with the He^+ 1s

hole will be more effective and Auger transition rate will be much higher for the valence states near E_F.

(ii) For Pd(111) the occupied surface states and surface resonances are located mainly in the energy region from E_F to about 2 eV binding energy. These states exhibit a high local density in the outermost surface layer. This is clearly seen in Figure 25 where the surface DOS (c) is much higher near E_F than the bulk DOS (d). Further, the surface states and resonances contribute to the local density (b) at about 3 Å region in front of the surface where the AN process takes place most probably. Owing to these features, the surface states and resonances interact with the incoming He^+ ions preferentially and yield a strong feature in the spectrum.

A similar deconvolution technique has been applied to the analysis of AN spectra. Boiziau et al. measured the He* spectrum of a clean Mo(110) and showed that the peak positions in the deconvoluted spectrum are in good agreement with those in the calculated and photoemission DOS.[25] Sesselmann et al. showed that the structures in the deconvoluted spectrum of a clean Cu(110) surface correspond well to those in the photoemission spectrum except for the peak intensities: In the deconvoluted spectrum the peak due to the spatially expanded free-electron-like Cu 4s bands is much enhanced relative to that due to the spatially localized Cu 3d bands.[130]

Sesselmann et al. also measured the angle dependence of emitted electrons when rare-gas metastable atoms collide with a clean Pd(111) and Cu(110) surfaces.[67] These data exhibit that the angular distributions of emitted electrons are highly anisotropic in intensity, being similar to those in the core−valence−valence Auger transitions. The anisotropic feature could be related partly to the spatial distribution of valence electrons, but is not well interpreted at present.

b. Ferromagnetic Ni(110). Onellion et al. examined the interaction of spin-polarized He*(2^3S) atoms with a ferromagnetic Ni(110) surface in order to probe the surface magnetism.[125] The experimental alignment is similar to that shown in Figure 3. Figure 26 shows the He*(2^3S) MAES of the sample at ~130 °C together with the polarization asymmetry A as a function of the retarding bias applied to the electron analyzer. The parameter A is defined by $A = (1/|P_z|)\{(R_+ - R_-)/(R_+ + R_-)\}$, where R_+ and R_- are count rates of detected electrons of the beam polarizations $P_z > 0$ and $P_z < 0$, respectively (see eq 4).

It turns out from Figure 26 that the sign of the asymmetry parameter is positive. This means that the He*(2^3S) atoms with spin parallel to the majority spin of the sample yield stronger electron emission than the opposite spin polarization. Further the asymmetry parameter increases drastically with increasing the retarding bias, namely for electrons emitted near E_F. Onellion et al. interpreted these features on the basis of the energy diagram schematically shown in Figure 27. For the magnetized Ni surface, the valence bands split in energy owing to the exchange interaction (mainly between Ni 3d electrons) as in the case of the bulk: the majority (up-spin) bands shift downward in energy, while the

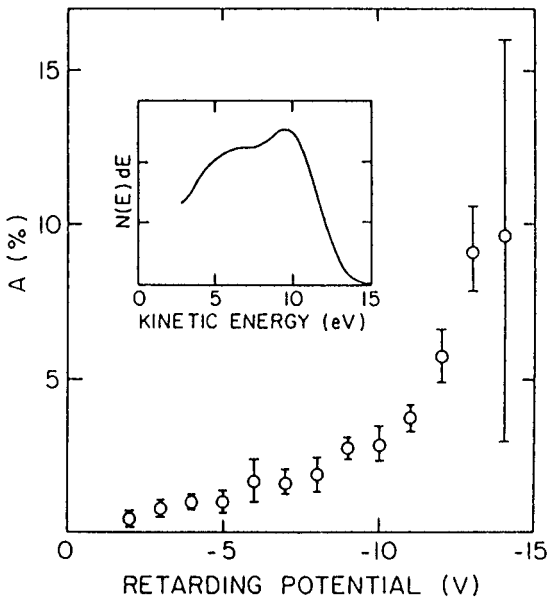

Figure 26. Polarization asymmetry A as a function of retarding potential for a clean, magnetized Ni(110) surface at ~130 °C. The inset shows the electron emission spectrum excited by the He*(2^3S) atoms. (Reprinted with permission from ref 125. Copyright 1984 The American Physical Society.)

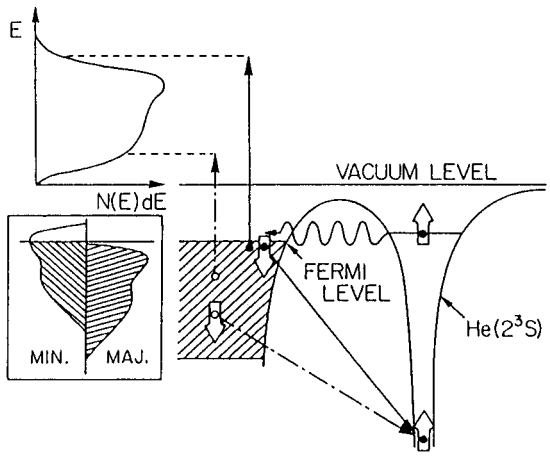

Figure 27. Energy diagram illustrating the He*(2^3S)−Ni(110) surface interaction. Resonance ionization is indicated by the wavy arrows, Auger neutralization by corresponding pairs of straight arrows, and open arrows denote electron spins. (Reprinted with permission from ref 125. Copyright 1984 The American Physical Society.)

minority (down-spin) bands move upward. Consequently, the electronic states located near E_F will be occupied mainly by down-spin electrons. When a spin-polarized He*($1s^{\uparrow}2s^{\uparrow}$) atom approaches to such a magnetized surface, it is firstly ionized by resonance tunneling of the $2s^{\uparrow}$ electron into a conduction band, as shown by a wavy line in Figure 27. Then, the spin-polarized $He^+(1s^{\uparrow})$ ion formed is neutralized to the singlet ground state $He(1s^{2\uparrow\downarrow})$ only by electron transfer from the minority (down-spin) band. Since the emitted electrons with the highest kinetic energy result from the AN process in which the two electrons both originate near E_F, where there are few up-spin electrons, the asymmetry parameter A is largest at high energies, in agreement with the observed dada. Onellion et al. also measured the parameter A as a function of the sample temperature and found that

it decreases linearly with the temperature, in marked contrast to the bulk magnetization behavior, although the surface Curie temperature is the same as the bulk value.

The theoretical analysis of the asymmetry parameter was made by Penn and Apell.[139] They indicated that the observed asymmetry in Figure 26 can be reproduced only by the use of a realistic potential for the Ni electrons in the vacuum region and that the magnetization of Ni(110) is −20% at E_F and at about 4.5 Å from the surface. The negative magnetization in the vacuum above Ni(110) is consistent with band calculations,[146] in which the Ni sp electrons spill out into the vacuum region and are polarized oppositely from the Ni 3d electrons through the s−d hybridization.

The spin-polarized MAES has been applied to the clean metal surfaces such as ferromagnetic Fe(110) on GaAs,[123] Fe(110) on W(110),[147a,b] Fe layer on Ag(100),[147c] and CO(0001) on W(110)[147b,d] to obtain the asymmetric parameter. Further, Hart et al. measured the spin polarization of emitted electrons P (which is defined by eq 5) from a clean Cu(100).[127] Although the copper is nonmagnetic, the polarization P was found to be nonzero, i.e., it is about 20% at the lower kinetic energy region and rises up to about 75% at the highest energy region (corresponding to emission from E_F). Some interpretations of this spin correlation involving the surface electronic properties were given by Dunning et al.[51,128,148,149] and Salmi et al.[140]

2. Alkali Metals

In a low work function metal, the resonance ionization (RI) is suppressed because a valence band lies opposite the highest occupied level of a rare-gas metastable atom, and hence the direct Penning ionization (PI) takes place. Alkali metals, alkaline-earth metals, and rare-earth metals belong to this category. Further, it is known that the singlet−triplet conversion of a He* metastable atom proceeds efficiently on these surfaces, as described in section III.B.3.

The He*(2^3S) spectra of clean surfaces of polycrystalline alkali-metals (Li, Na, K, Rb, and Cs) were measured by Woratschek et al.[99] The data of a clean Cs multilayer are shown in Figure 28. From the comparison with the He I photoemission spectrum, the observed bands were related to direct emissions from the Cs 6s and 5p-derived states via the PI process, surface plasmon loss, and O_3VV-Auger transition (which is denoted by A in the figure). As is seen in the figure, the Cs 6s-derived band is extremely weak in the He I spectrum owing to the low photoionization cross section, while the corresponding band is much more intense in the He*(2^3S) spectrum. A similar enhancement of the s-derived band was also observed for the other alkali metals. Using such a high sensitivity for the s-derived band, Woratschek et al. compared the observed band shape with the free-electron density of states and indicated that the band shape is strongly modified by the transition matrix effect.

A few years later, however, Hemmen and Conrad[29] pointed out that the analysis of the strong emission near E_F is not so straightforward by considering the

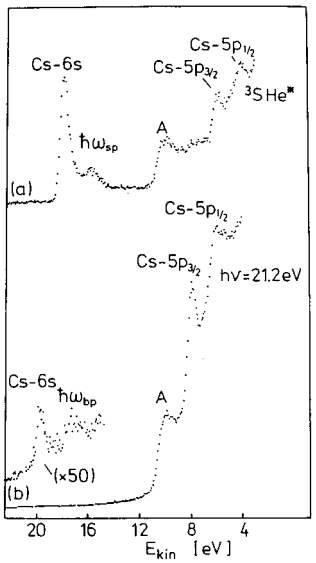

Figure 28. Electron emission spectra of a clean Cs surface using the He I resonance line (21.2 eV) and He*(2^3S, 19.8 eV) atoms. (Reprinted with permission from ref 99. Copyright 1987 Elsevier.)

operation of an additional decay channel, i.e., the formation of a core-excited negative He^- ion with the $(1s^12s^2)^2$S configuration and subsequent intraatomic Auger decay into the ground state by an autodetachment process (see Figure 18). When these processes take place on the surface, it is expected that (i) the band due to autodetached electrons appear at E_F in the spectrum and (ii) its intensity grows up with decreasing the work function of the surface. This prediction has been verified by the coverage-dependent spectra of the potassium-adsorbed Pt(111) surface shown in section III.B.3 and also Ar* spectra of Na, K, and Rb multilayers.[100] It should be noted that the enhancement of the s-derived band in MAES is commonly observed, which involves not only other low work function metals such as Ba[100] and Yb[150] but also a gas-phase Hg atom[4] and several organic molecules.[151−153]

3. Semiconductors and Semimetals

As mentioned in section III.B.1, when a rare-gas metastable atom collides with a clean semiconductor or semimetal surface, the deexcitation channel (RI+AN or PI) depends on the surface electronic structure: it deexcites to the ground state on clean Si(100)-2×1,[149,154−156] Si(111)-7×7,[39,41,144,157] GaAs-(100),[158] GaAs(110),[159] TaS_2(001),[160] and MoS_2(001)[94] surfaces predominantly via the RI+AN process, while on graphite[92,93] and $LaCoO_3$[94,95] surfaces mainly via the PI process. In this section, we take up four examples measured in our laboratory; a typical semiconductor (Si), two-dimensional layer compounds (graphite and MoS_2), and a transition-metal compound ($LaCoO_3$).

a. Si(111)-7×7. In tetragonal semiconductors such as Si, the cleavage of the crystals breaks the covalent bonds and gives rise to the dangling bonds. To minimize the total energy of the system, such dangling bonds recombine with each other and the strong modifications in surface atom positions (i.e., relaxation and reconstruction) generally occur. The

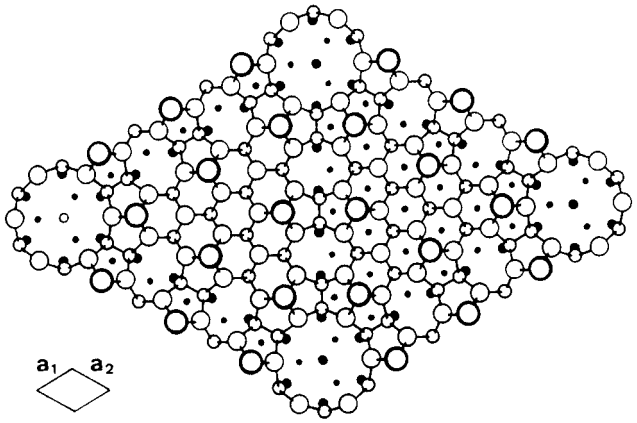

Figure 29. Structure of the Si(111)-7×7 surface based on the dimer−adatom−stacking fault (DAS) model. Large circles denote adatoms in the first layer, smaller circles and dots denote atoms below the second layer. (Reprinted with permission from ref 161. Copyright 1985 Elsevier.)

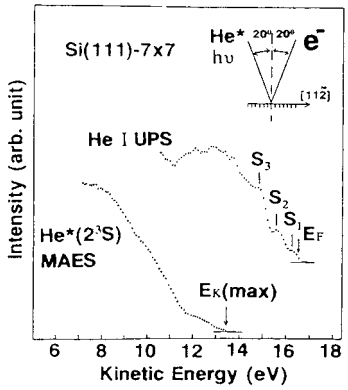

Figure 30. Electron emission spectra of a Si(111)-7×7 surface using the He I resonance line and He*(2^3S) atoms. (Reprinted with permission from ref 41. Copyright 1990 Elsevier.)

Si(111)-7×7 superstructure[161] schematically shown in Figure 29 is a typical example. If an electronic state derived from dangling bonds and/or back bonds is formed in the band gap, the amplitude of the wave function decreases rapidly with penetrating into the bulk. This state is well localized at the surface and referred to the surface state. So far a large number of theoretical and experimental studies have been performed to identify surface states. Owing to the extreme surface sensitivity, MAES is expected to be particularly useful to detect transitions involving surface states.

Figure 30 shows the He I and He*(2^3S) spectra of a Si(111)-7×7 surface.[41] The threshold of photoemission corresponds to the Fermi level E_F. In the He I spectrum, three sharp peaks at 0.3, 0.8, and 1.8 eV below E_F (labeled S_1, S_2, and S_3, respectively) were attributed to emissions from the surface states.[162] Their local origins were clarified by scanning tunneling spectroscopy;[163] the S_1 and S_2 peaks are due to the dangling-bond states localized on the 12 adatoms and those localized on the six free atoms beneath the adatom layer and on a corner hole, respectively, and the S_3 peak is due to the back-bond state on the adatoms (see Figure 29). The He*(2^3S) spectrum does not exhibit such sharp peaks as observed in the photoemission spectrum and is rather similar with the ion neutralization spectrum[164] and

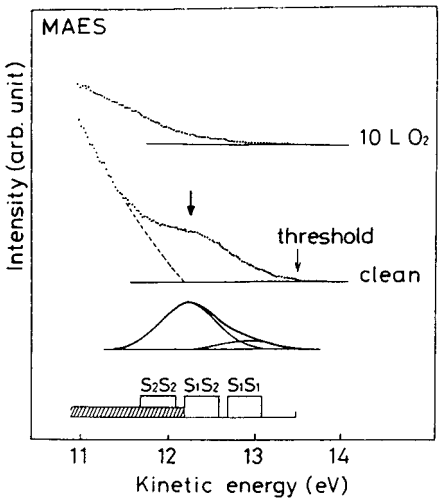

Figure 31. Metastable atom electron spectra of a clean and oxygen-covered Si(111)-7×7 surfaces using the He*-(2^3S) atoms. The tail structure obtained by subtracting the bulk band contribution is also shown. The expected band positions due to Auger neutralization across the surface states S_1 and S_2 are indicated together with those involving the bulk states (hatched region). (Reprinted with permission from ref 144. Copyright 1992 Elsevier.)

the core−valence−valence Auger spectrum[165] except for a weak tail at high E_k region, which indicates that He*(2^3S) atoms deexcite predominantly via the RI+AN process. In fact He*(2^1S) atoms give rise to almost the same spectrum (which is not shown in Figure 30) as the He*(2^3S), reflecting the formation of He^+ ions. It was once suggested that the PI process takes place on the 7×7 surface,[166] but this is not the case.

Figure 31 shows the expanded He*(2^3S) spectra near the threshold for a 7×7 surface and for the oxygen adsorbed surface prepared by 10 L O_2 exposure at 300 K.[144] Since the tail structure disappears almost completely after such exposure, it can be identified with emissions from the surface states, by analogy with the analysis of photoemission. The Auger transition energies across the surface states S_1 and S_2 expected from eq 26 are shown in Figure 31, where the one-electron binding energies obtained by the He I spectrum are used. The notation S_iS_j in the figure denotes the final hole state. The observed peak coincides well to the expected S_1S_2 level within ∼0.2 eV and is attributed to the cross transition involving two dangling-bond surface states S_1 and S_2. The S_1S_1 state is not observed as a prominent peak, but a lower-lying part of the asymmetric tail probably relates to this hole state. In fact the above assignment is confirmed by the deconvolution of the spectrum.[157] The good agreement between the two-hole binding energies obtained by the spectrum and those expected from one-electron energies indicates that the hole−hole interaction across the surface states is very small. It is well-known that the hole−hole interaction is not negligible for narrow band (transition metal) compounds.[167] Here, it is not the case, because the dangling-bond states of S_1 and S_2 are localized spatially and separated with each other, leading to small electron correlation.

As is seen in Figure 30, the intensity of the S_1S_1 and S_1S_2 states are very weak compared with the higher-lying bands, although MAES is surface sensi-

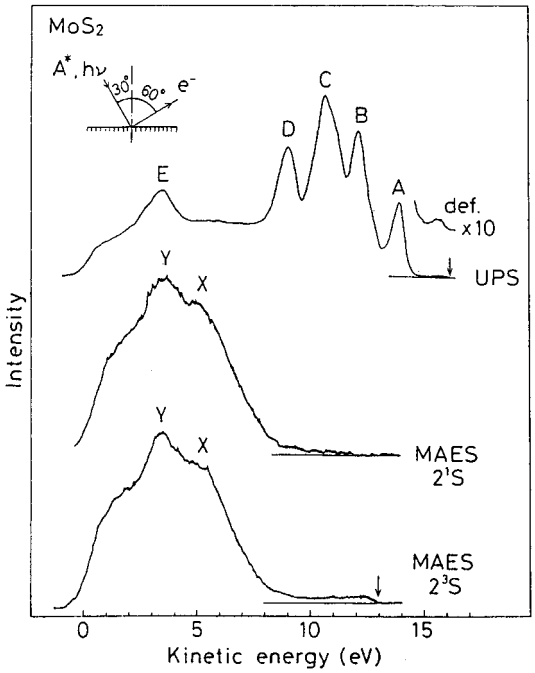

Figure 32. Electron emission spectra of a MoS_2 surface using the He I resonance line and He*(2^1S and 2^3S) atoms. (Reprinted with permission from ref 94. Copyright 1993 Elsevier.)

tive. This is also in striking contrast to the case of the free-electron like surface state of Cu.[130] Two reasons for this finding are considered. One is due to the low density of the dandling-bond surface states. The other is due to the matrix element effect. The dangling-bond S_1 state is highly localized on an adatom and is half filled. Therefore, if the electron of the S_1 state transfers to the He^+ 1s hole, the Auger electron giving the S_1S_1 or S_1S_2 band should be emitted from one of the neighboring adatoms or free atoms. According to the DAS model, the nearest-neighbor distance between adatoms is 6.7 Å and that between an adatom and an free atom is 5.0 Å. Owing to the short-range nature of the screened Coulomb potential, the transition rates giving rise to two holes separated by such large distances are strongly suppressed.

b. MoS_2. Molybdenum disulfide, MoS_2, is a typical layer compound and its structure consists of "sandwiches", each having three sublayers of atoms in the sequence of S−Mo−S. The interlayer interactions are of van der Waals type and are rather weak compared to the intralayer bonding. This reflects in the highly anisotropic properties, e.g., the crystal is easily cleaved. Within the simple picture of the electronic structure of MoS_2, the electrons are considered to be confined well in the individual sandwiches and hence the valence bands are essentially two-dimensional in nature. In fact, the previous photoemission studies indicate that the energy band dispersion is rather flat in the k_z direction (where z axis is perpendicular to the surface) compared to the direction parallel to the surface.[168] Further, it was found that the uppermost valence band is composed of the atomic-like Mo $4d_{z^2}$ orbitals,[169] while the lower-lying bands are dispersive and derived mainly from the S 3p and 3s orbitals.[168]

Figure 32 shows the He I and He*(2^1S, 2^3S) spectra

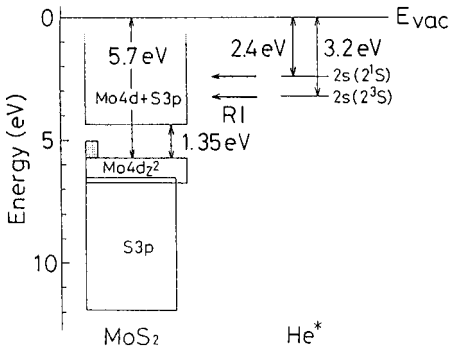

Figure 33. Energy diagram of MoS_2 and He*(2^1S and 2^3S) atoms interacting near the surface. (Reprinted with permission from ref 94. Copyright 1993 Elsevier.)

of a MoS_2(001) surface.[94] Five sharp peaks A−E are observed in the UPS and can be assigned as follows: peak A is due to the atomic-like Mo $4d_{z^2}$ state, peaks B−D are due to the dispersive S 3p-derived bands, peak E is due to the S 3s-derived bands. A very weak peak at higher E_k region (band gap region) is probably due to defect levels. The He*(2^1S) and He*(2^3S) spectra are almost identical and do not correspond to the UPS, being characterized by a weak tail in the higher E_k side and two broad intense bands X and Y. These features indicate that He* metastable atoms deexcite on the MoS_2 surface predominantly via the RI+AN process.

Now we discuss the occurrence of the RI process on the MoS_2 surface. As mentioned in section III.B.1, the RI process corresponds to the electron transfer from the He* 2s state to an empty state of the surface. The ionization energy of the He* 2s electron near the surface is approximated by the difference between the effective ionization potential (E_i') of the ground-state He and the effective excitation energy (E_x') of He*. The AN process involving two electrons with the lowest binding energy (which corresponds to the defect level in the present case) gives the maximum kinetic energy of the emitted electron; $E_k(\max) = E_i' - 2\Phi$ (eq 27). Using the observed values ($\Phi = 5.0$ eV and $E_k(\max) = 13.0$ eV), E_i' is estimated to be 23.0 eV. Since E_x''s do not change much from the gas-phase ones, the effective ionization energies of the 2s levels near the surface are estimated to be $23.0 - 20.6 = 2.4$ eV for He*(2^1S) and $23.0 - 19.8 = 3.2$ eV for He*(2^3S). The energy diagram of MoS_2 and He* is shown in Figure 33, where the valence band width is derived from the angle-resolved photoemission data[168] and the band gap is referred to the absorption edge of 1.35 eV.[170] As is seen in Figure 33, the 2s levels of He* are located opposite empty states composed of the Mo 4d and S 3p orbitals. Thus, the RI process is energetically possible. Furthermore, the band calculations indicate that the density of the corresponding empty states is very high. Owing to these features the RI+AN mechanism becomes dominant on the MoS_2 surface.

Next, we proceed to the assignment of the AN spectra. Using the one-electron binding energies of the Mo 4d and S 3p-derived states obtained by the photoemission data, the weak tail structure in Figure 32 can be attributed to the two-holes in the defect levels and Mo $4d_{z^2}$ states, i.e., $(\text{def})^{-2}$ and $(\text{Mo } 4d_{z^2})^{-2}$. The intense bands X and Y are assigned to the two-

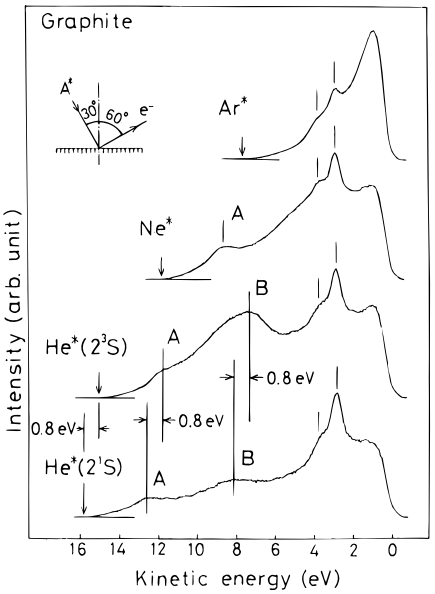

Figure 34. Electron emission spectra of a graphite surface using the He*(2^1S and 2^3S), Ne* and Ar* atoms. (Reprinted with permission from ref 93. Copyright 1990 The American Physical Society.)

hole states of the S 3p-derived bands, $(S\ 3p)^{-2}$, and correspond reasonably to a broad structure observed in the core−valence−valence (LMM) Auger spectrum. The strong suppression of the $(Mo\ 4d_{z^2})^{-2}$ state is partly due to the low density of the Mo $4d_{z^2}$ states. However, the main reason probably lies in the fact that the Mo $4d_{z^2}$ state is shielded effectively by the outermost S layer (layer distance $d_{S\text{-}Mo} = 1.59$ Å) against collisions of the He^+ ions. Strictly speaking, the latter effect is derived from two factors: (i) the Mo $4d_{z^2}$ orbital extends normal to the S layer but is rather contracted owing to the nuclear charge of Mo^{2+} and (ii) the Mo $4d_{z^2}$ orbital is atomic like in character and therefore cannot be exposed further outside the surface by mixing with the S orbitals. A similar feature has been found in the PI spectrum of gaseous ferrocene $Fe(C_5H_5)_2$, in which Fe is formally divalent cation and its 3d-derived MO's are shielded well by a pair of rings of cyclopentadienyl anions $(C_5H_5)^-$, yielding weaker bands compared with the ligand bands.[171,172] It should be noted that the strong suppression of metal d states is not seen in the case of dibenzenechromium $Cr(C_6H_6)_2$ where the Cr atom is sandwiched two benzene rings but its formal charge is neutral.[172]

c. Graphite. Graphite is also a typical layer compound with the interlayer distance $d_{CC} = 3.35$ Å and hence, its electronic structure is essentially two dimensional. The valence bands of graphite are characterized by two different types, π bands composed of pure C $2p_z$ orbitals and σ bands based on sp^2-hybridized C 2s, $2p_x$, and $2p_y$ orbitals. The π and σ bands exhibit characteristic energy dispersion (binding energy vs wave vector) as is well known by angle-resolved photoemission measurements.[173] Further, they are considered to have different spatial electron distributions reflecting the amplitude of the wave functions.

Figure 34 shows the electron emission spectra of graphite obtained by the He*(2^1S and 2^3S), Ne*, and

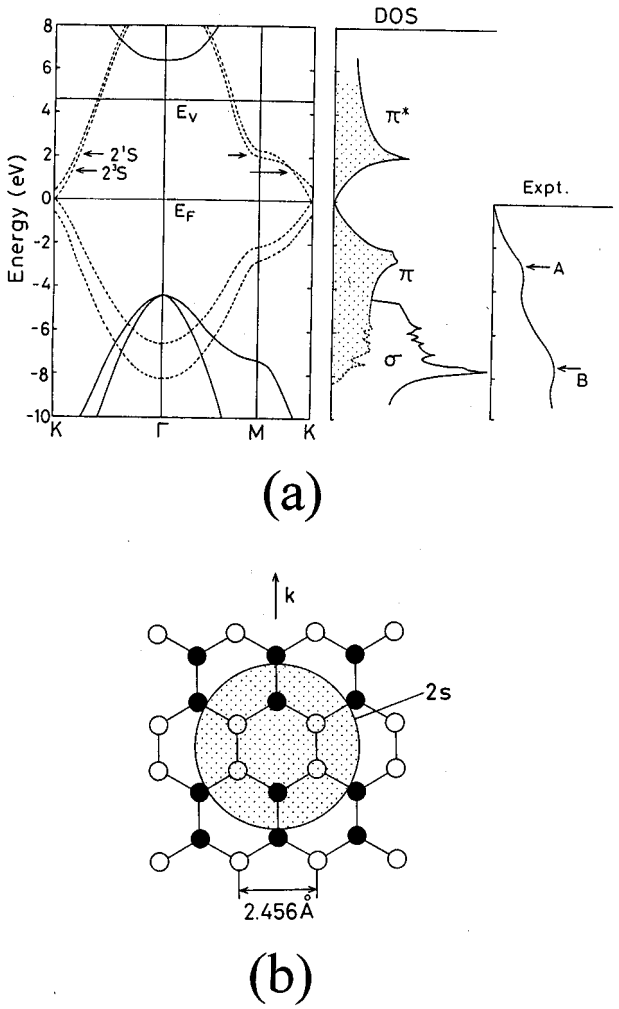

Figure 35. (a) Theoretical band structure, density of states, and He*(2^1S) spectrum of graphite. The arrows in the band structure denote the positions of the 2s levels for He*(2^1S) and He*(2^3S) atoms near the surface, and (b) schematic view of the π^* wave function at the symmetry point *M* together with the 2s atomic orbital of the He* atom. (Reprinted with permission from ref 93. Copyright 1990 The American Physical Society.)

Ar* metastable atoms.[93] In contrast to the cases of Si(111) and MoS_2, the threshold and the peaks (labeled A and B) in the two He* spectra shift with each other by the difference in the excitation energy; $20.6(2^1S) - 19.8(2^3S) = 0.8$ (eV), indicating the operation of the PI process. With decreasing the kinetic energy E_k, the background due to "true secondary" rises up continuously. Two stationary peaks at $E_k = 2.9$ and 3.8 eV appeared in all spectra are attributed to final-state structures, reflecting the high density of σ^* conduction bands above E_F.

Figure 35a shows the theoretical band structure for three-dimensional graphite and the DOS calculated using the approximation by discrete-variational Xα linear combination of atomic orbitals.[174] In the figure, the solid and dotted curves represent σ and π bands, respectively. Graphite is semimetal with no band gap below the vacuum level and has empty levels at the energy position corresponding to that of the 2s level. In this respect the operation of the PI process seems puzzling at first sight, because the RI+AN process is expected to occur preferentially on the surface. This problem can be solved taking into

account the transition matrix element of the RI process determined by the overlap between the He* 2s orbital and unoccupied orbitals of graphite. As shown in Figure 35a, the He* 2s levels lie in the π^* bands near the symmetry points M ($k = 1.48$ Å^{-1}) and K ($k = 1.71$ Å^{-1}) in the Brillouin zone, if we take the image potential effect ΔE_i to be -1.5 eV (cf., eq 25). At point M, all rows of the carbon atoms perpendicular to $\boldsymbol{k}$ have the same phase, but each double row shows a phase change (see Figure 35b). Since each carbon atom is thus surrounded by two atoms of the opposite phase and one atom of the same phase, the wave function at M cannot give an effective overlap with widely extending 2s orbital of He*. A similar argument can be made for the π^* wave function at K.

From the comparison between the calculated DOS and the MAES, it is found that (i) the observed maxima A and B relate closely to the π DOS maxima derived from the flat parts near the symmetry point M and the bottom at Γ, respectively, and (ii) the steep hump at -4.5 eV based on the σ bands is almost missing. This is because the π functions (composed of C $2p_z$ orbitals) protruding normal to the surface overlap effectively with the 1s orbital of He* and give a large cross section for Penning ionization. On the other hand, the sp^2-hybridized σ functions distributed parallel to the surface and screened by the π functions yield little contribution to the PI process.

d. $LaCoO_3$. The appearance of so-called satellites in valence-band photoemission is regarded as a direct evidence for the break-down of the one-electron picture when we describe the electronic structure of solids. Since the first observation in Ni, such satellites have been extensively studied in transition metals and their compounds in connection with many-electron effects, i.e., electron−electron correlation, charge fluctuation, etc. So far the origin of satellite has been studied mainly through the binding energy analysis and the resonance-like behavior of photoemission. It is expected that the many electron problem can be treated in a different way by the use of MAES, since metastable atoms cause the local ionization at a solid surface. Now we take an example of semiconducting $LaCoO_3$. It is a typical perovskite oxide of the type ABO_3, where B is a transition metal ion occupying octahedral sites.

Figure 36 shows the He*(2^3S) and He I spectra of polycrystalline $LaCoO_3$.[94,95] Photoemission bands 1 and 2 are assigned to the Co 3d-derived main states, bands 3 and 4 to the O 2p-derived states, and band 5 to the Co 3d-derived satellite. The corresponding bands also appear in the He* spectrum, which indicates that He* atoms decay on the surface via the PI process. The characteristics of the He* spectra are summarized as follows:

(i) The Co 3d-derived main bands are strongly suppressed relative to the O 2p-derived bands.

(ii) The Co 3d-derived satellite is greatly enhanced relative to the other bands.

Within the simple model for the PI process, the transition rate is governed essentially by the differential overlap between the valence wave function and He* 1s orbital. Therefore, an orbital exposed outside the surface gives more effective overlap with

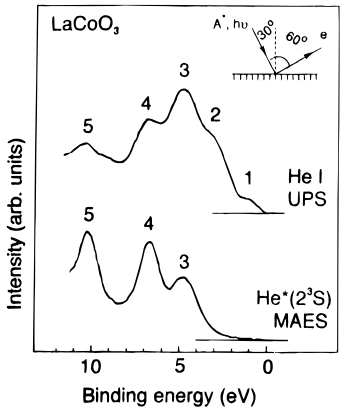

Figure 36. Electron emission spectra of a $LaCoO_3$ surface using the He I resonance line and He*(2^3S) atoms. (Reprinted with permission from ref 95. Copyright 1993 The American Physical Society.)

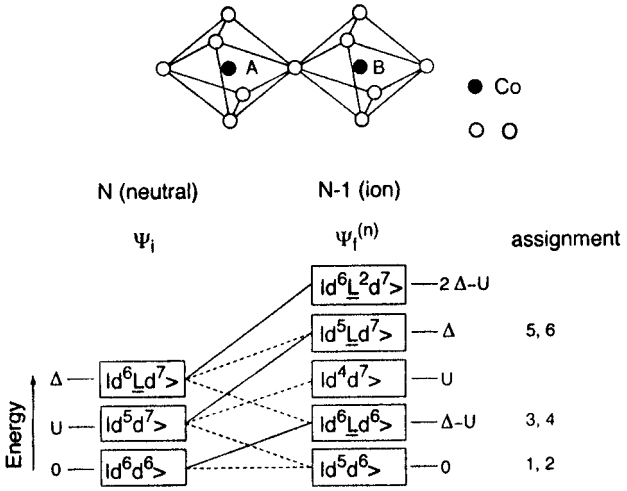

Figure 37. Simple model of the initial and final configuration interactions using a Co_2O_{11} cluster. Solid and dotted lines denote passes from O 2p emission and Co 3d emission, respectively. (Reprinted with permission from ref 95. Copyright 1993 The American Physical Society.)

the He* 1s orbital than an orbital localized on the surface, yielding a stronger band in MAES. In $LaCoO_3$, the formally trivalent Co cation is present inside the surface, being coordinated by O anions located at the surface. Further the 3d orbitals of Co^{3+} are contracted spatially taking its small ion radius into account ($r_{Co^{3+}} \approx 0.63$ Å, $r_{O^{2-}} \approx 1.40$ Å). Consequently, the incoming He* atom interacts effectively with the outer-distributed O 2p orbitals, but very little with the inner-distributed Co 3d orbitals, in accordance with the experimental result (i) mentioned above. A similar discussion was made in the case of MoS_2.[94]

In order to interpret the satellite enhancement in the MAES, we will consider a cluster including two Co ions, $O_5Co_AOCo_BO_5$ shown in Figure 37,[95] where Co_A and Co_B ions are surrounded by octahedral O anions. Then, the initial-state wave function may be described by

$$\Psi_i = a_0|d^6d^6\rangle + a_1|d^6\underline{L}d^7\rangle + a_2|d^5d^7\rangle \quad (32)$$

The first term denotes the ground-state configuration. The second term is a configuration of a charge transfer (CT) type and is characterized by the

O2p→Co3d transfer energy Δ. The third term introduced here represents a configuration of Mott−Hubbard (MH) type produced by the transfer of a d electron from Co_A to Co_B sites or by the reverse process. The transfer energy of this type *U*, which is characterized by the d−d electron repulsion, is estimated to be 17.8 eV for free Co^{3+} ion from the difference in the ionization energy between Co^{2+} and Co^{3+} ions. In the solid phase, however, *U* is considered to decrease down to several electron volts, owing to the Madelung potential from the lattice and also polarization effects due to the electron transfer, which makes the MH-type configuration to mix sufficiently with the ground-state and CT-type configurations. On the other hand, the final-state wave functions $\Psi_f^{(n)}$ are described by a set of following combinations:

$$\Psi_f^{(n)} = b_0^{(n)}|d^5d^6\rangle + b_1^{(n)}|d^6\underline{L}d^6\rangle + b_2^{(n)}|d^5\underline{L}d^7\rangle + b_3^{(n)}|d^4d^7\rangle + b_4^{(n)}|d^6\underline{L}^2d^7\rangle \quad (33)$$

where each term is made up via one-electron emission from the configurations in Ψ_i, the relation being summarized in Figure 37. It should be noted that the $|d^5\underline{L}d^7\rangle$ state relating mainly to the satellite can be formed either by a Co 3d emission from the CT-type $|d^6\underline{L}d^7\rangle$ or by an O 2p emission from the MH-type $|d^5d^7\rangle$ in Ψ_i, whereas the $|d^6d^5\rangle$ leading to the main bands is produced only by a Co 3d emission from the ground $|d^6d^6\rangle$ or MH-type $|d^7d^5\rangle$ in Ψ_i. As mentioned above, the transition rate of PI is much larger for the outer-distributed O 2p orbitals than for the inner-distributed Co 3d orbitals. Therefore, the transition pass via the O 2p emission ($|d^5d^7\rangle \rightarrow |d^5\underline{L}d^7\rangle$ gives a strong satellite band in MAES, while the passes via the Co 3d emission give weak main bands, in agreement with the present experimental results. In other words, the data indicate that the MH-type CI in the initial state for a cluster involving two Co ions plays a dominant role in the appearance of the multi-electron satellite in MAES. The $|d^6\underline{L}d^6\rangle$ state leading to the O 2p-derived bands is produced by an O 2p emission from the ground $|d^6d^6\rangle$ or a Co 3d emission from the CT-type $|d^6\underline{L}d^7\rangle$ in Ψ_i. This indicates that the O 2p-derived states also appear as stronger bands in the spectrum.

4. Insulators

In the insulator surface, the energies of the highest occupied levels of the rare-gas metastable atoms fall into the band gap, and hence, only the PI process takes place, providing direct information on the outermost surface layer. In this section we will describe the MAES of alkali halide and solid xenon.

a. Alkali Halides. Munakata et al.[175] first measured the Ne* and He* spectra of the evaporated thin films of alkali halides (LiF, LiCl, LiBr, NaF, and NaCl). From the comparison with the photoemission spectra, they found two features. First, the peak positions of the valence bands in the MAES are shifted to the lower binding energy side from the corresponding photoemission peaks by 0.1−1.5 eV. These shifts are caused partly by a strongly attractive potential between the rare-gas atoms in the ground state and the ionized solid surface. However, the main reason probably comes from the fact that the occupied states at the surface are located at higher levels than the valence states in the bulk, reflecting the difference in the Madelung potential between the surface and bulk. Second, the relative intensity of true secondary emissions is much enhanced when the energy of the metastable atom exceeds twice the band gap energy, i.e., when the electron-electron scattering of Penning electrons in the solid is feasible.

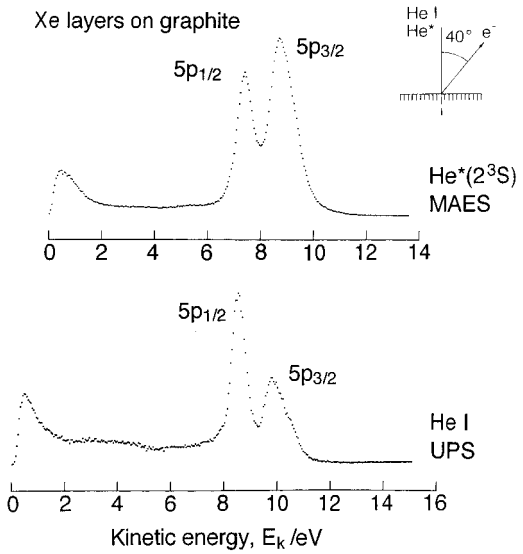

Figure 38. Electron emission spectra of solid Xe obtained by the He I resonance line and He*(2^3S) atoms. (Reprinted with permission from ref 180. Copyright 1995 Elsevier.)

Kempter et al. examined in detail NaCl,[176,177] LiF,[86] and CsI[178,179] adlayers formed on a W(110) surface as a function of the amount of deposition. They obtained the same conclusion as that of Munakata et al. with respect to the peak shifts observed in the He* spectra. Further they found that the layer growth is initiated by molecular adsorption and followed by the formation of islands composed of molecules (see section IV.C.2).

b. Solid Xe. Figure 38 shows the He I and He*-(2^3S) spectra of a Xe multilayer produced by 100 L exposure to a graphite surface at 30 K.[180] Two bands in the He I spectrum are attributed to emissions from the Xe $5p_{3/2}$ and $5p_{1/2}$-derived bands. The $5p_{3/2}$ band is somewhat broader than the $5p_{1/2}$ band because, at the surface, the $5p_{3/2}$-derived level split into the $M_j = +3/2$ and $+1/2$ sublevels owing to the lateral interactions between neighboring atoms,[181] where M_j is the magnetic quantum number of the total angular momentum of the atomic state. With decreasing the kinetic energy of emitted electrons, E_k, secondary electrons produced in the Xe layers and graphite substrate rises up continuously in the He I spectrum.

The Xe 5p-derived bands also appear in the He*-(2^3S) spectrum, indicating that metastable atoms deexcite on the surface via the PI process, as in the gas-phase He*(2^3S)-Xe collision.[182] The occurrence of the PI process on Xe layers has been confirmed directly by recent spin-dependent measurements by Oró et al., who found that the spin polarization of ejected electrons is conserved when spin-polarized He*(2^3S) atoms impinge on Xe layers on Cu(100)[52] and Au(100),[135] i.e.,

$$He^*(2^3S,1s\uparrow 2s\uparrow) + Xe(\uparrow\downarrow) \rightarrow He(1^1S,1s\uparrow\downarrow) + Xe^+(\uparrow) + e^-(\uparrow) \quad (34)$$

In this process, a Xe 5p electron with down spin fills the He* 1s hole and the He* 2s electron with up spin is ejected to the vacuum simultaneously.

The characteristics of the He*(2^3S) spectrum are summarized as follows:

(i) The intensity ratio of the Xe $5p_{3/2}$- and $5p_{1/2}$-derived bands is about 2:1, which is much different from the case of photoemission. This is because in Penning ionization the *k* conservation rule is smeared out in contrast with the photoemission process and the local density of states is reflected in the He*(2^3S) spectrum.

(ii) The intensity of the secondary emission is rather low compared with the case of the photoemission. This is based on the fact that He* atoms deexcite just outside the surface and electron emission occurs mainly in the backward direction.

From comparison with the gas and solid-phase MAES, Yencha et al. indicated that the rare-gas metastables are deexcited on molecular solids of H_2O and NH_3 mainly via PI.[183] Using the spin-labeling technique, Dunning and his collaborators showed conclusively that the metastables are deexcited on thick condensed layers of Ar,[52] CO_2,[184] and H_2O[184] almost completely via PI and on those of O_2,[184] Cl_2,[184] and NO[135] partially via PI, as in cases of the gas-phase collisions. The occurrence of the PI process is seen in ordinary organic solids and will be described in section V.

B. Adsorbed Surfaces

1. Carbon Monoxide

The unique feature of MAES that provides selective information on the outermost surface layer is especially useful for the study of the electronic states of molecular adsorbates. In this section, we deal firstly with carbon monoxide adsorbed on metal surfaces, because this system is regarded as a prototype of molecular adsorption and also Penning ionizations of CO[62,182,185−190] and transition-metal carbonyls[190,191] are well studied in the gas-phase. After a brief review of the results of free CO and transition-metal carbonyls, we present and discuss the MAES of CO adsorbed surfaces, which include the deexcitation channel of incident metastable atoms, the relative intensity of CO-derived bands, and a structure observed near the Fermi level.

As is well-known the ground-state electron configuration of CO is $(1\sigma)^2(2\sigma)^2(3\sigma)^2(4\sigma)^2(1\pi)^4(5\sigma)^2(2\pi^*)^0$. Here, the 1σ and 2σ orbitals are essentially composed of the O 1s and C 1s atomic orbitals, respectively, and the 3σ orbital is derived mainly from the O 2s orbital. The 4σ and 5σ orbitals are lone-pair-type orbitals located mainly on the O and C atoms, respectively. The 1π orbital is a bonding orbital with electron distribution inclined toward the O atom. The $2\pi^*$ orbital is the lowest unoccupied orbital mainly distributed on the C atom.

Figure 39 shows the electron emission spectra of free CO by the He*(2^1S and 2^3S) atoms and the He I resonance line.[190] These spectra exhibit a series of relatively sharp peaks, which are assigned to the $X^2\Sigma^+$, $A^2\Pi$, and $B^2\Sigma^+$ states of the product CO^+ ion (hereafter we use the conventional notation, the CO 5σ, 1π, and 4σ states, respectively). The characteristics of the MAES of CO are summarized as follows:

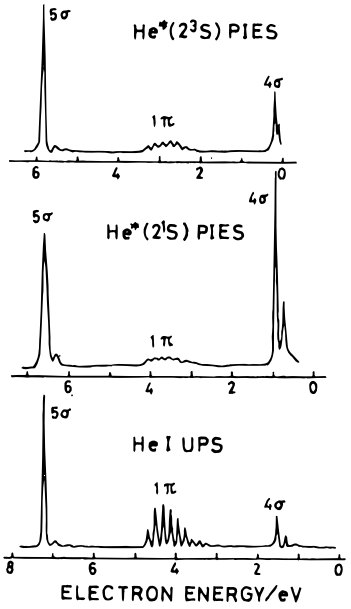

Figure 39. Penning ionization electron spectra of gaseous CO obtained by He*(2^3S) and He*(2^1S) atoms and the He I photoemission spectrum. (Reprinted with permission from ref 190. Copyright 1983 The American Physical Society.)

Table 2. Relative Populations of the Ionic States for Penning Ionization of CO

	$X^2\Sigma^+$	$A^2\Pi$	$B^2\Sigma^+$	ref
He*(2^1S)	100		104	186
	100	35	96	190
He*(2^3S)	100	43		185
	100	38		186
	100	40	43	62

(i) The ionization potentials of free CO obtained by the asymptotic excitation energies for He*(2^1S and 2^3S) are almost identical with those from the photoemission spectrum within <0.05 eV.[185−187] The ionization via the covalent channel was confirmed by a spin-polarized measurement.[188]

(ii) The relative band intensities in the Penning spectra are listed in Table 2. Although they depend on the emission angle of Penning electrons[182] and the collision energy,[189] the 5σ and 4σ bands are generally stronger than the 1π in the He*(2^1S) and He*(2^3S) spectra. The only exception is the weak feature of the 4σ band in the He*(2^3S) spectrum, which may arise from the fact that the excitation energy of He*(2^3S), 19.82 eV, is not enough to yield the overall CO 4σ structure with the vertical ionization energy of 19.72 eV.

(iii) The angular distribution of Penning electrons emitted by the CO−He*(2^3S) collision is highly anisotropic, that is, the backward scattering (the direction of the incoming He*) is dominant.[182]

In transition metal carbonyls the metal−CO bonding has been described in terms of a two-electron transfer,[192] i.e., the donation of a CO 5σ electron to the transition-metal d* virtual orbital and the back-donation of a transition-metal d electron to the CO

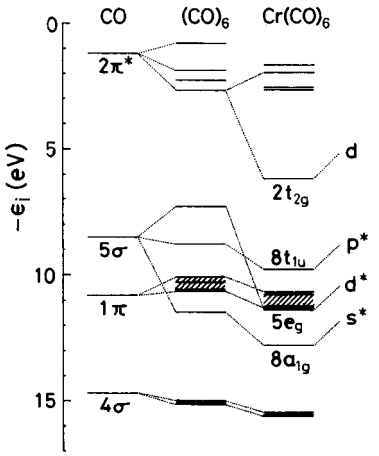

Figure 40. The calculated energy diagram for CO, hypothetical $(CO)_6$, and $Cr(CO)_6$.

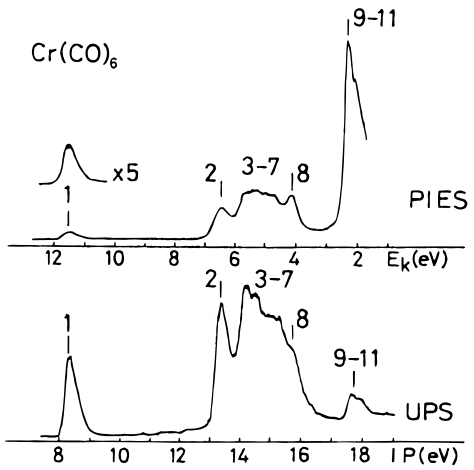

Figure 41. Penning ionization electron spectra of gaseous $Cr(CO)_6$ using He*(2^3S) atoms and the He I resonance line. (Reprinted with permission from ref 191. Copyright 1992 The American Physical Society.)

$2\pi^*$ empty orbital. In order to manifest these interactions, the calculated energy levels for CO, $(CO)_6$, and $Cr(CO)_6$ by Johnson and Klemperer[193] are reproduced in Figure 40, where $(CO)_6$ is a hypothetical complex with the same geometry as $Cr(CO)_6$ except for the absence of a Cr atom. In the diagram, the changes in the energy levels from CO to $(CO)_6$ are attributed to the ligand−ligand (through-space) interactions, while those from $(CO)_6$ to $Cr(CO)_6$ are based on the metal−ligand (through-bond) interactions. On going from CO to $(CO)_6$, the CO 5σ orbital yields three sets of MO's, i.e., the e_g, t_{1u}, and a_{1g} orbitals. The e_g state is significantly stabilized in $Cr(CO)_6$, owing to the mixing of the 5σ orbital with the Cr 3d*(e_g) virtual orbital, which corresponds to the donation effect. It is of note that the a_{1g} state is more stable than the t_{1u} and e_g, indicating the importance of the through-space interaction among the CO 5σ orbitals. The CO 4σ level also splits into three on going from CO to $Cr(CO)_6$, but the splitting is rather small because of its low orbital energy and electron localization. The CO 1π (and $2\pi^*$) orbital gives rise to four sets of MO's in $(CO)_6$. The $2\pi^*$-derived t_{2g} orbital hybridizes strongly with the Cr 3d orbitals with the same symmetry, forming the $2t_{2g}$ MO in $Cr(CO)_6$. The charge transfer produced by this interaction is referred to the back-donation.

Figure 41 shows the comparison between the He I and He*(2^3S) spectra of gas-phase $Cr(CO)_6$.[191] In the UPS, band 1 is assigned to the $2t_{2g}$ state that is predominantly Cr 3d in character with some CO $2\pi^*$ contribution, while bands 2−8 and 9−11 are related to CO $5\sigma/1\pi$-derived states and CO 4σ-derived states, respectively.[194] The corresponding bands also appear in the He* spectrum but the relative band intensity is considerably different. The features of the He* spectrum are summarized as follows:

(i) Band 1 is very suppressed compared with the CO-derived bands. This is because the $2t_{2g}$ MO is localized mainly on the Cr atom surrounded by six CO ligands and cannot interact with incoming He* atoms effectively. A similar shielding effect has been observed in the He* spectra of gas-phase $Fe(CO)_5$,[190] $Mo(CO)_6$,[194] and $W(CO)_6$.[194]

(ii) The intensity ratio of the CO $5\sigma/1\pi$ and 4σ-derived bands is about 1:1, although the corresponding ratio for free CO is 1:0.31 (see Table 2). This means that the transition rate for the CO 4σ-derived orbitals is about three times larger than that for the CO $5\sigma/1\pi$ orbitals, if we take the orbital number into consideration. This can be interpreted by the fact that the CO 4σ-derived orbitals in $Cr(CO)_6$ are localized largely on the O atoms located outside the molecule and hence interact with He* preferentially.

(iii) Among the CO 5σ-derived bands, band 8 due to the $8a_{1g}$ state is much stronger than band 2 due to the $8t_{1u}$, taking their orbital degeneracy into account. This is because the $8a_{1g}$ MO is spatially expanded owing to the through-space interaction among the CO 5σ orbitals.

Next we discuss the MAES of CO adsorbed on metal surfaces in relation to the results of gaseous CO and metal carbonyls. Since the pioneering work on the CO-covered Pd(111) surface by Conrad et al.,[24] the MAES has been extensively applied to various systems, which involve CO on clean Ni(110),[125,126] Ni(111),[27,74,195−197] Cu(110),[198] Mo(110),[25,199] Ru(0001),[200] Pd(110),[38,127,198] Ag(110),[134] and W(110)[201] surfaces and on precovered metal surfaces such as O/Ni(111),[196] K/Ni(111),[197,202−204] Cu/Ru(0001),[200] Li/Ag/Ru(0001),[205] Ag/Ru(0001),[205] K/Ru(0001),[206,207] and K/W(110).[201]

As a typical example of strong chemisorption, we take up here the CO-covered Pd(110) surface. This system exhibits an imperfect c(4×2) LEED (low-energy electron diffraction) pattern at saturation coverage($\theta_{CO} \approx 0.75$). The structure models are shown in Figure 42, where the CO molecules form close-packed rows along the [110] direction and each CO stands up on the surface with the C atom pointing down to the surface. Figure 43a shows the electron emission spectra of the CO/Pd(110) at $\theta_{CO} \approx 0.75$ excited by the He I resonance line and He*(2^1S) metastable atoms.[38] In the He I spectrum the threshold of emission at $E_k = 15.0$ eV corresponds to the Fermi level E_F. In addition to strong emissions from the Pd 4d valence bands just below E_F, two weak maxima are seen at 7.8 and 10.7 eV below E_F and are attributed to the CO $5\sigma/1\pi$ and 4σ-derived states, respectively. The He*(2^1S) spectrum, on the other hand, reveals only two prominent peaks arising from the CO $5\sigma/1\pi$- and 4σ-derived states (albeit a strong

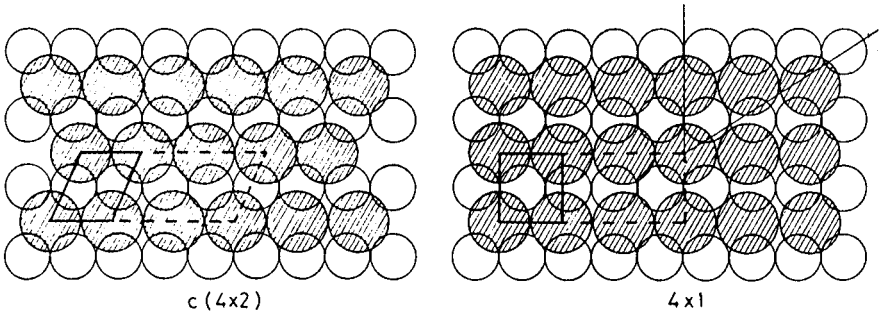

Figure 42. Structure model for CO adsorbed on Pd(110) ($\theta_{CO} = 0.75$), showing two limiting cases for the mutual configuration of parallel chains of adsorbed CO. (Reprinted with permission from ref 38. Copyright 1982 Elsevier.)

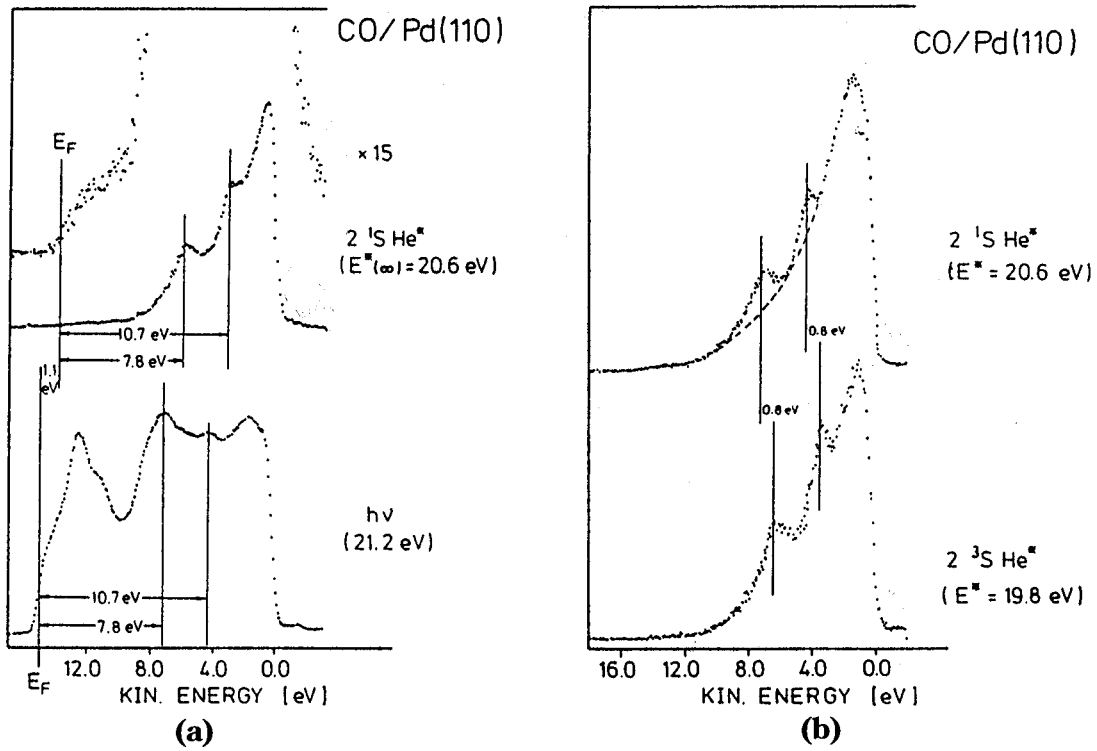

Figure 43. (a) Electron emission spectra of a CO covered Pd(110) surface at $\theta_{CO} = 0.75$ obtained by the He I resonance line (21.2 eV) and He*(2^1S, 20.6 eV) atoms, and (b) those obtained by the He*(2^1S) and He*(2^3S, 19.8 eV) atoms. (Reprinted with permission from ref 38. Copyright 1982 Elsevier.)

superimposed background). When the onset at $E_k =$ 13.9 eV is identified as the Fermi level, the binding energies of the CO 5σ/1π- and 4σ-derived states are 7.8 and 10.7 eV, in agreement with the results of the He I spectrum. This indicates that the He*(2^1S) atoms are deexcited on the CO-covered Pd(110) via the PI process, instead of the RI+AN process on the clean surface. The operation of the PI process is further confirmed by comparison between the He*(2^1S) and He*(2^3S) spectra shown in Figure 43b. The CO-derived peaks in the He*(2^3S) spectrum shift to lower kinetic energies by about 0.8 eV with respect to those in the He*(2^1S) spectrum, reflecting the difference in the excitation energies of free He* (20.6 eV for 2^1S and 19.8 eV for 2^3S). The features in the He I and He*(2^1S) spectra should differ in the E_k scale just by the difference in their energies, i.e., 21.2 − 20.6 = 0.6 (eV). The actual difference is, however, 1.1 eV, which indicates that the effective excitation energy of He*(2^1S) (as well as He*(2^3S)) is reduced by 0.5 eV in front of the surface. This is possibly because the incoming potential between He* and a chemisorbed CO is rather attractive in contrast to the case of He*-free CO collision. The image force effect may cause a lowering of the potential energy when the highly polarizable He* approaches up to about 5 Å from the metal nuclei.[38,198]

As an example of a weakly chemisorbed system, the He I and He*(2^1S and 2^3S) spectra of CO/Cu(110) are shown in Figure 44.[198] The CO was adsorbed at 140 K and at the maximum coverage ($\theta_{CO} \approx 0.77$). A weak Cu 4s band emission just below E_F and the following strong Cu 3d band emission are clearly seen in the He I spectrum, while the He* spectra exhibit essentially only emissions from the CO-derived states. The peak shifts in the 2^1S and 2^3S spectra indicates the operation of the PI process. In the photoemission spectrum of a weakly chemisorbed system it is known that the satellite band due to the many-electron effect appears in the higher binding energy side of the 4σ-derived band.[208] However, such a satellite line has not been detected in the metastable spectra owing to the strong background and/or the low ionization cross section.

Before an analysis of the CO-derived states, we should mention the source of strong background

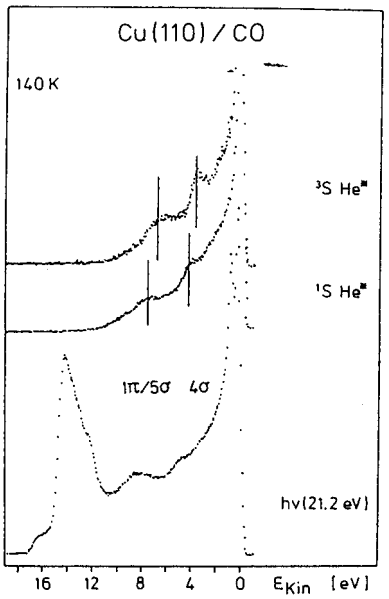

Figure 44. Electron emission spectra of a CO covered Cu(110) surface at $\theta_{CO} = 0.77$ using the He I resonance line and He*(2^1S and 2^3S) atoms. (Reprinted with permissiond from ref 198. Copyright 1984 Elsevier.)

commonly observed in CO/metal systems. In the case of the CO/Pd(110) in Figure 43, the magnitude of the background is about 10 times stronger than the sum of the two PI bands. This is in striking contrast to the cases of the transition-metal carbonyls (Figure 41). Roussel et al. pointed out that this is partly due to experimental conditions such as an effect of the transmission coefficient of the electron analyzer.[74] However, even in their transmission-corrected spectrum of the CO/Ni(111), the background is roughly five times stronger than the PI signals. One of the sources of the intense background is the effect of secondary electrons as in photoemission. Wang calculated the angular distribution of Penning electrons from the CO overlayer and suggested that a high fraction of the electrons is emitted into the solid to yield secondary electrons.[209] According to the angle-resolved measurement,[38] however, most Penning electrons from the CO-derived states are emitted to the backward direction (direction of the incoming He*). Therefore, the secondary emission is considered to be weak in the PI process as in the case of Xe multilayers (see Figure 38). The second and more probable candidate for the strong background is the contribution from the RI+AN process operating parallel to the PI process. If the RI process proceeds on the CO-covered surface, the following AN process will give rise to electron emissions whose intensity gradually rises up with decreasing the kinetic energy. In fact such a feature is reproduced well in the He^+ ion neutralization spectrum of the CO/Ni(111) surface.[210] A detailed discussion of the PI vs RI+AN processes depending on the size and/or molecular orientation of the adsorbate was reported in the literature.[196,198] The third source of the strong background is the Auger neutralization of the CO^+ ion left at the surface after impact of metastables; a valence electron transfers from the surface into the hole of the CO^+ ion and another electron is emitted to the vacuum.[27] In CO/Pd(110), since the binding energies of the CO $5\sigma/1\pi$ and 4σ-derived states

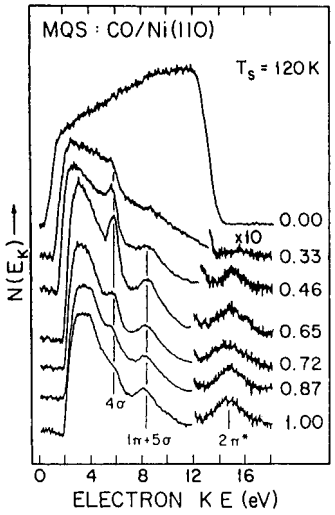

Figure 45. Metastable atom electron spectra of CO adsorbed on a Ni(110) surface using the He*(2^1S) atoms. The coverage θ_{CO} is shown in right side of each spectrum. (Reprinted with permission from ref 126. Copyright 1985 Elsevier.)

referred to E_F are $E_B = 7.8$ and 10.7 eV, respectively, and also the work function is $\Phi = 6.2$ eV, Auger electrons are expected to appear below the kinetic energies of 1.6 and 4.5 eV (when two electrons at E_F are involved in the transition, the emitted electron has the maximum kinetic energy given roughly by $E_B - \Phi$). As a consequence this mechanism may contribute substantially to the lower kinetic energy part of the background.

Next we discuss the relative intensity of CO-derived bands. The $5\sigma/1\pi$:4σ intensity ratio for weakly chemisorbed CO on Cu(110) (at $\theta_{CO} \approx 0.77$ and 140 K) is about 1:1,[198] which is very close to the case of gaseous $Cr(CO)_6$.[191] For the strongly chemisorbed system, this ratio usually rises up to 1.5:1 for CO/Pd(110) ($\theta_{CO} \approx 0.75$, 300 K),[198] 1.9:1 for CO/Ni(111) ($\theta_{CO} \approx 0.5$, 300 K),[74] 2.5:1 for CO/Pd(111) ($\theta_{CO} \approx 0.66$, 140 K),[198] and 4:1 for CO/Pd(111) ($\theta_{CO} \approx 0.5$, 300 K).[198] Further, for CO on Li-preadsorbed Ag layers which is regarded as a physisorbed or very weakly chemisorbed system, the 5σ-derived band is almost missing while the CO 4σ- and 1π-derived bands are clearly seen.[205] If we assume that the CO 4σ and 1π orbitals are scarcely perturbed upon chemisorption, these data may indicate that the 5σ-derived orbital of chemisorbed CO extends much further outside the surface by mixing with metal d orbitals and that its tendency is more remarkable in the strongly chemisorbed system than in the weakly one. In fact, a cluster calculation of the CO/Ni system predicts that the electron distribution of the 5σ-derived orbital is strongly perturbed and exposed outside the oxygen atom of chemisorbed CO.[211]

Although the above discussion is focused mainly on the CO−metal interaction, the relative band intensity depends also on the orientation of CO with respect to the surface. Figure 45 shows a sequence of the He*(2^1S) spectra for CO/Ni(110) measured at various CO coverage θ_{CO}.[126] With increasing coverage the intensity of the 4σ-derived band increases until a critical coverage $\theta_{CO} = 0.66$, but decreases remarkably above it. Lee et al. interpreted this

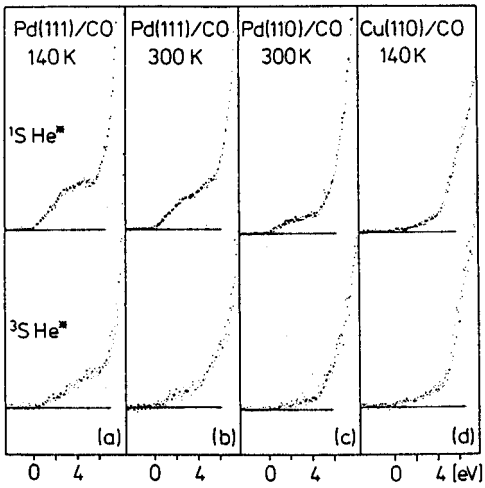

Figure 46. Metastable atom electron spectra of CO covered surfaces near the Fermi level. (Reprinted from ref 198. Copyright 1984 Elsevier.)

feature in terms of a variation of the molecular orientation, where CO molecules stand up normal to the surface below $\theta = 0.66$ and tilt to an off-normal direction above it. In the tilting orientation, the 4σ-derived orbital localized mainly on the oxygen atom of CO is close to the surface and a large fraction of incident metastables are resonantly ionized before they approach close enough to Penning ionize it. The $5\sigma/1\pi$-derived band does not decrease because the tilting tends to increase the PI intensity by increasing exposure of the 1π-derived orbital located at the side of CO against the collision of He*.

Finally, we discuss a weak structure close to E_F observed in the metastable spectra of CO-covered surfaces (see Figures 43 and 45). In order to facilitate comparison between the strongly and weakly chemisorbed systems, the expanded spectra of CO-covered Pd(111), Pd(110), and Cu(110) surfaces are shown in Figure 46.[198] A similar structure has been observed in the cases of the CO/Ni(111),[27,195−197] CO/Ni(110),[126] and CO/Ru(0001)[200] systems. This structure does not arise from the RI+AN process, because the threshold of the electron emission via the RI+AN appears at much lower kinetic energy. Further it is not assigned to the metal d or s state via the PI process, because its intensity increases with increasing CO coverage (see Figure 45) and is much enhanced when CO is adsorbed on alkali metal-preadsorbed surfaces.[197,202,207] Thus, it is established fairly well that this weak structure near E_F originates from the PI process for the chemisorbed CO molecule. However, as described in the following, the detailed assignment seems controversial at present.

The first interpretation of the weak structure near E_F is based on the Blyholder model,[212] which is essentially the same as the bonding model for transition-metal carbonyls mentioned above. In this model, by the mixing of the CO $2\pi^*$ orbitals with the substrate d orbitals, two types of states, i.e., a bonding state located below E_F with the dominant substrate d in character and an unoccupied antibonding state located high above E_F with a main component of the CO $2\pi^*$. The former state is filled and hence should be detected by MAES and UPS. On the basis of the MO picture, the Santa Barbara group assigned the MAES structure near E_F to the filled component of the $2\pi^*$. The small electron localization in the adsorbed CO may explain the low intensity of the structure. Further, Kuhlenbeck et al.[213] measured the angle-resolved UPS of CO/Ni(110) in the (2×1) ordered phase and assigned some dispersive bands in the 0.6−2.7 eV range below E_F to the CO $2\pi^*$-derived bands.

The second interpretation of the weak structure is based on the Newns−Anderson model.[214,215] This model predicts that weak or moderately strong mixing of the adsorbate $2\pi^*$ orbitals with the broad substrate bands results in the formation of virtual band of states or resonances, centered at some eV above E_F. The full width at half maximum of this band (resonances) should be several eV, leading to a tail extending below E_F and thus to a fractional electron occupancy. If such resonances are formed upon CO chemisorption on transition-metal surfaces owing to the hybridization of the CO $2\pi^*$ orbitals with the substrate s, p and d bands, the structure near E_F shown in Figure 46 corresponds to the occupied tail of a $2\pi^*$-derived resonance and therefore would be the direct evidence for the back-donation effect. In the CO/Cu(110) system the emission near E_F is much weaker compared to the CO/Pd owing to the reduced bonding strength, indicating the reduction of backdonation or $2\pi^*$ resonance occupation. A detailed discussion of CO chemisorption based on the Newns−Anderson model is reviewed by Avouris et al.[215]

Very recently the third interpretation is given by Drakova and Doyen.[216] They performed a spin-unrestricted, screened, Hartree−Fock calculation to study the interaction between He*(2^1S) and the NO-covered Pd(111) surface and made a tentative generalization of their model for CO adsorption. In this model, the incident He*(2^1S) is deexcited into the ground state via three-step processes; the resonance ionization of He*(2^1S) at large distances, the formation of He^+-CO^-/Pd(111) close to the classical turning point, and the Auger decay of the complex giving Penning-like peak of $2\pi^*$. The detail of these processes will be presented in the next section.

2. Nitrogen Monoxide

The NO molecule is paramagnetic and its electron configuration in the ground state is $(1\sigma)^2(2\sigma)^2(3\sigma)^2(4\sigma)^2(5\sigma)^2(1\pi)^4(2\pi)^1$, $^2\Pi_g$. The removal of a 2π electron leads to the $X^1\Sigma^+$ ground state of NO^+ ion while the electron emission from the 1π, 5σ, and 4σ orbitals gives rise to pronounced multiplet splittings by 2.8, 1.8, and 1.6 eV, respectively.[217] The He*(2^3S) spectrum of free NO is shown in Figure 47, and the relative band intensity is listed in Table 3.[218] It shows that the 5σ-derived states ($b^3\Pi$ and $A^1\Pi$) are stronger in intensity than the 2π and 1π-derived states ($X^1\Sigma^+$, $a^3\Sigma^+$, and $w^3\Delta$).

The electronic states of NO molecule adsorbed on metal surface have been studied by MAES, which includes NO on clean Ni(111),[74,195,196,220] Cu(110),[221] Ru(0001),[222] Pd(111),[221] and Pt(111)[221] surfaces, and on a preadsorbed O/Ni(111) surface.[196,220] The NO adsorptions on clean Ag(111) and Ag precovered Ru(0001) surfaces are also studied by MAES but NO dissociates at 90 K to form N_2O.[222]

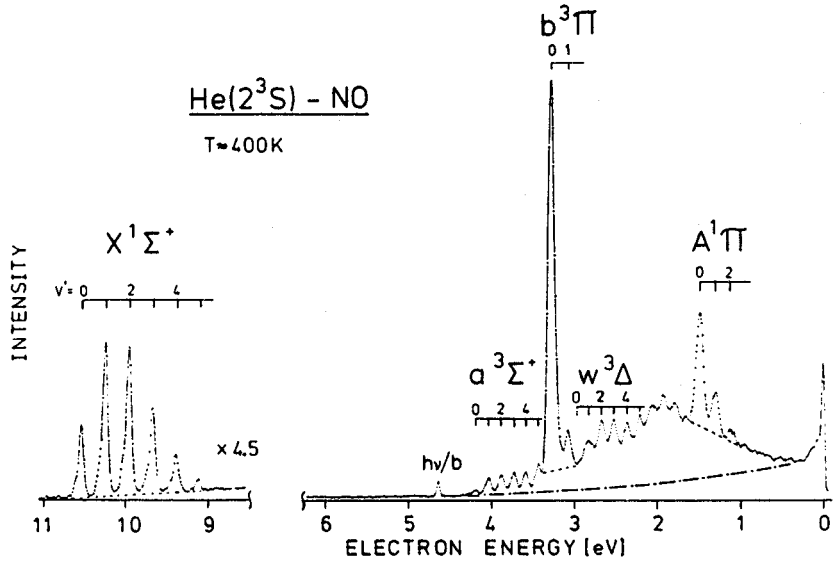

Figure 47. Penning ionization electron spectrum of gaseous NO using the He*(2^3S) atoms. (Reprinted with permission from ref 218. Copyright 1979 Elsevier.)

Table 3. Relative Populations of the Ionic States for Penning Ionization of NO (400 K)

	$X^1\Sigma^+$	$a^3\Sigma^+$	$b^3\Pi$	$w^3\Delta$	$A^1\Pi$	ref
He*(2^3S)	29		100			219
	35		100		50	186
	26	28	100	115	42	218

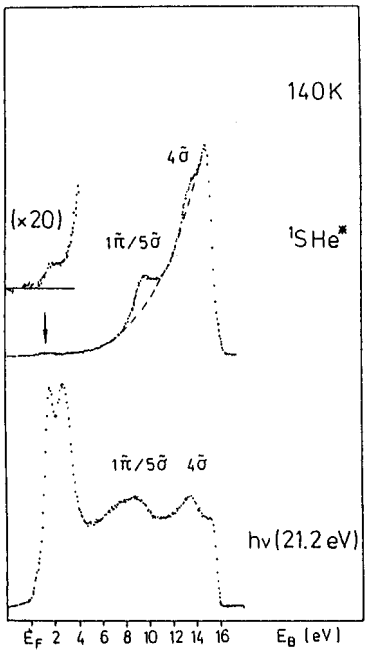

Figure 48. Electron emission spectra of NO-covered Cu(110) surface at 140 K using the He I resonance line and He*(2^1S) atoms. (Reprinted with permission from ref 221. Copyright 1988 The American Physical Society.)

Figure 48 shows the He I and He*(2^1S) spectra of NO on Pd(111) at 140 K at the saturation coverage.[221] As in the case of CO on transition-metal surfaces, the He*(2^1S) spectrum exhibits only the adsorbate 2π, $1\pi/5\sigma$, and 4σ-derived states and no contribution of the Pd 4d bands, which is dominant in the He I spectrum. The low intensity of the 2π-derived state near E_F is partly because the Penning ionization cross section is low (see Table 3). The second reason is that NO adsorbs with the N atom toward the surface. The

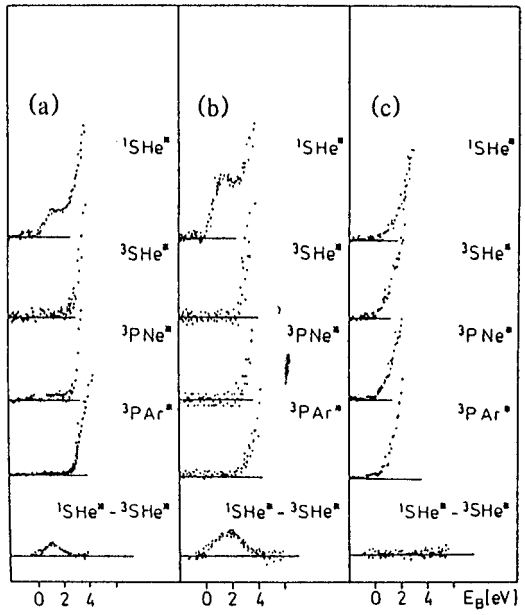

Figure 49. Metastable atom electron spectra near the Fermi level taken with different metastable atoms from (a) Pd(111), (b) Pt(111), and (c) Cu(110) surfaces saturated with adsorbed NO at 140 K. (Reprinted with permission from ref 221. Copyright 1988 The American Physical Society.)

2π orbital of NO is localized mainly at the N atom and hence is shielded geometrically by the other orbitals against collision of incident He* atoms.

Figure 49 shows the expanded spectra near the Fermi level for the Pd(111), Pt(111), and Cu(110) surfaces saturated with NO at 140 K, obtained by collisions of singlet (He*2^1S) and triplet (He*2^3S, Ne*^{3}P, Ar*^{3}P) metastables.[221] For Pd and Pt which interact weakly with NO, a distinct emission from the NO 2π-derived state is observed in the singlet spectra, while the corresponding emission is absent in all the triplet spectra. For Cu which is strongly coupled with NO, such spin-dependent emissions are not observed. In order to interpret these findings, Sesselmann et al. assumed that the spin of the 2π electron of the weakly chemisorbed NO is unpaired

on the time scale of $\sim 10^{-13}$ s (transition time in PI), namely chemisorbed NO on Pd or Pt is paramagnetic. On the basis of this assumption, they considered three-spin system composed of He*1s and 2s electrons and NO 2π electron and calculated the transition rate. Although their analysis is questionable at present, the presence of well-localized spin at the chemisorbed molecule on transition metals has received considerable attention to theoretical investigators.[216,223,224]

Drakova and Doyen[216] performed a spin-unrestricted screened Hartree−Fock calculation for the NO-covered Pd(111) surface interacting with He*-(2^1S) in order to account for the above experimental features. Their proposed model is based on the three-step deexcitation of He*(2^1S), which is shown in Figure 50. In the first step (a) the incident He*(2^1S) loses its 2s electron by resonance ionization via the diffuse unoccupied NO-derived resonances in the empty part of the Pd bands. This process takes place at large distance from the surface where the Penning ionization rate of NO is low. When the He^+ ion thus formed approaches more close to the surface, the bonding shift for all NO-derived states occurs through the electrostatic and quantum-mechanical interactions with He^+, leading to a shift of the first NO affinity level below E_F and hence to its quasiresonant occupation (see diagram b). Then the Penning-like transition can occur in the complex He^+-NO^-/Pd-(111), in which an electron of the NO-derived states fills the He^+ 1s hole and an NO 2π electron is emitted (see process c). In the final process, it is clear that the electron transfer involving two NO 2π electrons is allowed for He*(2^1S), but forbidden for He*(2^3S) since the spin of the 1s electron is parallel to those of NO 2π electrons. This model seems well to interpret the experimental feature mentioned above.

3. Hydrogen

The hydrogen molecule is usually dissociatively adsorbed on the transition-metal surfaces, on which metastable atoms are deexcited via the RI+AN mechanism. So far hydrogen chemisorption on clean Ru(0001),[225] Pd(111),[67,130] W(poly),[67,130] W(110),[42] and GaAs(110)[159] have been studied.

Figure 51 shows the AN spectra of H/Pd(111) obtained for exposures of 1, 10, and 100 L at 300 K and for ambient pressure of 1×10^{-7} Torr at 140 K.[130] The deconvolution of the spectra is shown in Figure 52, where the energy scale is the binding energy (E_B) referred to the Fermi level (E_F). With increasing exposure, the deconvoluted spectra exhibit an intensity decrease at E_F up to about $E_B = 1.5$ eV and a strong peak emerging at $E_B = 6.5$ eV. Further, the difference spectra from the clean Pd(111) show additional maxima at $E_B = 2.8$ and 4.2 eV. At 140 K the H-induced structures are much more pronounced than at 300 K which indicates additional hydrogen adsorption at low temperature. Sesselmann et al. compared the spectra with the surface density of states calculated by Louie[145] and indicated that (i) a drastic reduction of the density near E_F upon hydrogen chemisorption is due to the removal of intrinsic surface states and resonances, (ii) some of these states shift to higher binding energy and cause an enhancement of the surface density, yielding the observed maxima at $E_B = 2.8$ and 4.2 eV, and (iii) an peak at 6.5 eV originates from the bonding states between H 1s and Pd 4d orbitals.

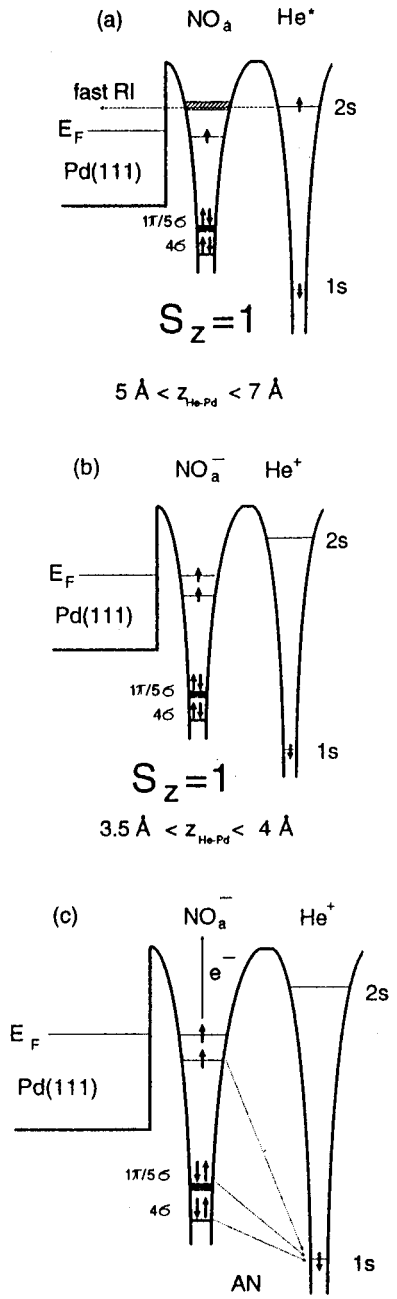

Figure 50. (a) Resonance ionization of He* in front of the NO-covered Pd(111) surface via the NO-induced unoccupied resonance states, (b) bonding shift of NO-derived states through the electrostatic and quantum-mechanical interaction with He^+, leading to a drop of the lowest-lying affinity level of NO below the Fermi level, and (c) Auger neutralization in He^+-NO^-/Pd(111) accompanied by the electron ejection from the highest occupied $2\pi^*$ level of NO^-. (Reprinted with permission from ref 216. Copyright 1994 The American Physical Society.)

On the basis of angle-resolved photoemission data it has been suggested that, on the (111) surfaces of Ni, Pd, and Pt, hydrogen adsorb at the surface above the first metal layer only at low temperatures (≤100 K), while at room temperature H atoms are incorporated under the first metal layer.[226] This conclusion was based on the fact that with UPS no additional

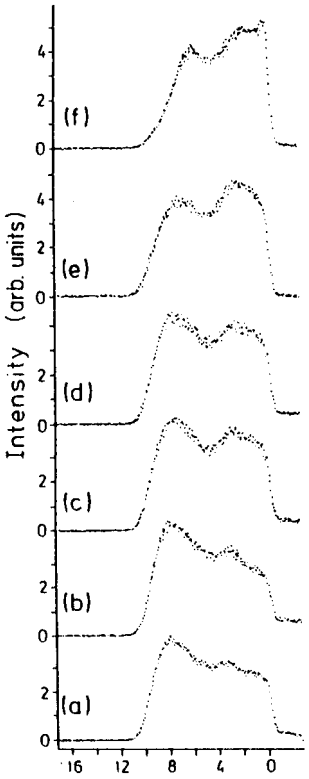

Figure 51. Metastable atom electron spectra from (a) a clean Pd(111) surface and the surfaces exposed at 300 K to (b) 1 L, (c) 10 L, (d) 100 L, (e) a constant pressure of 1 × 10^{-7} Torr, and (f) at 140 K to a constant pressure of 1 × 10^{-7} Torr hydrogen. (Reprinted with permission from ref 130. Copyright 1987 The American Physical Society.)

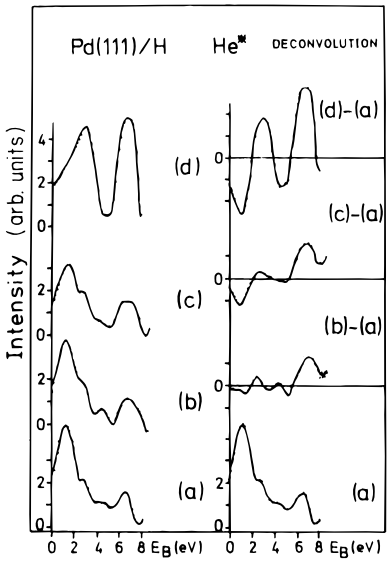

Figure 52. Deconvolution of the He* spectra of a Pd(111) surface exposed at 300 K to (a) 1 L, (b) 10 L, (c) a constant pressure of 1 × 10^{-7} Torr, and (d) at 140 K to a constant pressure of 1 × 10^{-7} Torr hydrogen. Difference spectra of the deconvolution are also shown. (Reprinted with permission from ref 130. Copyright 1987 The American Physical Society.)

emission due to the H 1s−d bonding state and only very small changes in the metal d band region were observed at room temperature. However, the above MAES data clearly show that even at room temperature hydrogen adsorption causes substantial changes in the d band region as well as outside the metal d band.

4. Alkali-Metal Atoms

The adsorption of alkali metals on a solid surface has attracted considerable attention for the MAES study from several points of view, i.e., singlet−triplet conversion, formation of core-excited anion, local work function, exoelectron emission during oxygen exposure, promotion of catalytic activities, etc. Since the former two topics were discussed in detail in section III, we focus here on the concept of the local wave function induced by a small amount of alkali atom metal on a solid surface. In higher coverage region, where coverage is still low enough to give the work function less than 2 eV, it should be noted that the analysis of the MAES (especially the structure near E_F) is not straightforward, owing to the resonance capture (RC) and subsequent autodetachment (AU) decay channel founded in 1991[29] (cf., section III.B.3). In this sense, the spectra of low work function surfaces published before the finding of the RC+AU operation (1991) should be reinterpreted.The latter two topics concerning surface reactions will be discussed in section IV.C.

As stated before, rare-gas metastable atoms such as He*(2^3S) are deexcited on ordinary transition and noble-metal surfaces predominantly via the RI+AN mechanism. This is because these surfaces have large work function (usually several electron volts) and provide empty states opposite the 2s level of He*. If the work function of the surface is lowered and the Fermi level rises up above the He* 2s level, the RI process should be suppressed and then the PI process operates. This drastic change in the deexcitation channel is expected to occur with alkali-metal adsorption. On the basis of this prediction, Conrad et al.[227] measured first the He*(2^1S) spectra of clean and alkali metal- (K and Cs) covered Pd(111) surfaces. However, they did not find such a sudden change from RI+AN to PI at a coverage where the average work function just passes through the energy of the He* 2s level. Instead, they observed that incoming He* atoms did not feel the average work function (Φ_{av}) but the local one (Φ_{loc}) near the point of impact; He* atoms were deexcited on bare Pd patch (where Φ_{loc} is high) via RI+AN and in the vicinity of the adsorbed alkali-metal atom (where Φ_{loc} is low) via PI.

The local modification of the work function of metal surfaces induced by alkali-metal adsorption has been confirmed unambiguously by subsequent experiments.[29,42,97,176,197,206,228,229] For example, the He*(2^3S) spectra of K/Pt(111) surfaces are shown in Figure 20b.[29] For the clean surface, the He*(2^3S) atoms are deexcited via the RI+AN process and yield a broad spectrum reflecting self-convolution of the local density of states of Pt(111). As can be seen in the figure, even at lowest coverage ($\theta_K = 0.03$), the K 4s-derived band via the PI clearly appears near E_F superposed on the RI+AN contribution. This indicates that K free patches exist on the surface in coexistence with K islands and/or atoms with a local work function or dipole field sufficient to suppress the RI process of the incoming He*(2^3S).

A similar feature has been observed also for alkali-metal atoms adsorbed on semiconductor surfaces.[44,118,119,154,230,231] Nishigaki et al. studied adsorbed Si(100)-2×1 and Si(111)-7×7 surfaces and

Table 4. List of Adsorption Systems Studied by MAES

adsorbate	substrate
Ag	Ru(0001)[205]
Al	W(110)[87]
Ar	Cu(100)[52,a]
Ba	Pt(111)[100,b]
C_{60}	Cu(100);[184,a,b] Si(100);[88] Cs/Si(100);[88] SiO_2[88]
Cl_2	Cu(100);[184,a,b] GaAs(100)[158]
CO	Ag(110);[134] Cu(110);[198] Mo(110);[25,199] Ni(110);[125,a;126] Ni(111);[27,74,195,196,197] K/Ni(111);[197,202,203,204] O/Ni(111);[196] Pd(110);[38,127,a;198] Pd(111);[24,198] Ru(0001);[200] Ag/Ru(0001);[205] Cu/Ru(0001);[200] Li/Ag/Ru(0001);[205] K/Ru(0001);[206,207] W(110);[201] K/W(110)[201]
CO_2	Cu(100)[148,b;184,a,b]
Cs	Cu(100);[149,a] Cu(110);[98,99,b] Pd(111);[227] Ru(0001);[102] Si(100);[118,154] C_{60}/Si(100);[88] Si(111);[154,231] W(110);[42,176,178,179] CsI/W(110);[178] H/W(110);[42] I/W(110);[179] O/W(110)[235]
CsI	W(110)[178,179,233]
Cu	Ru(0001);[132] CO/Ru(0001)[243]
Fe	Ag(100)[133,147c,a]
H_2(or H)	GaAs(110);[159,c] Pd(111);[67;130,c] Ru(0001);[225] W(110);[42] W(poly)[67;130,c]
HCl	GaAs(100)[245]
H_2O	Ag(110);[255] Cu(100);[184,a,b] Cu(poly)[183,b]
I	W(110);[179] Cs/W(110)[179]
K	Cu(100);[127,a] Cu(110);[99,b;229] Ni(111);[97,228] Ru(0001);[206] CO/Ru((0001);[206] H/Ru(0001);[225] O/Ru(0001);[244] Pt(111);[29;100,b] Si(100);[44,118,119,154] Ta(poly);[44] W(110);[176] O/W(110)[201,235]
Li	Cu(110);[99,b] Ru(0001);[102] Ag/Ru(0001);[205] W(110);[176] O/W(110)[236]
LiF	W(110)[86]
Na	Cu(110);[99,b] Pt(111);[100,b] Ru(0001);[102] W(110);[176] O/W(110)[236]
NaCl	W(110)[176,177,233]
NCCN	Pd(100);[131] K/Pd(100);[249] Na/Pd(100)[249]
NH_3	Cu(poly);[183,b] Ni(110);[242] O/Ni(110);[242] Ni(111);[240] CO/Ni(111);[241] Pd(111)[198]
NO	Ag(111);[222,d] Cu(100);[135,a,b] Cu(110);[221] Ni(111);[74,195,196,220] O/Ni(111);[196,220] Pd(111);[221] Pt(111);[221] Ru(0001);[222] Ag/Ru(0001)[222,d]
N_2O	Pt(111);[40] O/Ru(0001)[222]
O_2	Ag(110);[254,c] Al(111);[237] Cu(100);[127,a;184,a,b] Cs/Cu(100);[149,a] Cu(110);[67;130,c] Cs/Cu(110);[247,248] Fe(110);[123,a] Mo(110);[25] Ni(100);[124,238] Ni(111);[239] Pd(111);[67,130,c] Ru(0001);[244] Cs/Ru(0001);[250,252,253] K/Ru(0001);[244] Li/Ru(0001);[232] Na/Ru(0001);[251] Si(100);[149,a,e;156] Cs/Si(100);[246] K/Si(100);[44,246] Si(111);[41,e;144] K/Ta(poly);[44] W(110);[201,147d] W(poly);[67;130,c] Al/W(110);[87,237] Cs/W(110);[234,235] CO/W(110);[147b,a;147d] Fe/W(110);[147a,a;147b,a] K/W(110);[176,235] Li/W(110);[236] Na/W(110)[236]
PF_3	Cu(110);[198] Pd(111)[198]
Rb	Cu(110);[99,b] Pt(111)[100]
Sb	GaAs(110)[159]
Te	Ni(100)[40]
Xe	Au(100);[135,a] Cu(100);[51,a;52,a] graphite[180,b] Ni(111);[228] K/Ni(111)[228]
Yb	GaAs(110)[150]

[a] Involves spin-resolved measurement. [b] Only condensed phase. [c] Involves deconvoluted spectrum. [d] N_2O formation. [e] Only oxide.

pointed out that a part of He* atoms are deexcited via PI even at lowest coverage to yield alkali-metal s-derived bands in the spectra.[154,230,231] It is interesting that alkali-metals on the Si(100)-2×1 surface form an ordered structure at monolayer coverage. From the comparison of the He* spectra of K and Cs adsorbed Si(100), Masuda et al. suggested that at one monolayer the former system remains semiconducting in nature while the latter system becomes a metallic phase.[118,119] In fact, on the K monolayer, the singlet−triplet conversion scarcely takes place owing to the low density of occupied and unoccupied states around E_F, in contrast to the case of the Cs monolayer.

5. Other Atoms and Molecules

The MAES technique has been applied to other adsorbed systems, which include dissociative and molecular adsorbed surfaces. Table 4 lists the systems studied so far. For the dissociatively adsorbed molecules (such as chalcogens) on transition-metal surfaces, metastable atoms are deexcited via the RI+AN process and the deconvolution methods should be used to obtain the one-electron states of the surface. The adsorption of organic and organometallic molecules has been also extensively studied by use of MAES and will be discussed in section V.

C. Surface Reactions

1. Reactions on Alkali-Adsorbed Surfaces

As stated in section VI.B.4, the adsorption of alkali-metal atoms induces the local modification of the work function. In order to examine this effect on the adsorption of foreign atoms and molecules, Lee et al. measured the He*(2^1S) spectra of Xe adsorbed on K-preadsorbed Ni(111) at various K coverages,[228] which are shown in Figure 53. The spectrum of Xe on the clean Ni(111) surface shows a typical Xe doublet structure due to the $5P_{1/2}$ and $5P_{3/2}$ states. Upon K preadsorption of $\theta_K = 0.01$, the doublet structure shifts slightly to lower kinetic energies (higher binding energies) and a third peak newly appears. The third peak is located at higher binding energy region and corresponds to one of the doublet of Xe adsorbed at strongly modified, local work function sites. With increasing K coverage, the original doublet decreases in intensity and instead the second doublet increases. Above the coverage of $\theta_K = 0.06$ the He* spectrum shows only the second doublet structure. These findings indicate clearly

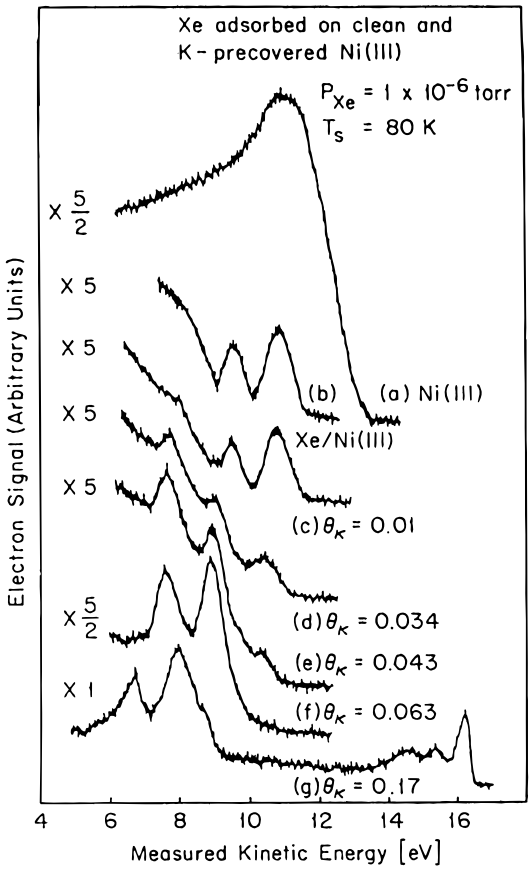

Figure 53. Metastable atom electron spectra of (a) a clean Ni(111), (b) Xe adsorbed on Ni(111), and c−g Xe adsorbed on K-precovered Ni(111) at various K coverages. In the spectra b−g Xe adsorption was made at 80 K and at ambient pressure of 1 × 10^{-6} Torr. (Reprinted with permission from ref 228. Copyright 1985 Elsevier.)

that at very low coverage the K/Ni(111) surface has two kinds of sites with different work functions. The Santa Barbara group has investigated extensively the interactions of CO with alkali metal-adsorbed surfaces, namely, two different sites reflecting the local work function,[197] the enhancement of backdonation form Ni(111) to CO $2\pi^*$,[202] atomic exchange between CO molecules near the K adatom,[203] the change in molecular orientation upon heating,[204] the Li-promoted adsorption on Ag layers on Ru(0001),[205] and the splitting of the CO 1π-derived orbital.[207]

The interactions of an alkali metal-adsorbed surface with oxygen have been also a subject for the MAES study in relation to the oxide formation depending on the oxygen exposure[244,248] and the quantum size effect of the conduction electrons.[247,248] Further, it is known that electrons (exoelectrons) are emitted from the surface in a limited stage of oxidation, when an alkali-metal surface is exposed to oxygen gas.[232,234,250−253] A model proposed by Nørskov et al. is schematically shown in Figure 54.[256] The affinity level (E_A) of free O_2 is located at 0.4 eV below the vacuum level. When O_2 molecule approaches a metallic surface, E_A will be lowered in energy first by image potential effect and then by chemical interaction. If this level is lowered further below the Fermi level and survives resonance transfer from a metal electron, the resulting hole state ϵ_A of O_2 may be filled by a valence electron from the metal whereby the energy released causes Auger emission of another

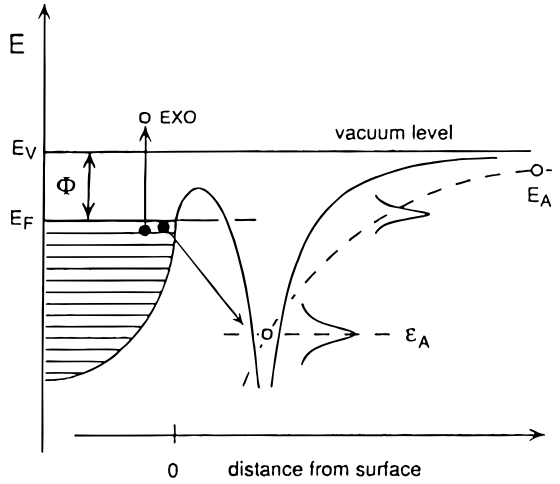

Figure 54. Schematic energy diagram for the mechanism of exoelectron emission proposed by Nørskof et al. (Reprinted with permission from ref 251. Copyright 1993 Elsevier.)

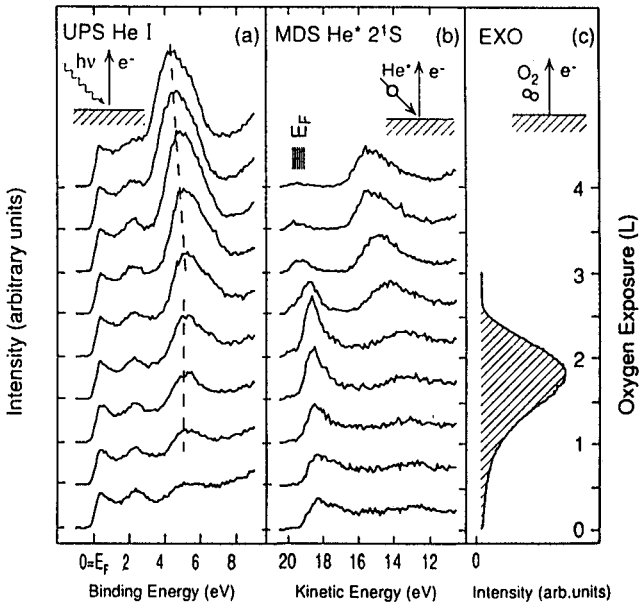

Figure 55. (a) He I photoemission spectra of the oxidation of about 2 monolayer of Li on Ru(001), (b) the complementary He*(2^1S) spectra, and (c) exoelectron emission yield as a function of oxygen exposure. (Reprinted with permission from ref 232. Copyright 1994 The American Physical Society.)

metal electron into the vacuum. Using this simple model, Böttcher et al. interpreted the exoelectron emission process during the oxidation of Cs films;[250,252,253] the exoelectron emission is confined to the stage of $Cs_2O_2 \rightarrow Cs_2O$ where the surface density of states near E_F is sufficiently low to suppress the resonance ionization of the hole state ϵ_A of O_2.

To characterize the exoelectron emission process in Li films, Greber et al. measured the He I and He*(2^1S) spectra of the Li-precovered Ru(0001) surfaces as a function of oxygen exposure, together with the emission yield of exoelectrons, negative ions, and photons.[232] Figure 55 shows their results and the features are summarized as follows:

(i) The yield of exoelectrons (panel c) and O^- ions becomes the maximum at ∼1.8 L exposure, where the work function of the surface reaches the minimum.

The light emission is not found within the detection limit.

(ii) In the He I spectra (panel a), two peaks at $E_B \approx 2.4$ and 4.9 eV are assigned to the Ru 4d-derived states. Upon exposure of oxygen, a peak at $E_B \approx 5.2$ eV appears, which is due to the O 2p-derived states of Li_2O. For exposure above ~2 L where the exoelectron emission scarcely occurs, the O 2p-derived states shift to the lower E_B side (which may correspond to the formation of higher oxides). The Fermi edge is observed in the whole range of exposure.

(iii) The He* spectra (panel b) are much different from the He I spectra. For exposure below ~2 L, they show only a pronounced structure near E_F and no O 2p-derived band. This indicates that the exoelectron emission takes place on the Li-precovered Ru(001) when the gas−solid interface is metallic in nature and oxygen is incorporated beneath the top Li layer, in contrast to the case for the Cs overlayers mentioned above. Above ~2 L, the intensity of the structure near E_F drops rapidly parallel to the appearance of the O 2p-derived states. This means that oxygen is no longer incorporated below the surface in this stage but also present in the outermost layer. On the basis of these data and a cluster calculation using the local-spin-density approximation, Greber et al. suggested that the exoelectron emission at the Li overlayers proceeds in a subsequent way; the formation of a transient O_2^{2-} species by electron transfer from the metal to the impinging O_2 molecule, the dissociation of the O_2^{2-} ion into two O^- fragments, one of which is ejected to the vacuum and the other forms a hole state at the metal surface to cause the Auger emission.[232]

2. Other Reactions

MAES is suited also to study the surface reacton accompanying the layer growth, because it provides selective information on the frontier region of the outermost surface, where the reaction proceeds. Ishii et al. first applied MAES to the observation of the oxide layer formation on Si(111)-7×7 and found that He*(2^3S) metastables are deexcited on the clean surface via RI+AN (see Figure 30) and on the oxidized surface via PI (see Figure 10),[41] reflecting the semiconductor−insulator phase transition at the outermost surface layer. Kempter et al. have studied in detail the growth of insulating layers such as alkali halides (LiF,[86] NaCl,[176,177] and CsI[178,179]) and aluminum oxide[87,237] on W(110). Figure 56 shows the He*(2^3S) and He I spectra during the simultaneous exposure of Al and O_2 onto a W(110) surface held at 750 K.[87] The bottom spectra in the figure are for the clean substrate; sharp bands near E_F in the UPS are assigned to emissions from the W 5d states, while a broad structure in the MAES is based on a self-convolution of the surface density of states due to RI+AN. Upon coadsorption of Al and oxygen, the UPS show the broad O 2p-derived bands between E_B = 6.5 and 7.5 eV depending on the exposure time. The corresponding bands also appear in the MAES, showing that the deexcitation channel of the He*(2^3S) metastables is converted to the PI process. It is noted that the MAES of the coadsorbed surfaces show very little emission in the higher E_k region

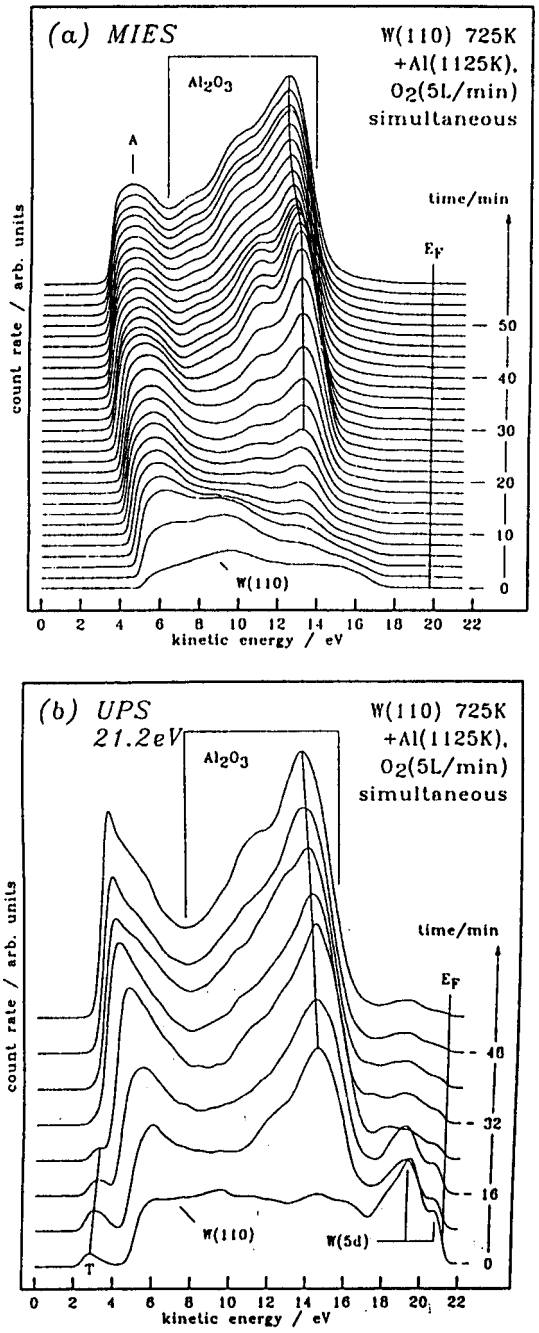

Figure 56. Metastable atom electron spectra during the coadsorption of Al (evaporation temperature, 1150 K) and oxygen (5 L/min) onto W(110) held at 750 K. (Reprinted with permission from ref 87. Copyright 1994 Elsevier.)

(between E_F and about 15 eV), although the substrate 5d bands are clearly seen in the UPS. From a comparison with the photoemission spectrum of bulk alumina, it is concluded that the coadsorption of Al and oxygen on hot W(110) leads directly to the formation of Al oxide layers. Kempter et al. also measured the UPS and MAES during the exposure of Al(2.5 adlayers)/W(110) to oxygen at room temperature and indicated that these surfaces require an additional heat treatment to become transformed into alumina.

The Santa Barbara group applied MAES as well as TPD, AES, and HREELS to study the atomic layer etching reactions of Cl_2[158] and HCl[245] on GaAs(100) surfaces. Their data indicate that the chlorination of the Ga-rich c(8×2)Ga surface at 85 K by Cl_2 forms

Table 5. Organic Solid Films Studied by PIES (MAES)

molecule[a]	substrate	preparation method[b]	ref	remark
acetylene	Pd(111)	vac. depo.	30, 198	
acetylene	Pd(111)	vac. depo.	30	trimerization to benzene
ethylene	Ni(111)	vac. depo.	196	
benzene	Pd(111)	vac. depo.	30, 198	
benzene	Cu	vac. depo.	259	
benzene	graphite	vac. depo.	266, 276	
biphenyl	Cu	vac. depo. (sub.)	258	
anthracene	Cu	vac. depo. (sub.)	26	
naphthacene	Cu	vac. depo. (sub.)	23, 257	
naphthacene	stainless steel	vac. depo. (sub.)	260	
naphthacene	stainless steel	vac. depo. (sub.)	260	photooxidation
pentacene	graphite	vac. depo. (sub.)	264,[c] 291[c]	
pentacene	stainless steel	vac. depo. (sub.)	291[c]	
perylene	Cu	vac. depo. (sub.)	257	
coronene	Cu	vac. depo. (sub.)	257	
rubrene	stainless steel	vac. depo. (sub.)	260	
rubrene	stainless steel	vac. depo. (sub.)	260	photooxidation
acrylonitrile	Ni	vac. depo.	268	
acrylonitrile	Ni	electrochemical adsorption	268	
pyridine	Ag	vac. depo.	267	
MgPc	graphite	vac. depo. (sub.)	278[c]	
FePc	graphite	vac. depo. (sub.)	265,[c] 273,[c] 278,[c] 292[c]	
FePc	stainless steel	vac. depo. (sub.)	273,[c] 278[c]	
ClAlPc	graphite	vac. depo. (sub.)	288[c]	
ClAlPc	graphite	vac. depo. (sub.)	283[c]	observed by emission microscope
ClAlPc	MoS_2(0001)	vac. depo. (sub.)	287,[c] 290[c]	
TFTCNQ	graphite	vac. depo. (sub.)	280,[c] 281[c]	
TFTCNQ	graphite	vac. depo. (sub.)	280,[c] 281[c]	CT complex with graphite
TFTCNQ	TMTSF/graphite	vac. depo. (sub.)	280[c]	CT complex with TMTSF
TMTSF	graphite	vac. depo. (sub.)	280[c]	
TMTSF	TFTCNQ/graphite	vac. depo. (sub.)	280[c]	CT complex with TFTCNQ
octane	Pt(111)	vac. depo.	284	
hexacosane	graphite	vac. depo. (sub.)	279[c]	
hexatriacontane	graphite	vac. depo. (sub.)	279[c]	
hexatriacontane	Cu	vac. depo. (sub.)	279[c]	
tetratetracontane	graphite	vac. depo. (sub.)	279[c]	
tetratetracontane	Cu	vac. depo. (sub.)	279[c]	
HTDY	graphite	vac. depo. (sub.)	282,[c] 285,[c] 289[c]	
HTDY	graphite	vac. depo. (sub.)	282,[c] 285,[c] 289[c]	polymerization to *atomic sash*
DTTY	graphite	vac. depo. (sub.)	286,[c] 289[c]	
DTTY	graphite	vac. depo. (sub.)	286,[c] 289[c]	polymerization to *atomic cloth*
$ZnSt_2$	graphite	vac. depo. (sub.)	282[c]	
$ZnSt_2$	stainless steel	vac. depo. (sub.)	282[c]	
$CdSt_2$	SiO_2	LB	277	
PA+PHA (2:1)	stainless steel	LB	270, 274	
AA	stainless steel	LB	270, 274	
AA+PDA (2:1)	stainless steel	LB	270	
PFDA	SiO_2	vac. depo. (sub.)	275	
HDT	Au(111)	self assembling	284	
HDT	Pt(111)	self assembling	284	
polyacetylene			269	
K-doped polyacetylene			269	
polyacrylonitrile	Fe	electrochemical polymerization	261−263	
polyacrylonitrile	Fe	electrochemical polymerization	261−263	reticulation
polyacrylonitrile	Ni	electrochemical polymerization	272	

[a] The structural formulae of the molecules are shown in Figure 57. [b] The abbreviations vac. depo. and vac. depo. (sub.) indicate the film preparation by vapor deposition from gas or liquid and that by vapor deposition from solid (sublimation), respectively. [c] The deposited amount was controlled in the unit of monolayer (equivalence).

a GaCl layer where each surface Ga atom has one Cl bond and two back-bonds to As, and that the GaCl species convert gradually to $GaCl_2$ by repeating treatment of Cl_2 adsorption at 85 K and warming to 130 K.

V. Organic Surfaces

A. Overview

Organic solids studied by PIES are tabulated in Table 5, and the formulae of the compounds are shown in Figure 57. The PIES of an organic solid were first obtained by Shibata et al. for a polycrystalline film of naphthacene in 1975.[23] As in the cases of UPS vapor-deposited "thin" films (200−500 Å in thickness) were used to avoid sample charging. It was shown that the kinetic energies of electrons giving the features in the spectra could be estimated from the energy of the metastable atom minus *IP*s obtained by UPS. This was the first observation of PI for known valence bands. Then, the PIES of naphthacene, perylene, and coronene films were

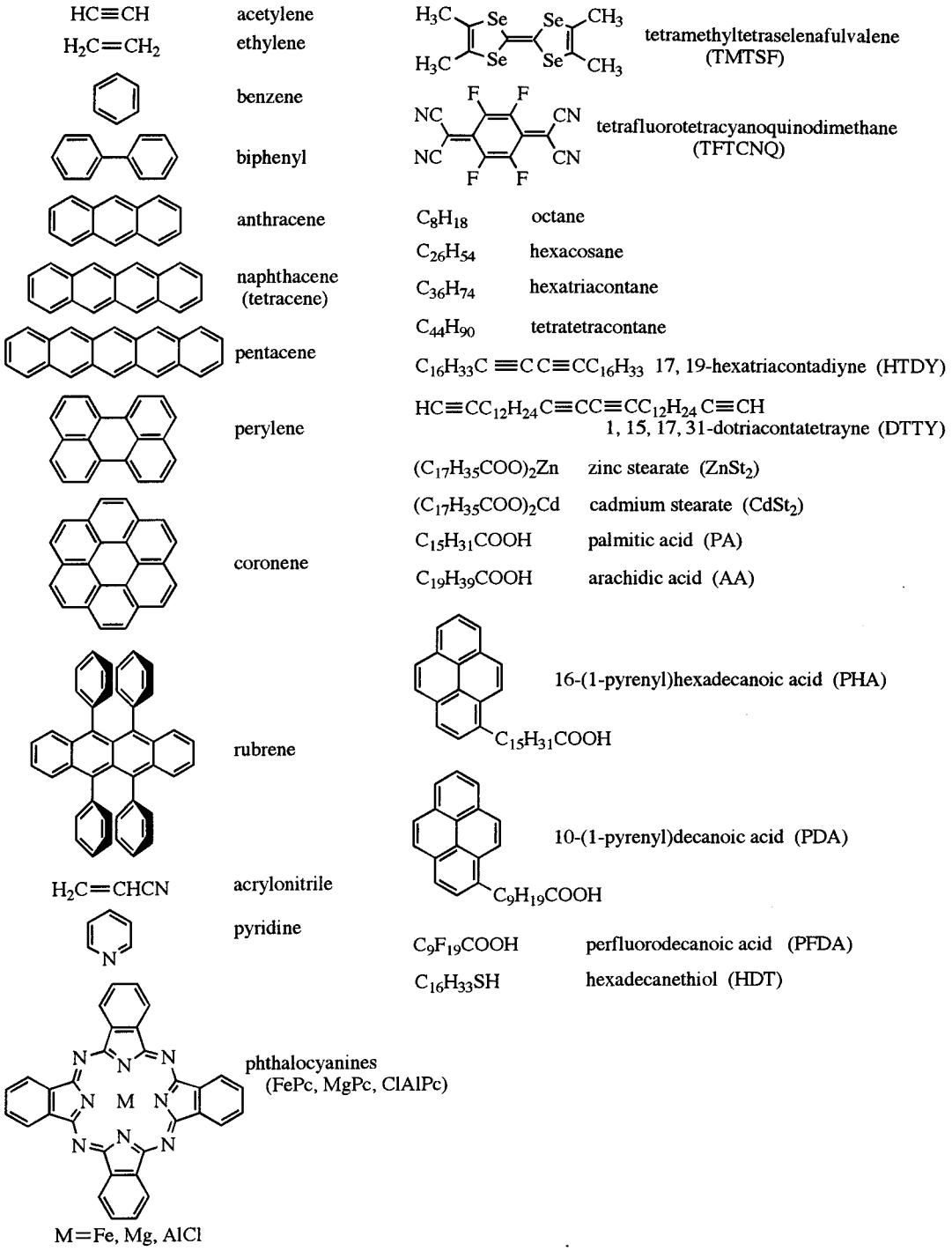

Figure 57. Formulae of the molecules constituting the organic solid films studied by PIES.

measured with He*, Ne*, and Ar* metastables.[257] Since these early studies, the deexcitation of metastables through the PI process has been observed for almost all the organic films given in Table 5.[23,26,30,196,198,257−292]

Since only molecules in the outermost surface layer can be selectively attacked by metastables at the exposed portion of the molecular surface, the "local" distribution of individual MO's at a definite part of a molecule is reflected in the PIES, provided that each surface molecule has the same orientation with respect to the metastable beam (see section III.B.1). In 1980, Munakata et al. confirmed this idea by comparing the PIES of an evaporated film composed of anthracene crystallites oriented with their *ab* planes parallel to the substrate and that of anthracene vapor.[26] This finding made one of the most important steps in the current line of PIES investigations of organic solids, and studies on molecular aggregation by PIES was started.[258] From this time on, the PIES measured by the Japanese groups[264−267,270,273−283,285−290] and those by other authors[268,272,284] have been analyzed essentially on the basis of this interpretation.

It is natural that aromatic monolayers whose thickness is only 3.4 Å (= twice the van der Waals (VDW) radius of the C atom in aromatics) were taken up to make the most use of the extreme surface sensitivity of PIES.[264,265] Harada et al. piled up monolayers defined by PIES and observed the first

stage of the film growth layer by layer, using UPS in combination with PIES.[264] Besides the studies on the aggregation of molecules with known electronic structures, Ozaki et al. suggested that the distribution of each MO can be probed from various directions and the whole shape of the MO will be obtained if various parts of ordered molecules are exposed to metastable beams.[273] They also demonstrated that the complicated electronic structure of a large organic molecule can be disclosed by comparing the PIES of orientation-controlled films.[278] In addition, Ohno et al. used PIES to detect the change in the electronic structure due to surface reactions in organic solids.[260] The application of PIES on the stream described in this paragraph has been extended to many kinds of films, as will be described in the following sections.

Several studies concerning organic surfaces do not belong to the above stream. Reynaud et al.[261−263] and Lee et al.[269] applied PIES to polymer films: the former investigated polyacrylonitrile (PAN) while the latter studied polyacetylene and K-doped polyacetylene. In both cases metastables were found to be deexcited via PI. Sesselmann et al.[30,198] and Bozso et al.[196] made the extension of their work on inorganic surfaces described in section IV to simple organic molecules such as acetylene, ethylene, and benzene adsorbed on well defined metal surfaces. For these systems the RI+AN process was observed at low coverage. Organic liquid surfaces were exclusively investigated by a group led by Morgner.[45,46,293−299]

Since the PIES applied to adsorbed surfaces of small organic molecules is similar to that applied to inorganic surfaces, we concentrate our attention mainly on the evaporated "films" of larger molecules. In section V.C, the PIES of various films will be exemplified and their interpretation from the chemical point of view, on the basis of the MO picture, will be the central topic.

B. Experimental Aspects

1. Preparation of Organic Films

a. Sample Preparation Methods. In the investigation of organic surfaces, compounds having large molecular weights, existing in solid phase at room temperature and atmospheric pressure (standard temperature and pressure, STP), have been mainly chosen. In this case the amount of deposition by sample sublimation can be regulated precisely with a quartz oscillator monitor calibrated in advance. This allowed us to control the film thickness in the unit of monolayer[264,265,273,278−283,285−290] and to observe the film growth layer-by-layer.[264,280,282,287,288,290] In the case of a compound existing in gas or liquid phase at STP, the sample exposure is expressed in Langmuir unit L (1 L = 10^{-6} Torr s), but the control of the deposited amount is not so easy compared to the first case. In Table 5 the films prepared by vapor deposition from solid (sublimation) and those by vapor deposition from gas or liquid are indicated by "vap. depo. (sub.)" and "vap. depo.", respectively. In addition to the above films, films prepared by a "wet" method, e.g., Langmuir−Blodgett (LB) films,[274,277] layers adsorbed at a liquid-solid interface under the influence of electric field,[268] and monolayers due to self assembling,[284] have been investigated. The three types (X, Y, and Z) of LB films[300] and two techniques for LB film preparation, i.e., the conventional LB (= vertical dipping (VD)) method[300] and the horizontal lifting (HL) method[301] are shown in Figure 58, parts a and b, respectively. There are also studies of the films originally formed by the dry or wet method and further converted chemically by photooxidation,[260] photopolymerization,[282,285,286,289] thermal polymerization,[261−263] or charge transfer reactions.[280,281]

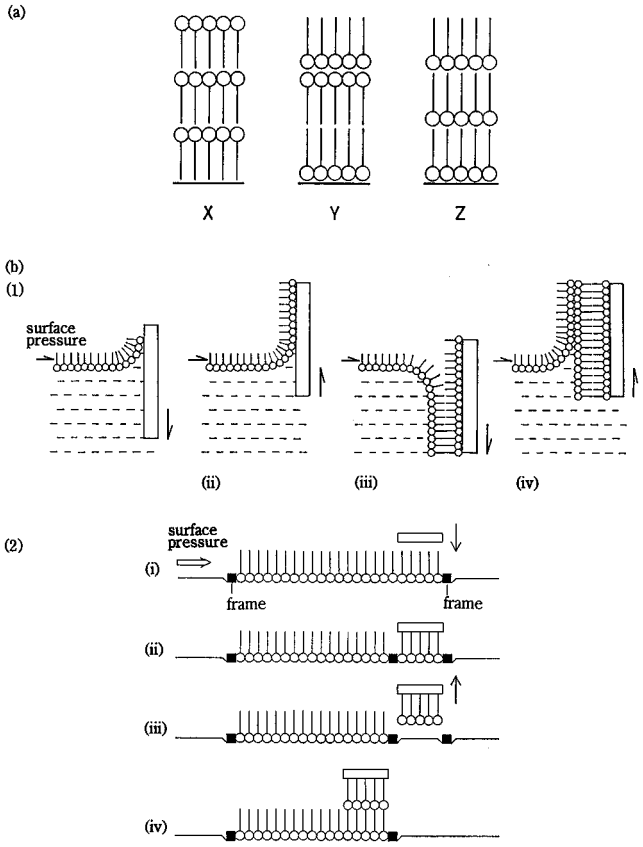

Figure 58. (a) Three types of LB films and (b) two methods for LB film preparation: (1) the conventional Langmuir−Blodgett (LB) (vertical dipping) method and (2) the horizontal lifting (HL) method, in which frames are used to edge or divide the adsorbed surface.

b. Substrates. As can be seen in Table 5, various substrates have been used for sample preparation. In early studies, only Cu and stainless steel substrates without crystallographical surfaces were used for specimens prepared both inside and outside the preparation chamber of the spectrometer.[23,26,257−260] Later, these substrates were mainly utilized in order to form polycrystalline or amorphous films rather than epitaxially grown ones. The metal substrates together with surface oxidized silicon wafers were employed for the preparation of LB films as well. A cleavage plane of graphite (highly oriented pyrolytic graphite (HOPG) or Grafoil) is suitable for the PIES study of evaporated ultrathin films, because the MAES show a sharp peak, whose intensity can be used as an direct measure of the surface coverage.[264,276,288] Grafoil provided by Union Carbide consists of graphite crystallites with their cleavage planes parallel to the foil plane[302] and gives essentially the same PIES as that of HOPG. But both

in a grafoil and a HOPG substrate a problem arises when one wishes to characterize the film also by electron diffraction requiring lateral molecular ordering, since the *ab* plane of graphite crystallites is randomly rotated on the *c* axis. The use of a cleavage plane of an MoS_2 single crystal, however, can solve this problem: chloroaluminum phthalocyanine (Cl-AlPc) monolayers have recently been investigated by PIES, ARUPS, and LEED.[290] There are other PIES studies combined with LEED; an octane layer adsorbed on a Pt(111) substrate and self-assembling monolayers of hexadecanethiol ($C_{16}H_{33}SH$; HDT) on a Au(111) and a Pt(111) surface.[284]

c. Estimation and Confirmation of the Amount of Deposited Sample. The amount of the deposited sample required to form a close-packed monolayer with the molecular or carbon skeleton plane oriented parallel to an atomically flat substrate, monolayer equivalence (MLE), was introduced for planar and chain compounds. One can estimate 1 MLE from the area of the substrate surface occupied by one molecule *S*, which is obtained from LEED experiments on related compounds (or a substitute model based on VDW packing in a monolayer). For example, some short *n*-alkanes $C_4H_{10}-C_8H_{18}$ form monolayer films in which molecules all in trans conformation pack closely with their skeleton planes parallel to a Pt(111) and a Ag(111) surface.[303,304] The formula giving the *S* value of the alkane with carbon number *N*, *S*(*N*), is given by

$$S(N) = 6.65(N + 1)\ (\text{Å}^2/\text{molecule}) \qquad (35)$$

On the assumption that the equation holds for larger *N* on graphite, 1 MLE of longer alkenes was estimated.[279]

Experimentally, the deposited amount δ of an evaporated film is monitored by a quartz oscillator with a known correction factor for its geometrical arrangement relative to the substrate, under the condition that the sticking coefficient of the sample to both the substrate and oscillator is regarded unity. If we observe that the PIES features characteristic of the molecule gradually become intense with increasing δ while those due to the substrate become almost missing at $\delta = 1$ MLE, we conclude that the molecules must lie flat on the substrate so as to form a monolayer. This is because metastable atoms interact only with the molecules at the outermost surface layer and 1 MLE of the molecules cannot cover up the substrate surface with tilted orientations. The disappearance of the sharp peak due to the conduction bands of graphite has been always observed in the PIES of various planar and chain compounds at $\delta = 1$.[264,265,278−283,285,286,288,289] Furthermore, the accuracy of δ control and the formation of a "flat-lying" monolayer were also verified from the analysis of the width and integrated intensities of the first bands in the PIES and UPS of a pentacene film grown layer-by-layer (see section V.C.2.c).[264]

Although δ cannot be directly controlled for small molecules adsorbed on the substrate, it is possible to obtain the value of δ indirectly on graphite. Suzuki et al. investigated the changes of PIES and UPS dependent on benzene exposure in L unit and determined δ from the intensities of the graphite conduction band peak in the PIES and UPS.[276]

2. Relaxation Shift

When an electron is emitted from molecular solid upon PI or photoionization, the ionized state is stabilized and gives lower IP because the molecular ion left behind polarizes surrounding molecules. Therefore, a PIES or a UPS band in solid phase generally has higher electron energy E_k compared to the corresponding band in gas phase. Since the extent of the stabilization, the relaxation shift, depends on the molecular packing,[305] the shift of PIES/UPS bands provides indirect information about molecular aggregation.[35,270,291] A PIES peak due to electrons from the outermost layer is located at a lower E_k than the corresponding UPS peak having large contribution of electrons from inner layers as well, because a molecule at the top layer lacks neighboring molecules on it (cf., section V.C.2.c).

3. Features Due to Secondary Electrons

Since the early work, it has been pointed out that the PIES of an aromatic solid exhibits a considerable background as in the case of UPS: a part of Penning electrons formed at the surface is emitted directly to vacuum while those having momenta directed to the inside of the solid undergo electron−electron scattering to produce low-energy secondary electrons.[257,259] An attempt was made to reproduce the observed spectra of multilayered benzene adsorbed on graphite by simulation, in which the origin of the background was ascribed to the inelastic scattering of Penning electrons as well as to the Auger relaxation of the holes created on the surface by PI.[276]

Situation is a little different for crystalline *n*-alkane, which forms a band structure in a single molecule.[306] In the UPS, secondary electrons produced by the inelastic scattering of photoelectrons generated in the solid accumulate in the unoccupied states having high densities to exhibit predominant features.[307] In the PIES, on the contrary, electrons ejected at the outermost surface have less chance to suffer inelastic scattering and, therefore, provide a spectrum with little influence of the unoccupied states.[279]

C. Characterization of Some Organic Films

1. Chain Compounds

a. n-Alkanes.[279] As a basis for investigating molecular aggregation by PIES, it is necessary to obtain some fingerprint spectra due to specific orientations of basic chemical structures frequently appeared in organic films. A typical attempt was made for long *n*-alkanes. After chain-length dependence of the electronic structure was studied by MO calculations as well as by PIES, the local distributions of MO's outside the surface were probed by PIES for two molecular orientations lying and standing on the substrate.

Figure 59a shows the calculated IPs of four *n*-alkanes, decane ($C_{10}H_{22}$), tridecane ($C_{13}H_{28}$), hexadecane ($C_{16}H_{34}$), and nonadecane ($C_{19}H_{40}$), via Koopmans' approximation. For some MO's of $C_{16}H_{34}$ the

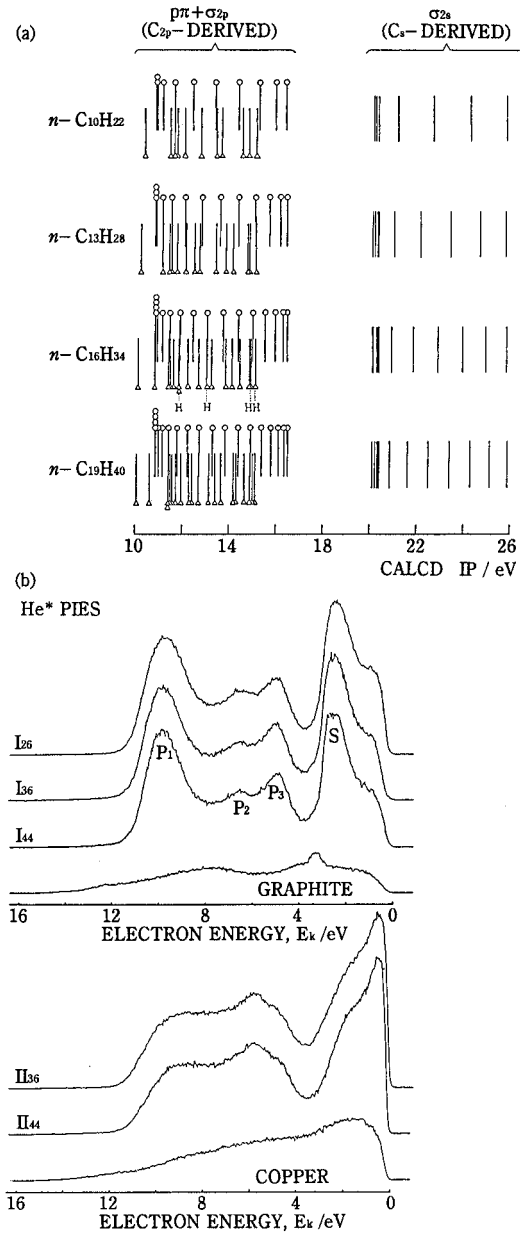

Figure 59. (a) Calculated ionization potentials (*IP*) of *n*-alkanes, decane ($C_{10}H_{22}$), tridecane ($C_{13}H_{28}$), hexadecane ($C_{16}H_{34}$), and nonadecane ($C_{19}H_{40}$). Bars labeled with open circles and triangles correspond to pseudo-π (pπ) and σ_{2p} MO's, respectively, the other bars to σ_{2s} MO's. The bars of σ_{2p} MO's having large distribution on the terminal H atom are indicated by "H" for hexadecane. (b) He*(2^3S) PIES of *n*-alkane evaporated films. Films I_{26}, I_{36}, and I_{44} were prepared by depositing 1 MLE of hexacosane ($C_{26}H_{54}$), hexatriacontane ($C_{36}H_{74}$), and tetratetracontane ($C_{44}H_{90}$) on a graphite substrate at 213 K, respectively. Films II_{36} and II_{44} were formed by depositing 68 MLE of hexatriacontane and 34 MLE of tetratetracontane on a Cu substrate at room temperature, respectively. The spectra of the graphite and Cu substrates are also shown. (Reprinted from ref 279. Copyright 1990 American Chemical Society.)

constituent AO's are drawn on the plane of the carbon skeleton (*xy* plane) in Figure 60. The MO's of *n*-alkane can be classified into three types: pπ, σ_{2p}, and σ_{2s}. The pπ MO's consist of the C $2p_z$ and H 1s AO's, and have pseudo-π character, spreading almost normal to the skeleton plane. The σ_{2p} MO's are made up of the C $2p_x$, $2p_y$, and H 1s AO's while the σ_{2s} MO's are composed of the C 2s and H1s AO's. Each *n*-alkane calculated in Figure 59a has an energy gap between *IP* 16.5 and 20.1 eV; the pπ and σ_{2p} MO's are present above this energy gap and the σ_{2s} MO's below it. In addition, some MO energies tend to gather around IP's of 11 and 20 eV as the alkyl chain becomes longer. It is of note that the high density of states (DOS) around *IP* 11 eV is due to pπ MO's. On the other hand, the high DOS around 20 eV is ascribable to σ_{2s} MO's.

Figure 59b shows the PIES of *n*-alkane evaporated films. The symbols I_{26}, I_{36}, and I_{44} stand for the 1 MLE films of hexacosane ($C_{26}H_{54}$), hexatriacontane ($C_{36}H_{74}$), and tetratetracontane ($C_{44}H_{90}$) prepared on a graphite substrate held at 213 K, whereas II_{36} and II_{44} represent a $C_{36}H_{74}$ (68 MLE) and a $C_{44}H_{90}$ (34 MLE) film prepared on a Cu substrate at room temperature. The Cu substrate was only heated under ultrahigh vacuum, and it did not have a "clean" crystallographical surface. Films I are of monolayer comprising molecules laid flat on the substrate because the graphite features are missing at 1 MLE in the PIES. On the other hand, films II are of crystalline since long *n*-alkanes are well known to form polycrystalline films with the trans zigzag chain oriented perpendicular to the surface upon evaporation onto an "unclean" metal substrate held at room temperature.[307,308] These orientations are consistent with the relative band intensity of the PIES as follows.

Bands P_1 and S markedly enhanced in the PIES of the monolayers I are assigned to the high DOS of pπ and σ_{2s} MO's in Figure 59a, respectively, while the hollow between bands P_3 and S is ascribed to the energy gap. The enhancement of bands P_1 and S is attributable to the flat orientation, because metastable atoms collide with the "sides" (methylene groups) of molecules and interact with pπ and σ_{2s} MO's extending normal to the carbon plane more effectively than with σ_{2p} MO's spreading on the plane. Taking into account the flat molecular orientation and the calculated energies of pπ MO's, bands P_2 and P_3 are also assigned to pπ MO's although the reason why band P_2 is observed in the energy region, where no maximum of the DOS seems to exist, remains uncertain at present.

In the PIES of crystalline films II, features corresponding to bands P_1-P_3 and S of the monolayers are missing, which indicates that pπ and σ_{2s} MO's are scarcely detected. Between E_k 6.5 and 5 eV, where the peaks of pπ bands P_2 and P_3 are located in the monolayer spectra, we can find a peak at E_k 6 eV. According to the calculation, σ_{2p} MO's like 39 and 37 have very large distribution on the terminal H atom (see Figure 60; such σ_{2p} MO's of $C_{16}H_{34}$ are indicated by "H" in Figure 59a). They tend to be concentrated near the bottom of the σ_{2p} MO region, with IP's smaller than that of the lowest pπ MO responsible for band P_3. Thus, the 6 eV peak is related to these MO's and the spectral features of films II are attributed to σ_{2p} MO's distributed on the terminal hydrogen atom, which are exclusively probed by metastables in the standing molecular orientation.

As a consequence, the PIES of films I and II in Figure 59b can be regarded as fingerprints for the lying and standing orientations of alkyl chains, which

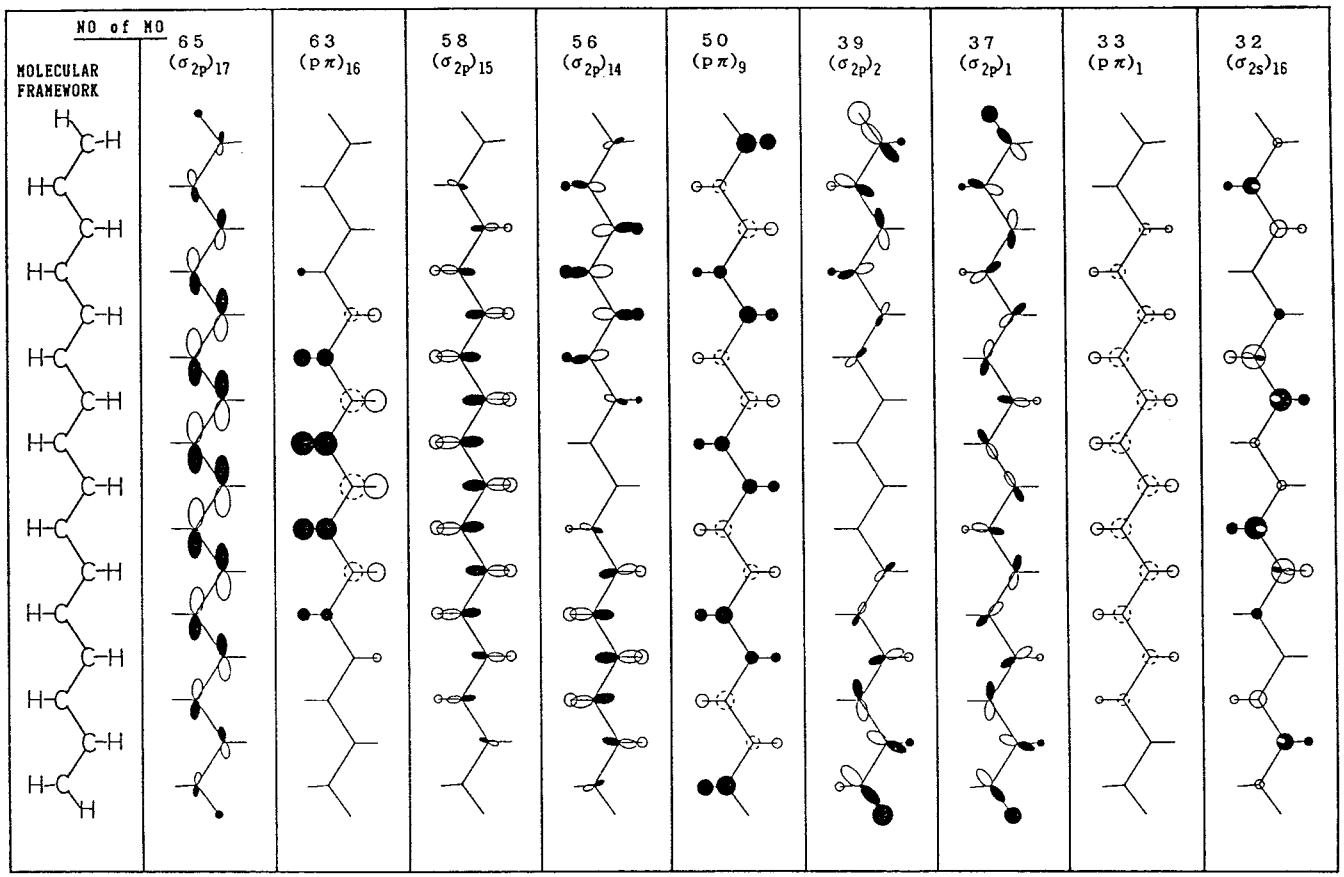

Figure 60. Some MO drawings of hexadecane. The constituent AO's of each MO are projected onto the plane of the carbon skeleton (*xy* plane). The sizes of AO's are proportional to the coefficients of the MO wave functions. The C $2p_x$ and $2p_y$ AO's are shown as their sums. The C $2p_z$ AO's are drawn as broken (or closed) circles, whereas the H 1s and C 2s AO's are drawn as full (or closed) circles. The 65, 63, and 32 MO's are the highest occupied σ_{2p} (also HOMO), $p\pi$, and σ_{2s}, respectively; 58 and 56 are σ_{2p} MO's with little distribution on the terminal H atom, whereas 39 and 37 are those with a large contribution from the terminal H 1s AO. In the first column, the molecular framework of hexadecane is shown. (Reprinted from ref 279. Copyright 1990 American Chemical Society.)

can be used for the identification of the exposed portion of surface molecules having long hydrocarbon units. The lying orientation with the "methylene surface" was found for the evaporated monolayers and piled-up monolayers of fatty acid salts,[282] alkadiyne,[282,285,289] and alkatetrayne[286,289] on graphite while the standing orientation with the "methyl surface" was observed for both evaporated[282] and LB films[270,274,277] of fatty acids and their salts. A *n*-octane layer adsorbed on a Pt(111) surface was also chosen as a representative system for the lying molecular orientation.[284]

b. Long-Chain Fatty Acids and Their Salts. The evaporated films of $ZnSt_2$ were prepared on a graphite substrate held at 193 K (deposited amount, δ = 1−5 MLE) and on a stainless steel substrate at room temperature (12 MLE).[282] The PIES of the 1 MLE film lacks graphite features and exhibits three markedly enhanced bands corresponding to the *n*-alkane bands P_1, P_3, and S in Figure 59b; hence, the film was found to be a monolayer of $ZnSt_2$ molecules laid flat. This film was further employed as a model monolayer of alkadiyne,[282,285] which bears structural similarity to $ZnSt_2$ and undergoes surface topochemical polymerization (see section V.D.6). Since the PIES of thicker films ($\delta \geq 2$ MLE) on graphite also have the three enhanced bands, it was considered that the orientation of the alkyl chains in the outermost layer is similar to that in the monolayer. There seems to be, however, a subtle difference in the molecular aggregation because the relative band intensities for the multilayers are a little different from those for the monolayer. On the other hand, the PIES of the 12 MLE film on a stainless steel substrate is essentially the same as those of the *n*-alkane crystalline films II, indicating that $ZnSt_2$ molecules stand with the methyl ends exposed outside the film surface.

Actually, the fingerprint spectra of the "methyl surface" were first applied to identify the molecular end exposed outside the LB film. Figure 61 shows the PIES of three LB monolayer films. Film I is an arachidic acid (AA; eicosanoic acid) monolayer,[270,274] film II is a mixed monolayer of palmitic acid (PA; hexadecanoic acid) and 16-(1-pyrenyl)hexadecanoic acid (PHA) (33 mol % PHA),[270,274] and film III is a mixed monolayer of AA and 10-(1-pyrenyl)decanoic acid (PDA) (33 mol % PDA).[270] Each monolayer was spread on an aqueous subphase and transferred onto a stainless steel substrate by the conventional LB method. The close resemblance between the PIES of film I and those of the *n*-alkane crystalline films II indicates that AA is oriented with its methyl end toward the outside. In the PIES of film II, three bands are observed in the high E_k region. These bands are assigned to four π MO's of the pyrene ring (two MO's are responsible for the third band). This observation clearly indicates that PHA is oriented

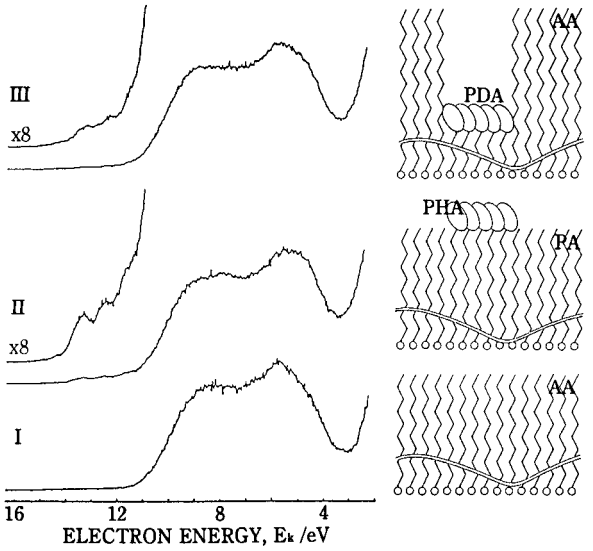

Figure 61. He*(2^3S) PIES of LB films deposited on a stainless steel substrate. Films I, II, and III are a monolayer of arachidic acid (AA), a mixed monolayer of palmitic acid (PA) and 16-(1-pyrenyl)hexadecanoic acid (PHA) (33 mol % PHA), and a mixed monolayer of AA and 10-(1-pyrenyl)decanoic acid (PDA) (33 mol % PDA), respectively. Models of the film structures are shown on the right.

with its pyrene ring (a model for a functional part) exposed to the film surface. It is noteworthy that the PIES of film III also definitely gives the pyrene π bands. Since the alkyl chain of PDA is much shorter than that of AA, the π MO's of the pyrene ring, which is located far from the methyl end of AA in the mixed monolayer, could not interact with metastables if PDA and AA were mixed uniformly. Thus, this observation strongly suggests phase segregation in film III.

The peak position of each π band in curves II and III is shifted to the higher E_k side by ~1.1 eV compared to the position (estimated from UPS) for the gas-phase PIES of pyrene. This shift is mainly due to the relaxation shift for the pyrene ring, because its π electronic structure is considered to be little perturbed by the presence of a hydrocarbon chain bonded to the ring. The shift of 1.1 eV is comparable to the relaxation shift observed in the UPS of the crystalline films of aromatic hydrocarbons, 1.0−1.3 eV,[305] which means that the pyrene rings of PHA (film II) and PDA (film III) must be packed as densely as in crystalline pyrene. It was, therefore, concluded that PHA and PDA molecules are not uniformly dispersed in the PA or AA matrix but, rather, are assembled together to form island structures, causing pyrene rings to overlap effectively.

In order to investigate the basic structure (X, Y, or Z) of LB multilayer films (Figure 58a), the change in PIES dependent on the number of layers was observed.[277] Figure 62a shows the PIES of 1−4 layers of cadmium stearate ($CdSt_2$) on a surface oxidized Si wafer substrate. The first monolayer was transferred onto the hydrophilic surface by the LB method, while the subsequent 2−4 layers were deposited by the HL method, in which the transfer ratio [(the area of the film removed from the water surface)/(the area of the substrate surface)] was kept unity with Teflon frames (cf., Figure 58b(2)). In the

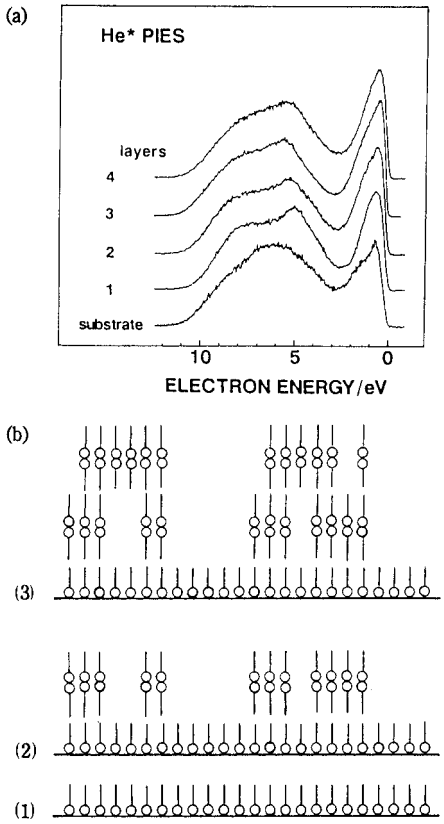

Figure 62. (a) He*(2^3S) PIES of 1−4 layers of cadmium stearate ($CdSt_2$) together with that of a silicon substrate and (b) molecular arrangements in the $CdSt_2$ films: (1) 1 layer film; (2) 2 layer film; (3) 3 layer film. (Reprinted with permission from ref 277. Copyright 1989 Elsevier.)

latter case, an X-type structure with the polar groups exposed outside would be obtained if the monolayer spread on the water surface were transferred to the substrate without the change in molecular orientation and packing. However, all the PIES in Figure 62a are similar to the PIES of the *n*-alkane crystalline films II, indicating that the stearate ions are oriented with the methyl ends exposed outside irrespective of the number of layers (note that the orientation in the 1 layer film by the LB method is reasonable). For the 2−4 layers the imperfect Y-type structures shown in Figure 62b were supported because (1) the transfer ratio was found to be 2 when the Teflon frames were not used in the HL method, and (2) X-ray diffraction patterns of a thicker (21 layers) film by the HL method both with and without the frame gave a long spacing of 50.3 Å corresponding to the Y-type structure.[309] The imperfect Y-type structures are consistent with the fact that the PIES for the 2−4 layers is more diffuse than that for the one layer since some disordering of alkyl chains is expected for the 2−4 layers. The spectral change during thermal annealing also substantiate these structures.[277]

c. Alkanethiol.[284] Using a well-characterized self-assembled monolayer (SAM) of HDT on Au(111) (film I) as a reference system, Brückner et al. studied the structure of a SAM of HDT on Pt(111) (film II). Though film I showed a $(\sqrt{3}\times\sqrt{3})$R30° superstructure in LEED, film II did not exhibit a LEED pattern, which indicates that the HDT molecules do not have long range order on the Pt(111) substrate. However,

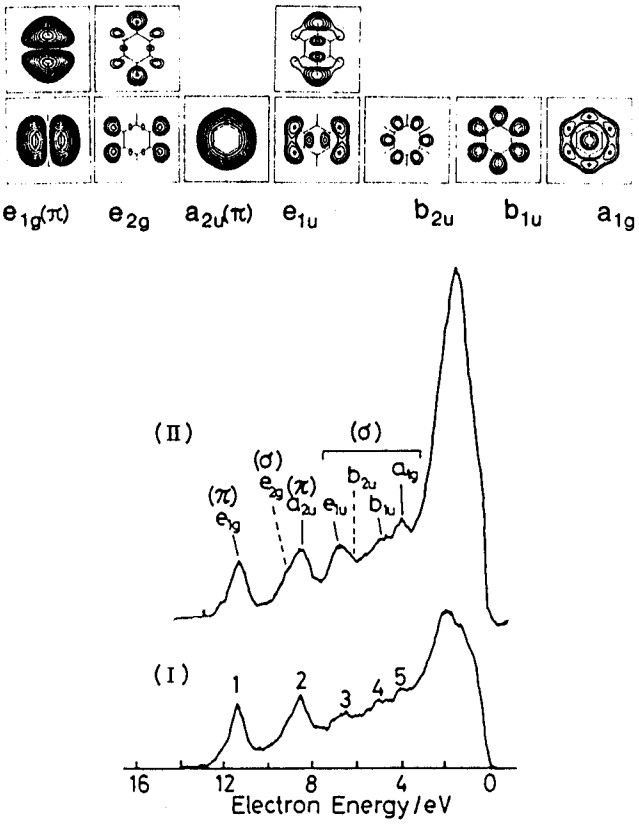

Figure 63. He*(2^3S) PIES of benzene adsorbed on a graphite substrate held at 130 K: (I) 5 L exposure and (II) 200 L exposure. On the top, the electron density maps of benzene MO's are drawn in a plane 1.7 Å above the molecular plane. (Reprinted with permission from ref 266. Copyright 1984 Elsevier.)

film II, as well as film I, was considered to be composed of molecules with the methyl ends exposed outside, because the PIES of both films I and II were similar to those of the *n*-alkane crystalline films II in Figure 59.

d. Perfluorocarboxylic Acid.[275] Mitsuya et al. studied molecular aggregation in a perfluorodecanoic acid (PFDA) evaporated monolayer on a dehydrated SiO_2 substrate through cyclic thermal treatment. The film was ascertained to cover the substrate up to 330 K. Reversible spectral change due to the thermal fluctuation of fluorocarbon tails was observed between 350 and 370 K, while irreversible disordering of the PFDA molecules occurred above 420 K (fairly higher than the bulk melting point 90 °C). The stability of the fluorocarbon chain up to 330 K was ascribed to the rigidity of the chain due to the large VDW radius of the F atoms (compared to the H atoms in a hydrocarbon chain), while extraordinary high second disordering point (compared to the case of an $CdAr_2$ LB monolayer) was attributed to the strong bond formed between the carboxylic group and the substrate.

2. Benzene and Related Compounds

a. Benzene. Figure 63 shows the PIES of 5 L (I) and 200 L (II) of benzene adsorbed on graphite held at 130 K[266] together with the electron density maps of benzene.[62] Film I was estimated to be a few layers from the graphite conduction band peak in the corresponding UPS. In film I, the π bands are much more enhanced than the σ bands, indicating that molecules are oriented parallel to the substrate so that metastables interact with π MO's more effectively than with σ MO's. The intensities of the σ bands relative to the π bands is larger for film II, which means that molecules at the outermost layer are tilted at higher exposure. Although this PIES was related to the molecular orientation of bulk crystal in a previous review,[32] we feel now that the degree of tilt is not large and that it is ascribable to increased disorder in the flat molecular arrangement as in the case of pentacene.[35,291] We here stress the point that the relative intensities also differ among σ bands. In film II, the e_{2g} and b_{2u} bands appear very weak, whereas the e_{1u}, b_{1u}, and a_{1g} bands have appreciable intensities. These differences can be interpreted in terms of the bonding characters of the MO's shown in the maps. Since the e_{1u}, b_{1u}, and a_{1g} MO's are strongly C−H bonding, the significant contribution of H 1s AO makes these MO's favorable to be probed by metastables. On the other hand, the e_{2g} MO having a weakly C−H bonding character and the b_{2u} MO with a localized C−C bonding character cannot interact effectively with metastables.

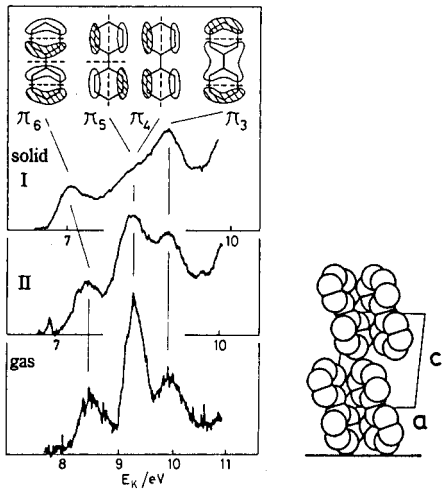

Figure 64. Ne*($^3P_2$) PIES of biphenyl films and vapor. Curves I and II were obtained from a sample deposited on a Cu substrate at 170 K and 109 K, respectively. A schematic diagram of the unit cell of a biphenyl crystal is given on the right. (Reprinted with permission from ref 258. Copyright 1980 Elsevier.)

b. Biphenyl. Figure 64 shows the PIES of biphenyl films (~100 Å thick) evaporated onto a Cu substrate held at 170 K (film I) and 109 K (film II) together with a gas-phase PIES.[258] The PIES of film II changed to that of film I when film II was annealed at 170 K for 40 min, but the PIES remained unchanged upon cooling the film back to 109 K. The UPS of both films were found to be essentially the same. The observed change in the PIES can be interpreted in terms of transition from an amorphous to a polycrystalline state, which is supported by the relative intensities of the spectra. The nearly degenerate π_5 and π_4 MO's have nodal planes along the long axis of the molecule. Therefore, if molecules are oriented at the crystalline surface as shown on the right of Figure 64, the electron distribution of the π_5 and π_4 MO's should be smaller at the surface, and hence their band intensities should be weaker than those of the π_6 and π_3 MO's, as in the PIES of film I.

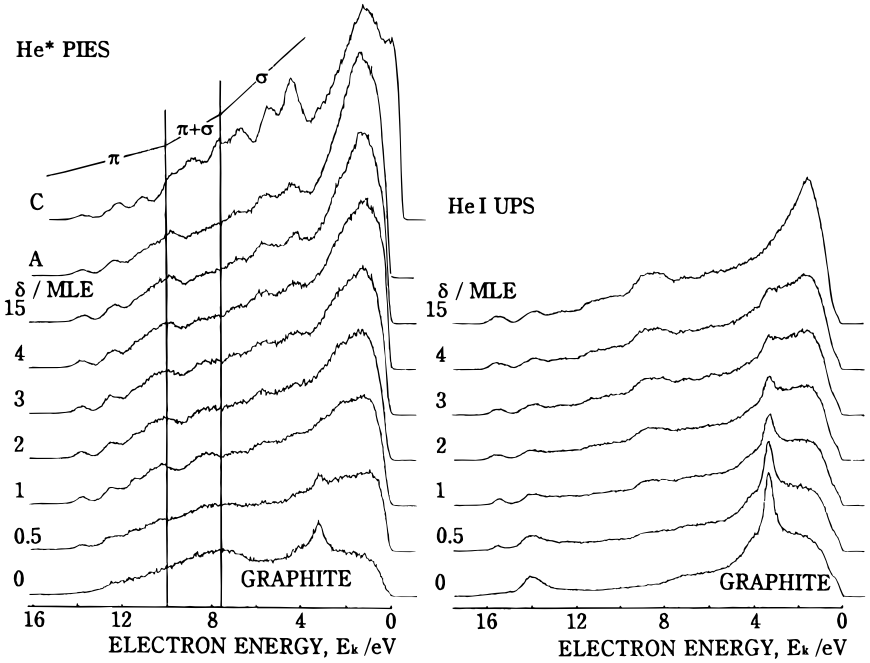

Figure 65. Change in the He*(2^3S) PIES and He I UPS of a pentacene film on a graphite substrate at 123 K with increasing amount of deposition δ, 0 to 15 MLE. The PIES of an amorphous (15 MLE on a stainless steel substrate at 123 K; curve A) and a crystalline film (30 MLE on a stainless steel substrate at room temperature; curve C) are also shown for comparison.

In contrast, the PIES of film II has intense π_5 and π_4 bands and is similar to the gas-phase spectrum, indicating that the molecules on the surface of film II are randomly oriented. These observations are consistent with the well-known facts obtained by X-ray diffraction and absorption spectroscopy that thick films of aromatic compounds are polycrystalline when deposited on a relatively hot metal substrate whereas they are amorphous on a cold metal substrate.[310−313] In Figure 64 the separation between the π_6 and π_3 bands for the polycrystalline film I is wider than those for the amorphous film and gas. This is due to the change in the conformation of the molecule; the splitting of the π_6 and π_3 MO's is larger for the former than for the latter, because it is reported that the two phenyl rings of biphenyl are coplanar in the crystal, but nonplanar in the gas phase (twisted about the central C−C bond by about 42°).[314]

c. Pentacene. Since PIES probes the outermost surface layer selectively but is incapable of detecting inner layers, UPS has been always applied with PIES to study the growth of extrathin films. Figure 65 shows the changes in the PIES and UPS of a pentacene film on graphite at 123 K with increasing deposited amount ($\delta = 0-15$ MLE).[35,264] In the figure the PIES of an amorphous (A) and crystalline (C) films are also shown.[291] The UPS of graphite changes slowly into that of pentacene: the conduction band peak of graphite is attenuated steadily, which suggests that the film becomes thick without formation of islands. On the other hand, the change in the PIES is, of course, the most drastic between $\delta = 0$ and 1 MLE, since electrons from pentacene are selectively observed at 1 MLE, when a monolayer is formed. In the PIES of thicker films, however, we can find a gradual increase in the intensity of the σ bands relative to that of the π and at 15 MLE the PIES shows appearance very similar to that of an amorphous film (curve A) but unlike that of a crystalline one (curve C). These findings indicate that the surface molecules gradually become tilted with increasing δ, to a degree as in the amorphous film. The degree of molecular tilt in the amorphous film is, however, very small compared with that in the crystalline one, where the long axis of a pentacene molecule is almost perpendicular to the film surface,[312,313] because the σ bands in the amorphous film are much weaker than those in the crystalline film. Therefore, molecules in a few MLE films, with smaller relative intensity of the σ bands compared to the case of the amorphous film, are considered to lie almost flat on graphite; the first stage of the film growth can be analyzed as follows by assuming that the flat lying molecules are piled up on the substrate.

Figure 66[35,264] shows the first bands in the PIES and UPS of the pentacene film shown in Figure 65. The shape of the PIES band is unchanged irrespective of the number of layers ($N = \delta$) because only the outermost surface layer contributes to the spectra. The slight broadening of the band width from $N = 2$ can be ascribed to the site inhomogeneity of the top-layer molecules which occupy various nonequivalent positions on the second-layer molecules. In the UPS involving inner layers as well as the outermost the peak position and the band shape changes from $N = 2$. For $N = 2$ to 4 UPS bands are decomposed into the contribution of the outermost layer (solid curve) and that of inner layers (broken curve). From this result we can obtain the value of ~0.3 eV as the separation between the peaks for the outermost layer and inner layers.

If electrons photoemitted from an inner layer pass through one overlayer toward the surface with a survival probability ρ, the integrated intensity of the first band for N layers $I(N)$ relative to that for the monolayer $I(1)$, is given as

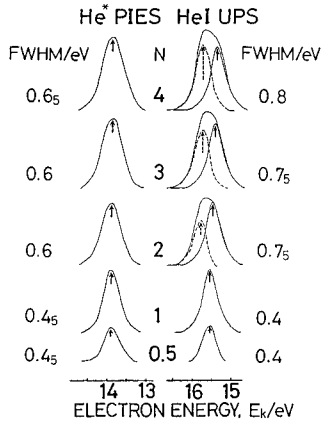

Figure 66. The first bands in the He*(2^3S) PIES and He I UPS of a pentacene film on graphite. The numbers of layers N are changed 0.5 to 4. For $N \geq 2$ each UPS band is decomposed into the contribution of the outermost layer (solid curve) and that of inner layers (broken curve). The full width at half maximum (FWHM) is also shown for each PIES and UPS band. (Reprinted with permission from ref 264. Copyright 1984 The American Physical Society.)

$$I(N)/I(1) = \sum_{k=1}^{N} \rho^{k-1} \qquad (36)$$

Using a least-squares fit of the observed $I(N)/I(1)$ to this equation, we obtained 0.53 as the value of ρ. From this value the escape depth of photoelectrons can be calculated to be 18 Å.

It is worthwhile to note that piled-up monolayers are very liable to sublime under vacuum; pentacene molecules begin to desorb at 150 K.[291]

d. Other Polycyclics. In the early stage of the PIES investigation, thick polycrystalline films of naphthacene, perylene, and coronene formed on an unclean Cu or stainless-steel substrates at room temperature, were used to study the deexcitation channel, secondary electron feature, and the character of the potential energy curve between the metastable and the organic surface.[23,257] An anthracene film served for the interpretation of PIES band intensities to be established:[26] the observed enhancement of a band in the solid PIES was explained in terms of the nature (especially local distribution) of the corresponding MO and the orientation of surface molecules for the first time.

e. Pyridine.[267] In the PIES of pyridine adsorbed on an evaporated Ag substrate held at 125 K, the relative intensities of the bands due to the N nonbonding and π_3 MO's increased gradually with pyridine exposure of 1.2 to 50 L. The energies of the π_2 and π_1 MO's were observed to be about 0.5 eV higher than those at several tens of Langmuirs and for gas-phase pyridine. These findings led to the presumption that at monolayer coverage (~1.2 L) pyridine molecules were chemisorbed with high inclination on the Ag surface with N−Ag bonding and that they were oriented randomly at much higher exposures.

3. Phthalocyanines

a. Iron Phthalocyanine and Magnesium Phthalocyanine. A methodology was presented to analyze the orientation and electronic structure of molecules alternately. Two kinds of iron phthalocyanine (FePc) films were taken as the specimens for this objective since the variety of MO's in FePc, i.e., π, σ, and 3d-like MO's with different types of spatial distribution, is of great help for band assignment. Figure 67a shows the PIES and UPS of the FePc films.[278] Films I and II were prepared by depositing 1 MLE of the sample onto a graphite substrate at 213 K and 15 MLE onto a stainless steel substrate at room temperature, respectively. In the UPS of both films, well-corresponding bands a−d are observed. These bands except band a are related to many MO's coexisting in narrow energy regions. On referring to other experimental and calculated results for various Pcs and related compounds,[315−325] band a is attributed to a π MO distributed on the inner porphine-like ring whereas bands b and c are considered to be mainly due to MO's with large contribution of the benzene rings.

In the PIES of film I, the graphite conduction band peak is almost missing, indicating that the film is a monolayer composed of flat-lying molecules. Hence, MO's spreading perpendicularly to the molecular plane (π MO's and/or $3d_\perp$-like MO's, see below) must be responsible for bands A_I−C_I because they are effectively attacked by metastables. The PIES and UPS of film I are compared in detail in the top panel of Figure 67a. Band C_I, which apparently corresponds to UPS band c due to π and σ MO's, is ascribable to π MO's. On the other hand, the peaks of bands A_I and B_I are located at lower E_k's by 0.4 and 0.3 eV, respectively, compared to those of bands a and b in the UPS. These bands are attributed to $3d_\perp$-like MO's for the following reasons: (1) the positions of bands A_I and B_I agree well with those of "3d bands" in the XPS of other FePc films;[278,315,316] (2) among the 3d AO's of the Fe atom, the $3d_\perp$-AO's ($3d_{yz}$, $3d_{zx}$, and $3d_{z^2}$) spreading normal to the molecular plane (xy plane) are apt to interact with metastables; (3) $3d_\perp$-like MO's are exposed outside the molecular surface more prominently than the π MO's made up of the 2p AO's (see Figure 67b), and, therefore, more effectively attacked by metastables in the flat molecular orientation.

Since no bands are found on the lower E_k side of band C_I in the PIES of film I, there must be no π MO's in this region. Therefore, four bands D_{II}, E_{II}, F_{II}, and G_{II} in the PIES of film II and also UPS bands d of both films are assigned to σ MO's, which hardly interact with metastables in the flat orientation. The enhancement of these σ bands in the PIES indicates that the molecules are tilted in film II, because metastables can interact effectively with σ MO's in this case (see Figure 67c). Bands A_{II}−C_{II} in the PIES of film II correspond well to bands a−c in the UPS of the same film (Figure 67a). Accordingly, band A_{II} is assigned to a π MO distributed on the porphine-like ring, whereas bands B_{II} and C_{II} are mainly attributed to the benzene-derived MO's. It is understandable from Figure 67c that not only σ but π MO's can interact effectively with metastables in the tilted orientation. The $3d_\perp$-like MO's distributed around the center of the molecule, however, are hardly attacked by metastables because of their little oozing outside the surface of film II. This accounts for the absence of the $3d_\perp$-like bands in the PIES. Since

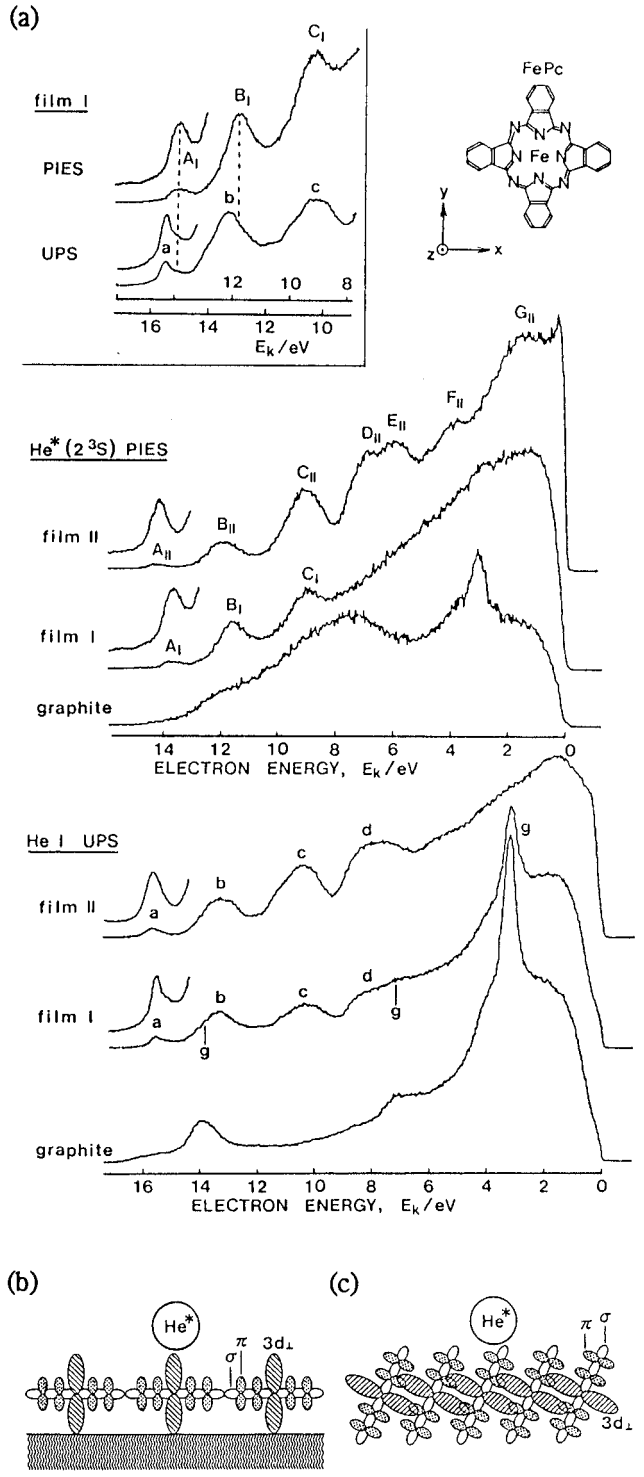

Figure 67. (a) He*(2^{3}S) PIES and He I UPS of iron phthalocyanine (FePc) evaporated films. Film I was prepared on a graphite substrate held at 213 K and film II on a stainless steel substrate at room temperature. The amount of deposited FePc was 1 MLE for film I and 15 MLE for film II. The spectra of the graphite substrate are also shown. The contribution of graphite to the UPS of film I is indicated by g. In the top panel, the high E_k parts of the PIES and UPS of film I are compared in detail. (b and c) Schematic diagrams showing the interaction between surface molecules and a metastable helium atom: (b) film I and (c) film II. Molecules in inner layers are omitted in (c). (Reprinted with permission from ref 278. Copyright 1990 The American Physical Society.)

band C_{II} is more enhanced than band C_I, σ MO's must be also present in the energy region of band C_{II}.

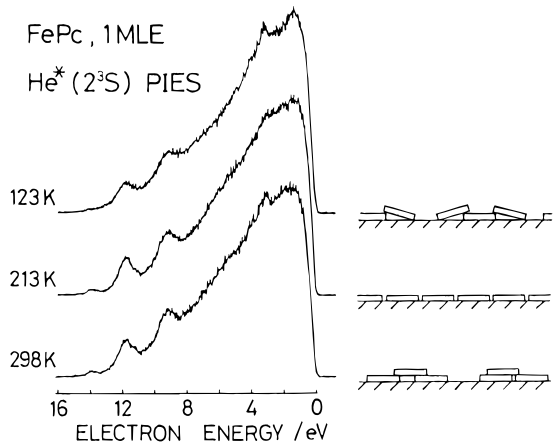

Figure 68. Thermally induced change in the He*(2^{3}S) PIES of an FePc film deposited by 1 MLE on a graphite substrate at 123 K. The film structure corresponding to each spectrum is illustrated on the right. (Reprinted with permission from ref 265. Copyright 1984 Elsevier.)

In the PIES of a magnesium phthalocyanine (MgPc) monolayer on graphite,[278] the first two bands A′ and B′ are weaker than bands A_I and B_I in the FePc monolayer, respectively. Furthermore, in contrast to the case of FePc, the positions of bands A′ and B′ are close to those of the corresponding bands in the UPS of MgPc. These findings are in line with the fact that the central metal atom Mg lacks d electrons; the PIES bands of MgPc are purely due to π MO's, being free from the influence of $3d_\perp$-like MO's.

It was thus concluded that the "3d bands" observed in the XPS of FePc are due to the $3d_\perp$-like MO's and there is no π MO's at E_k's lower than that for band C_I. It was also confirmed that both π and σ MO's are responsible for UPS band c. Thus, the PIES of solid-phase molecules with appropriate orientation provides us clues to the elucidation of the electronic structure. In the above study, the knowledge of the orientation of surface molecules is required although its precise "determination" is not necessary. The flat orientation is deduced from the disappearance of the substrate peak in the PIES of a 1 MLE film. From the knowledge of the flat orientation for film I, the assignment of the PIES bands can be made, and from their relative intensity, in turn, the tilted orientation for film II is obtained. Thus we can advance the investigation clarifying the orientation and electronic structure of the molecule, alternately.

Next we will describe the change in the molecular aggregation of the monolayer film. Figure 68 shows the thermally induced change in the PIES of an FePc film deposited by 1 MLE onto a graphite substrate held at 123 K.[265] The spectrum at 123 K has weak FePc bands due to the $3d_\perp$-like and π MO's and the distinct conduction band peak of graphite. At 213 K the FePc bands become stronger and the graphite peak is almost lost. At 298 K the FePc bands become a little weaker and the graphite peak reappears. These observations can be interpreted as a result of a change in molecular aggregation shown on the right of Figure 68. Upon deposition at 123 K, FePc molecules "freeze" on the cold substrate and lie with random orientation, partially overlapping one another. This causes lower coverage and decrease in the intensity of the FePc bands. When thermal

energy allows the molecules to move at 213 K, a closely packed monolayer is formed owing to the interaction between the graphite and the FePc molecules. At 298 K the molecules can diffuse on the substrate to form islands at preferred sites. Consequently, the graphite peak appears again and the FePc bands become weak in the PIES. This model of the stable island structure is supported by the observation that the PIES at 298 K did not change upon recooling the film to 213 K. It should be noted that the molecules lie flat in the islands because no σ bands are found in the spectrum.

The process of film growth was also investigated for FePc layers on graphite at 213 K. It was found that FePc molecules have a tendency to maintain flat orientation in films thicker than those of pentacene; in the PIES the σ bands were completely missing at 5 MLE and much weaker than the π bands even at 20 MLE.[292] (Note that the σ bands of pentacene is as strong as the π already at 15 MLE in Figure 65.) This indicates that the flat, piled-up arrangement is stable for such a planar molecule as FePc with a larger molecular plane.

b. Chloroaluminum Phthalocyanine. A double-faced molecule ClAlPc exhibits another type of molecular aggregation dependent on the substrate temperature.[288] An amorphous film was formed on deposition onto a graphite substrate at 103 K, but it changed into a closely packed monolayer upon heating to room temperature. The difference in the behavior between FePc and ClAlPc is considered to be due to the difference in the molecular structure; unlike FePc, ClAlPc cannot form islands easily, because of the presence of the Cl atom outside the Pc ring plane.

Figure 69a shows the change in the PIES of a ClAlPc film prepared on graphite held at room temperature with increasing deposited amount δ.[288] In the figure bands A, B, and E correspond to bands A′, B′, and C′ in the PIES of the MgPc monolayer;[278] band A is assigned to a π MO of the inner porphine-like ring (π_P MO); bands B and E are correlated to π MO's with large contribution from the benzene rings (π_B MO's). On the other hand, bands C and D are due to the nonbonding MO's of the Cl atom, $n_{||}$ and $n_\perp$, which are distributed parallel and normal to the molecular plane, respectively (see Figure 69b1). Band F is ascribed to σ MO's. Since the graphite conduction band peak is reduced to one-half at 0.5 MLE and almost zero at 1 MLE, Pc rings must be oriented parallel to the substrate. Furthermore, bands B, C, and D are strong and bands A and F are scarcely seen at 1 MLE. This indicates that ClAlPc molecules protrude Cl atoms outside the film at 1 MLE because in this orientation metastable atoms interact much more effectively with the $n_{||}$, $n_\perp$, and π_B MO's exposed outside than the π_p and σ MO's shielded by the Cl and π_B orbitals (see Figure 69b1). Bands C and D become weaker and band F stronger with increasing δ. This is ascribed to the gradual tilt of Pc rings in the outermost layer, because, in tilted orientation, the $n_{||}$ and $n_\perp$ MO's are partly shielded by other MO's from metastables, whereas the σ MO's are exposed outside the film surface, giving appreciable band intensity (cf., Figure 69b2).

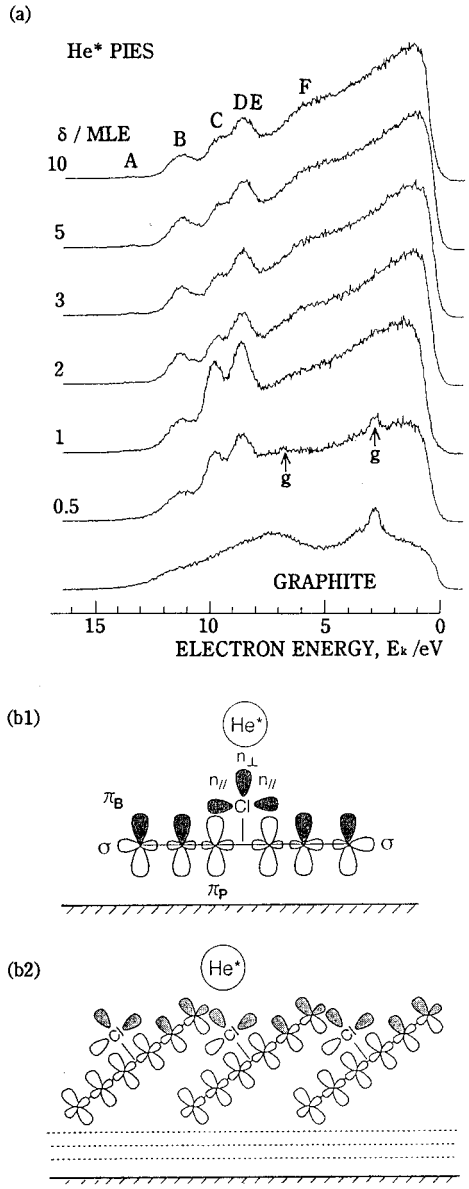

Figure 69. (a) Change in the He*(2^3S) PIES of a chloroaluminum phthalocyanine (ClAlPc) film on a graphite substrate held at room temperature with increasing amount of sample deposition δ. (b) Schematic diagrams of ClAlPc molecules interacting with a helium metastable atom in flat (1) and tilted orientations (2). (Reprinted from ref 288. Copyright 1995 American Chemical Society.)

The spectral change in Figure 69a also shows that the interaction between the π_B MO's and metastable atoms becomes stronger and that the $\eta_{||}$ MO is more effectively shielded than the $\eta_\perp$ with the molecular tilting.

A different growth of a ClAlPc film was found on a MoS_2 substrate.[287,290] At 1 MLE molecules deposited at room temperature form islands in which the Cl atoms of the top molecules are mainly directed to the substrate. Upon heating to 373 K the film structure changes to the stable one and molecules are oriented flat to the substrate with the Cl atoms protruding outside the film. According to LEED and ARUPS studies, both at room temperature and 373 K molecules form square lattices whose molecular azimuthal angle is about 6° with respect to the three equivalent surface crystal axes of the MoS_2 substrate. At 2 MLE molecules are tilted in the second layer

with Cl atoms mainly directed to the substrate. At 5 MLE ARUPS indicates that molecules are tilted with the inclination angle of about 10° to the substrate. In this case, the relative band intensity of PIES suggests that both molecules with Cl atoms directed to the outside and those to the substrate are present.

4. Acrylonitrile and Polyacrylonitrile

Perreau et al. made the surface identification of PAN film (100 Å thick) prepared by the electrolysis of acrylonitrile at the surface of a Ni electrode, comparing its PIES with gaseous spectra of acetonitrile and acrylonitrile.[272] The PIES of the film showed an very intense broad band at E_k 6.5 eV, where the N lone pair (nonbonding, n) bands for both gas phase molecules appear. According to the authors, although they did not give the chemical structure of the chain end clearly, the intense peak dominating the film spectrum is also due to the n electrons, which suggests that the cyano groups are exposed outside the film surface.

In relation to this study, two different orientations of acrylonitrile molecules were studied by PIES.[268] In chemisorption from vapor phase (layer I), molecules are bound on metal surfaces through the polar cyano groups. On the other hand, in chemisorption from liquid phase (layer II), under the influence of the electric field provided by the dipole layer between the cathode and an electrolytic solution in an electrochemical cell, molecules with high dipole moment are flipped so that the vinyl group is constrained to be close to the cathode surface. The PAN film surface from which cyano groups sprout was considered to be originated from monomer molecules thus flipped. In fact, the PIES indicated that vinyl and cyano groups were exposed outside in layers I and II, respectively.

D. Chemical Reactions in Organic Film Surfaces

1. Photooxidation at the Outermost Surface Layer

The ability of PIES to detect a surface reaction sensitively was first demonstrated by applying it to the photochemical reaction of aromatic compounds.[260] Figure 70 shows the PIES and UPS for the photooxidation process of a tetracene (naphthacene) film. Curves 0 show the spectra for the fresh film and curves 1 those after irradiation for 1 h under oxygen pressure of 2 Torr. In curves 1 a slight change is observed for the PIES, whereas no change is found for the UPS. Further irradiation for 1 h under the same oxygen atmosphere (curves 2) strengthens this tendency to the spectral changes. The change in the PIES can be explained in terms of the separation of the conjugated system of tetracene into those of benzene and naphthalene:

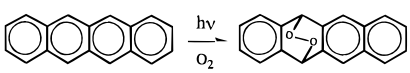

In Figure 70, T, B, and N denote the peak positions corresponding to tetracene, benzene, and naphthalene. We can see from the figure that the intensity of the bands due to tetracene gradually decreases

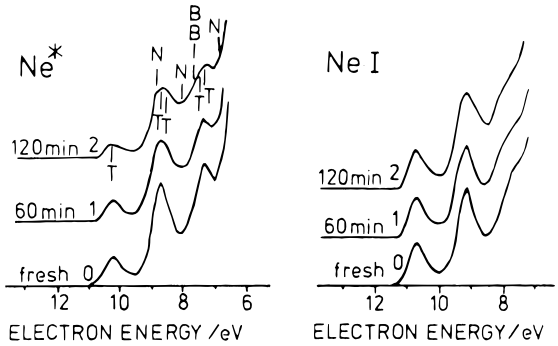

Figure 70. Ne*($^3P_2$) PIES and Ne I UPS for the photooxidation process of a tetracene (naphthacene) solid film. Curve 0 show the spectra for the fresh film, curve 1 those after irradiation for 1 h under oxygen pressure of 2 Torr, and curve 2 those after further irradiation for 1 h under the same oxygen atmosphere. In the PIES, T, B, and N denote the peak positions corresponding to tetracene, benzene, and naphthalene. (Reprinted with permission from ref 260. Copyright 1982 Elsevier.)

during photooxidation, while those due to benzene and naphthalene increase. These results show that the photooxidation mainly takes place at the outermost surface layer and that it can be sensitively detected by PIES. The smaller change in the UPS indicates that the reaction rate for inner layers is much slower than that for the outermost layer because the process of the reaction is controlled by the diffusion of oxygen into inner layers. These conclusions were supported by the result for 5,6,11,-12-tetraphenylnaphthacene (rubrene).[260] In this case, the observed changes in the UPS due to the photooxidation reaction were much more rapid compared to the case of tetracene, because the four phenyl groups of rubrene make molecular packing in the solid very loose, resulting in faster oxygen diffusion into inner layers.

2. Reticulation Reaction of Polyacrylonitrile[261−263]

There are a series of early studies in which PAN grafted on an Fe support was heated and reticulated by intrachain (and interchain) cyclizations with opening of CN bonds.

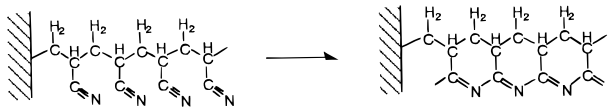

The insulating and conducting properties of the film influenced by heating and reticulation were studied by PIES and UPS.

3. Benzene Formation from Acetylene

The chemical change of adsorbed acetylene to benzene on a Pd(111) surface was studied by MAES, although it was used as a supplementary tool of UPS.[30] The spectral dependences of this chemisorbed system on exposure and temperature are rather complicated. Curve a in Figure 71 is the MAES of a clean Pd(111) substrate. Curve b obtained after 5 L exposure at 140 K was attributed to a chemisorbed species called α state combined to the surface by π/di-σ bonding. Curve c obtained at ambient acetylene pressure of 10^{-7} Torr at 300 K was ascribed to

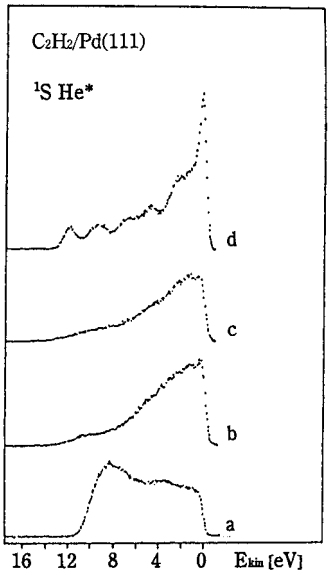

Figure 71. He*(2^1S) MAES of acetylene adsorbed on a Pd(111) substrate: (a) clean Pd(111) surface; (b) after 5 L exposure of C_2H_2 at 140 K; (c) at ambient C_2H_2 pressure of 10^{-7} Torr at 300 K; (d) after 300 L exposure of C_2H_2 at 140 K. (Reprinted with permission from ref 30. Copyright 1983 Elsevier.)

a different species β state with distorted geometry but unchanged stoichiometry. This species was unreactive and could also be formed by annealing the α species to 300 K. High exposure (100 L) at 140 K provided curve d due to the formation of a new species, which was identified as benzene because energy differences between various bands in curve d agreed well with those for gaseous benzene and benzene adsorbed on a Pd(111) substrate. This transformation, i.e., an cyclotrimerization of acetylene was found to take place only if the surface was covered with α state. Benzene molecules were only weakly held on the surface and started to desorb at about 150 K. It is of note that features in curves b and c (as well as curve a, of course) did not correspond to those in the UPS, indicating that α and β states deexcite metastables via RI+AN. This means that thin layers of acetylene molecules adsorbed flat to the Pd substrate can not shield Pd d orbitals. Similar oozing of metal d orbitals through the benzene ring was observed for benzene molecules adsorbed flat to a Pd substrate[30] and a sandwiched metal complex $(C_6H_6)_2Cr$.[172]

4. Intermonolayer Charge-Transfer Reaction

A stimulating attempt was carried out, in which charge transfer complexes were formed between the monolayers of tetrafluorotetracyanoquinodimethane (TFTCNQ; electron acceptor) and tetramethyltetraselenafulvalene (TMTSF; electron donor).[280] Before introducing this attempt, the PIES for single-component films will be described first.

The PIES of TFTCNQ films (0−10 MLE) on graphite at 123 K are shown in Figure 72.[280,281] At 1 MLE, the presence of strong π bands 1−3 and the absence of the substrate features point out that TFTCNQ molecules are arranged parallel to the substrate. Band 4 is related to π and nonbonding MO's localized on the CN group, n(CN); band X can be ascribed to $[TFTCNQ]^-$ formed by electron transfer from the graphite substrate (see section V.D.5). At 10 MLE very intensified band 4 indicates that molecules are considerably tilted exposing their CN groups to the metastable beam (see the left of Figure 72). The relative intensities of bands 1 and 2 at 10 MLE is consistent with this orientation at the outermost layer: band 1 due to the $b_{1u}(\pi)$ MO is enhanced relative to band 2 related to the $b_{2g}(\pi)$ and $b_{3g}(\pi)$ MO's, because the b_{1u} MO is mainly distributed on the methyne C atoms exposed outside, while the b_{2g} and b_{3g} MO's are predominantly distributed on the ring C atoms (see the right of Figure 72). At 2 and 3 MLE the relative band intensities indicate that the degree of tilt is smaller than at 10 MLE. At 2 MLE, however, the presence of band X due to $[TFTCNQ]^-$ ions shows that the second layer molecules are somewhat tilted and that they cannot cover completely the ions in the first layer.

In contrast to the case of TFTCNQ, it seems rather surprising that a quasiplanar compound TMTSF lies

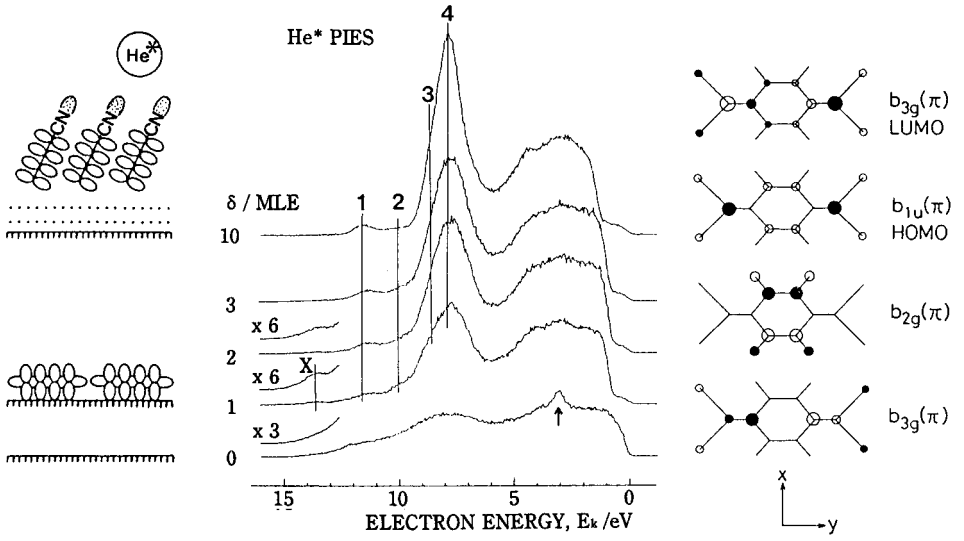

Figure 72. He*(2^3S) PIES of tetrafluorotetracyanoquinodimethane (TFTCNQ) films with increasing amount of sample deposition δ. The molecular orientation at the outermost surface layer is schematically shown on the left for 1 and 10 MLE films. The lowest unoccupied π MO and the three highest occupied π MO's of TFTCNQ are shown on the right. (Reprinted with permission from ref 280. Copyright 1991 Elsevier.)

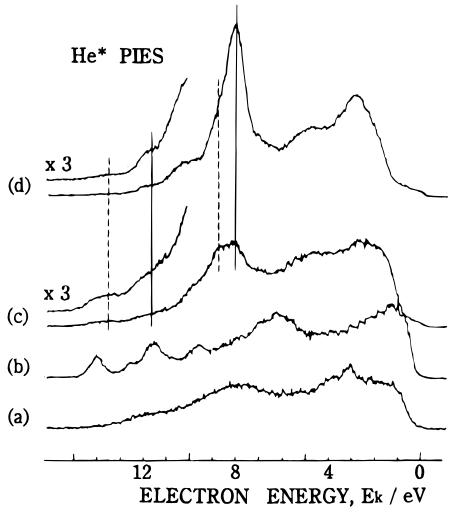

Figure 73. He*(2^3S) PIES of (a) graphite substrate, (b) tetramethyltetraselenafulvalene (TMTSF) (1 MLE)/gr (1 MLE TMTSF on graphite), (c) TFTCNQ (1 MLE)/TMTSF (1 MLE)/gr, and (d) TFTCNQ (2 MLE)/TMTSF (1 MLE)/gr. The bands denoted by solid and broken lines are due to TFTCNQ and $[TFTCNQ]^-$, respectively. (Reprinted with permission from ref 280. Copyright 1991 Elsevier.)

flat in a monolayer on graphite at 123 K and that the PIES of the film at 10 MLE is almost identical to that at 1 MLE, showing the same flat molecular arrangement.[280]

Figure 73 shows the PIES of a TMTSF monolayer on graphite (denoted by TMTSF(1)/gr, curve b) and a 1 MLE and a 2 MLE film of TFTCNQ prepared on TMTSF(1)/gr (denoted by TFTCNQ(1)/TMTSF(1)/gr (curve c) and TFTCNQ(2)/TMTSF(1)/gr (curve d).[280] These films were prepared at 123 K. In the PIES of TFTCNQ(1)/TMTSF(1)/gr the bands related to TMTSF are missing and the bands located at 13.6 and 8.7 eV are characteristic of $[TFTCNQ]^-$, while the bands at 11.6 and 7.9 eV are due to neutral TFTCNQ. Thus, TFTCNQ molecules mostly cover the TMTSF monolayer with flat molecular orientation and some of them are changed to $[TFTCNQ]^-$ forming charge-transfer complexes with TMTSF. The ratio of $[TFTCNQ]^-$ ions is estimated to be 70−80% from the intensity of the X band at 13.6 eV. The PIES of TFTCNQ(2)/TMTSF(1)/gr is rather similar to that of TFTCNQ(10)/gr in Figure 72, giving the strong band 4. Therefore, TFTCNQ molecules are tilted at the outermost layer. This is supported by the fact that the band X slightly appears in the PIES of TFTCNQ-(2)/TMTSF(1)/gr.

A 1 MLE and a 2 MLE film of TMTSF were also deposited on TFTCNQ(1)/graphite.[280] The PIES of TMTSF(1)/TFTCNQ(1)/gr showed that TMTSF molecules on TFTCNQ were partly altered to $[TMTSF]^+$ ions, forming charge transfer complexes with TFTCNQ. In TMTSF(2)/TFTCNQ(1)/gr the surface was found to be mostly covered with neutral TMTSF molecules tilted a little.

5. Formation of Organic Anions without Counterions

As stated in the last section, both neutral TFTCNQ molecules and $[TFTCNQ]^-$ ions were present in a TFTCNQ monolayer prepared at 123 K on graphite. The change in the PIES upon heating the monolayer to 183 K indicated that the neutral molecules were desorbed, leaving the ions that were more stable, owing to the charge-transfer interaction with the substrate.[281] The PIES of pure $[TFTCNQ]^-$ was obtained by subtracting the substrate emission from the PIES of the heated film. The estimated ratio of TFTCNQ molecules left as ions on the substrate was ∼40−50%. This value is reasonable, because the film would be unstable, owing to the interaction of electric dipoles closely aligned side-by-side, if all the molecules were ionized on the substrate. In fact, the PIES of a 0.4 MLE film had almost the same appearance as that of the heated film. This means that molecules are initially adsorbed on graphite as ions separated from each other and that neutral molecules occupy positions among ions at the later stage of the monolayer formation. The ion formation is considered to be due to a strong electrophilic character of TFTCNQ because ions could not be detected in TCNQ films. Since neutral TFTCNQ arises on the electron emission from $[TFTCNQ]^-$, the bands in the PIES of pure $[TFTCNQ]^-$ correspond to states of the TFTCNQ molecule. According to ab initio MO calculations, the first two bands X and Y at 13.6 and 12.3 eV were assigned to the ground state of TFTCNQ and the lowest triplet one due to the electron excitation from the HOMO to the LUMO, respectively.

6. Formation of an Organic Monatomic Layer by Intramonolayer Polymerization

As have been reviewed above, when vapor deposited onto a graphite substrate cooled adequately, a planar or linear organic compound forms a monolayer in which the molecule is oriented with the carbon skeleton plane parallel to the substrate surface. Molecules are liable, however, to be desorbed[282,285,286,291,292] as well as be disordered in aggregation since they are gathered by weak VDW interaction. Therefore, stronger interaction must be introduced among them to utilize a unique aggregation for material design. A new substance can be created if molecules tailored by considering two-dimensional packing and reactivity are arranged suitably on a solid surface and undergo a controlled intermolecular reaction in a monolayer. From this standpoint, "surface topochemical reactions" were designed with tailored compounds 17,19-hexatriacontadiyne (HTDY) and 1,15,17,31-dotriacontatetrayne (DTTY).[289] First, HTDY molecules laid in a monolayer were combined one dimensionally by photopolymerization: the diacetylene units in each column of Figure 74a were polymerized to stitch up the rows of the flat-lying alkyl chains and yielded a sashlike single sheet of a planar carbon network, *atomic sash* (Figure 74b). The process was monitored by PIES.[285] Prior to this work, however, a similar product was also formed by a more complicated process, the selective polymerization of the outermost molecules in a 5 layer film followed by the desorption of monomer molecules in the inner layers.[282]

Next to the *atomic sash*, a macromolecular sheet spreading two dimensionally was prepared: intramonolayer polymerization of DTTY yielded a single sheet of a clothlike macromolecule (*atomic cloth*)

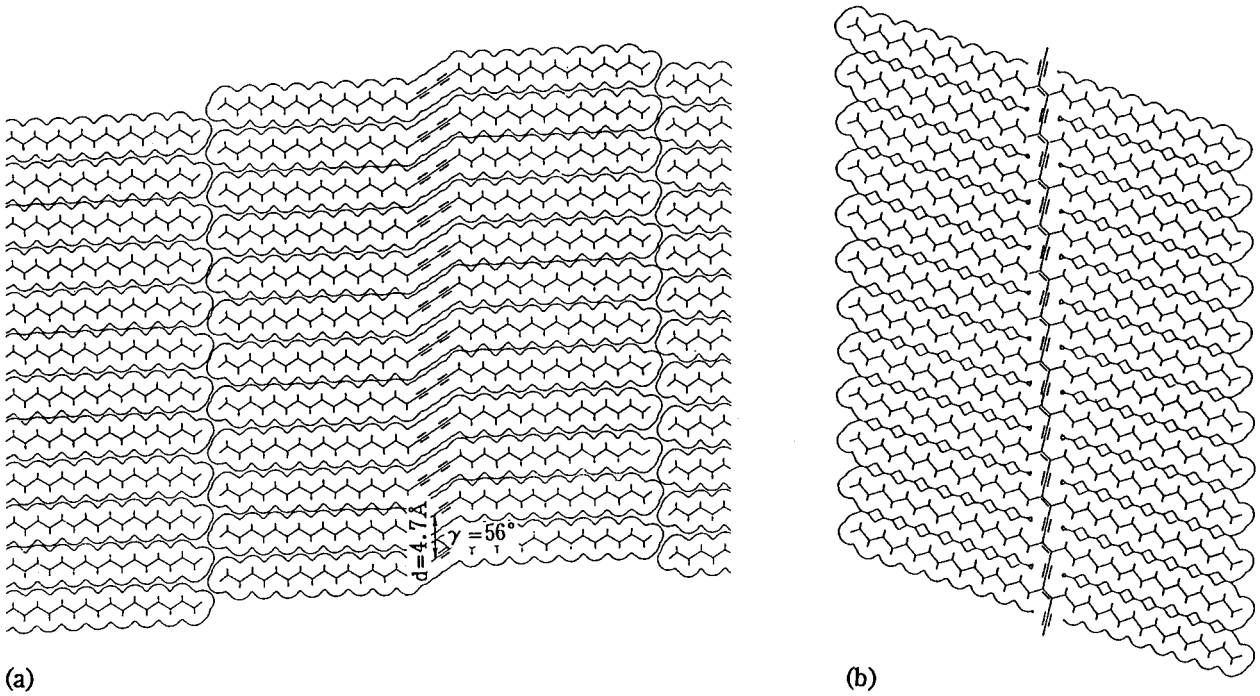

Figure 74. Schematic diagrams for (a) a monolayer of 17,19-hexatriacontadiyne (HTDY) molecules laid flat in all-trans conformation and (b) a single sheet of a sashlike macromolecule (*atomic sash*) produced by polymerizing HTDY molecules in each column of (a). (Reprinted from ref 285. Copyright 1995 American Chemical Society.)

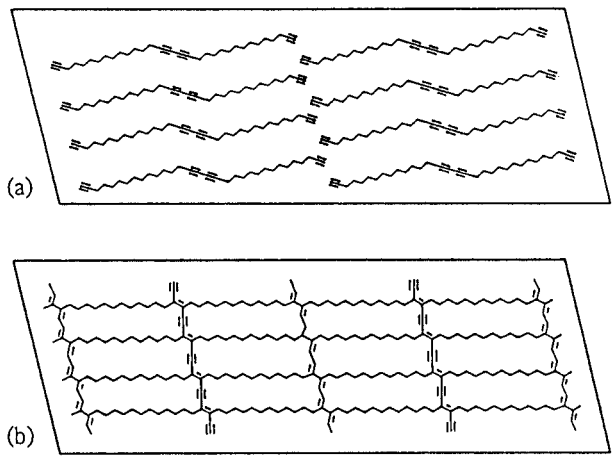

Figure 75. Intramonolayer polymerization of 1,15,17,31-dotriacontatetrayne (DTTY). (a) Arrangement of DTTY molecules in a monolayer. (b) Product of photopolymerization, *atomic cloth*: a single sheet of a clothlike macromolecule comprising the columns of polydiacetylene and polyacetylene chains alternately cross-linked to the rows of alkyl chains. (Reprinted with permission from ref 286. Copyright 1995 The American Physical Society.)

comprising the columns of polydiacetylene and polyacetylene chains alternately cross-linked to the rows of lying alkyl chains (see Figure 75).[286] The *atomic cloth* (and *atomic sash* as well, in a sense) can be regarded as an organic monatomic layer.

The PIES of a DTTY monolayer at 213 K is shown as curve 2 in Figure 76a.[286] The disappearance of graphite features and marked enhancement of bands P (pseudo-π, pπ) and S (σ_{2s}) confirms that the molecule orients with the carbon skeleton plane parallel to the substrate. Band D is assigned to the antibonding vertical π (D$\pi_a^{\perp}$) MO of diacetylene, whereas band A is assigned to the antibonding and bonding vertical π (A$\pi_a^{\perp}$ and A$\pi_b^{\perp}$) MO's of the terminal acetylenes (see Figure 76b). Features due to the bonding vertical π (D$\pi_b^{\perp}$) MO of the diacetylene are, however, buried in the overwhelmingly enhanced band P around E_k 10 eV. It should be noted that π MO's distributed on the carbon plane (D$\pi_a^{\parallel}$, D$\pi_b^{\parallel}$, A$\pi_a^{\parallel}$, and A$\pi_b^{\parallel}$) cannot be detected in the PIES for flat molecular orientation. During the exposure to UV light, bands D and A become stretched after 2 h (curve 3) and lose the peaks and afford monotonous features after 20 h (curve 4). This can be attributed to the process that the energies of the D$\pi^{\perp}$ and A$\pi^{\perp}$ MO's split and broaden as the polymerization reaction proceeds and the conjugated system extends. On the other hand, the UV irradiation does not essentially alter the shapes of bands P and S. Furthermore, the irradiated monolayer provides almost the same PIES as curve 4 when heated to 298 K (see curve 5). The unchanged alkyl bands for the irradiated and heated monolayer indicate that the zigzag chains are laid flat during polymerization and heating and also no sign of graphite signals means that molecules are not desorbed. This is a striking contrast to the fact that an unirradiated DTTY monolayer evaporates completely at 298 K. From these observations, it is considered that DTTY molecules are polymerized in the monolayer to form an *atomic cloth* structure. Thus, a single sheet of a two-dimensional macromolecule can be prepared by intramonolayer photopolymerization, during which the electronic structure and orientation of molecules suitably arranged on a solid surface were probed by PIES. Using this method, we will be able to pile up the layer of thickness 4 Å, which is much thinner than the layer composed of standing hydrocarbon chains (thickness ~20 Å) in ordinary LB films. Such a layer will be more easily applicable to the construction of molecular devices.

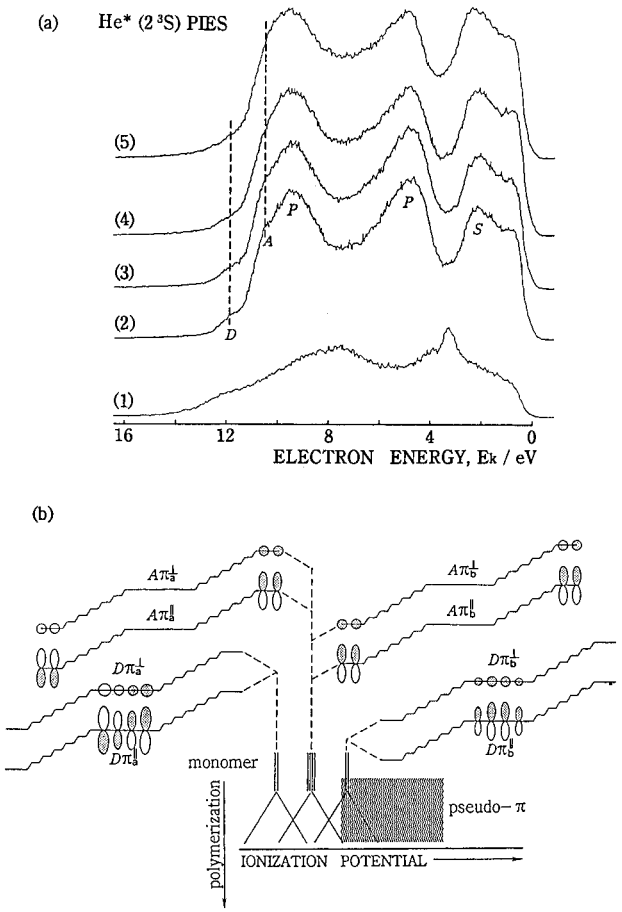

Figure 76. (a) He*(2³S) PIES of a graphite substrate held at 213 K (1) and a DTTY monolayer formed on it (2−5): (2) fresh at 213 K, (3) after 2 h of UV irradiation, (4) after 20 h of UV irradiation, and (5) after heating the irradiated film (4) to 298 K. (b) Schematic diagrams for the π MO's of DTTY, distributed at the diacetylene (Dπ) and terminal acetylene units (Aπ). The energies of D$\pi^{\perp}$ and A$\pi^{\perp}$ MO's split and broaden as the polymerization reaction proceeds and the conjugated π system extends. (Reprinted with permission from ref 286. Copyright 1995 The American Physical Society.)

E. Liquid Surfaces

There are a series of PIES studies applied to the surfaces of organic liquids.[45,46,293−299] The PIES of formamide (FA) was measured first and it was concluded that the molecules at the outermost surface layer are laid flat on the liquid surface.[293,294] A study on a surface active salt tetrabutylammonium iodide in FA showed that I^- anions appear at the outermost surface layer, which unambiguously denied the double-layer model in electrochemistry.[45] The surface segregation phenomena[295−298] as well as the surface composition[295,299] of various binary liquid systems were also investigated by PIES.

We will describe below, as an example, the results for pentadecane ($C_{15}H_{32}$, PD)-FA system.[297] In this case, the charging problem of liquid insulator PD were overcome by preparing its segregated thin layer on a surface of polar solvent FA that was regarded as a conducting liquid substrate. The target of PIES was a vertical liquid beam of 25 mm in length. The whole target could be moved vertically so as to vary the separation between the outlet of the beam and the position of the He* beam. In this way, the effective "surface age" could be varied between 2 and 23 ms. The measurement was started with the polar solvent FA. Then increasing amount of PD was added until the PIES exhibited no signals attributable to the FA substrate owing to the spontaneous segregation of PD, that is, the PD layer formation at the surface. Curves a and b in Figure 77 are the PIES of pure FA and 5% PD in FA ($c = 5\%$) at surface age $t = 3.5$ ms, respectively. In curve b, the characteristic features of FA in curve a, the band at E_k 10 eV and the hallow at 8.5 eV, are still observed, although the hollow is partly filled and a new hollow emerges at 3 eV. At a later stage of surface development at $t = 21.5$ ms, the same mixture provides curve c, which has a distinct peak at 5.7 eV and is completely free from the FA features. In curve c, the relative band intensities are similar to those of standing alkyl chains (see curves II in Figure 59b, and curve I in Figure 61). Therefore, the surface is covered with a closed layer of standing PD molecules. Curve d in Figure 77 shows the PIES for $c = 18.5\%$ measured at $t = 10$ ms. No trace of FA can be found in curve d as well, indicating a complete coverage of the surface with PD. The relative band intensity, however, have changed to become more or less similar to that of the monolayer of lying alkyl chains on graphite (see curves I in Figure 59b, but curve d resembles more closely the PIES of shorter molecules $ZnSt_2$ and HTDY laid flat[282,285]). Hence, in the more concentrated solution showing curve d, molecules are considered to be oriented flat at the outermost surface layer.

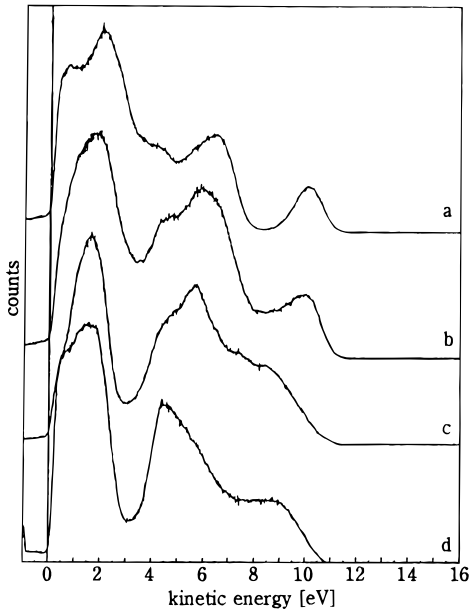

Figure 77. He* (2³S) PIES of organic liquids. (a) Pure solvent formamide (FA), (b) a mixture of 5% by weight of pentadecane (PD) in FA at the age of the surface $t = 3.5$ ms, (c) as before but t is increased to about 21.5 ms, and (d) a mixture of 18.5% by weight of PD in FA at $t = 10$ ms. (Reprinted from ref 297. Copyright 1994 Elsevier.)

VI. Observation of Surface Topology

So far we have discussed the laterally averaged information of surfaces that is given by impact of metastables atoms. In this section we describe the attempts to observe the surface topology using electron emission by metastable atoms.

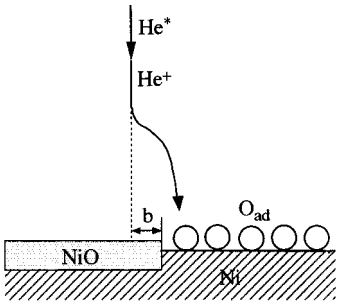

Figure 78. Trajectories of He*/He^+ near the boundary between oxide and chemisorbed oxygen. (Reprinted with permission from ref 124. Copyright 1994 Elsevier.)

Recently Morgner and Tackenberg studied the epitaxial growth of nickel oxide on Ni(100) and Ni(111) surfaces under oxygen exposure.[124] Combining XPS and MAES they could monitor the lateral growth of NiO islands and estimated the average radius of the oxide islands and the number of islands per centimeters squared. Figure 78 shows a trajectory of He* near the boundary between nickel oxide and chemisorbed oxygen on Ni. Near the boundary the lateral electric field is produced, because the work function of NiO is roughly 1.5 eV below that of the chemisorbed oxygen. On NiO having a wide band gap He* atoms deexcite through Auger deexcitation (AD), while on the chemisorbed surface Auger neutralization (AN) followed by resonance ionization (RI) occurs. However, near the border of NiO islands a He* atom is resonance-ionized since it approaches NiO as well as metallic Ni at the same time. As shown in Figure 78, the He^+ ion thus formed is drawn from the NiO to the chemisorption site owing to the lateral electric field near the boundary. In the figure parameter b is the separation between the boundary and the point at which the He* atom should originally hit. The largest b that leads to Auger neutralization of He^+ on the chemisorbed surface is defined as the capture range r_{capt} (the value of r_{capt} is roughly estimated to be 3 Å). Because of the effect of r_{capt} MAES underestimates the contribution of oxide in contrast to the case of XPS that is free from such effect. Morgner and Tackenberg measured the MAES and XPS during oxide growth on Ni. The careful analyses of both spectra gave the average oxide island radius in units of r_{capt} and the number of islands in centimeters squared as a function of the total oxide formed.

Next we describe a more direct method of the observation of surface topology. Harada et al. developed an electron emission microscope using the He*(2^3S) atom as the excitation source.[283,326] Figure 79 shows the schematic diagram of the microscope. It is available for low-energy electron emission microscopy (LEEM), photoelectron emission microscopy (PEEM), and metastable electron emission microscopy (MEEM), depending on the incident beam. For MEEM the intense beam of He*(2^3S) ($\sim 10^{16}$ atoms s^{-1} sr^{-1}) obtained by the metastable source shown in Figure 2 is used because metastables can not be converged unlike photons or electrons. In Figure 79 electrons emitted from the specimen by impact of electrons, photons, or metastables are accelerated to 10 keV and imaged by the electron optical system consisting of a cathode objective lens (COL), two intermediate lenses (IL1, IL2), and three projector lenses (PL1, PL2, and PL3). The final image is observed with a fluorescent screen with two multichannel plates (MCP) and stored in a video tape using a CCD camera. Deflectors (DEF) and stigmators (STG) are used to align the beam and to compensate the astigmatism. An electron energy analyzer (Wien filter) between lenses IL2 and PL1 enables to observe the electron spectrum of the local surface area and the energy-filtered image given by electrons of a selected energy. For the measurement of the local electron spectra, an energy slit S is inserted and the energy of electrons emitted from a local area of the specimen is analyzed by the Wien filter. The local area is selected by adjusting an aperture A. The energy resolution of the Wien filter estimated by electron optical simulation is 0.1 eV. On the other hand, to observe an energy-filtered image, the diffraction plane made by COL and IL1 is set at the position of the aperture A and one diffraction spot is selected. Then the diffraction

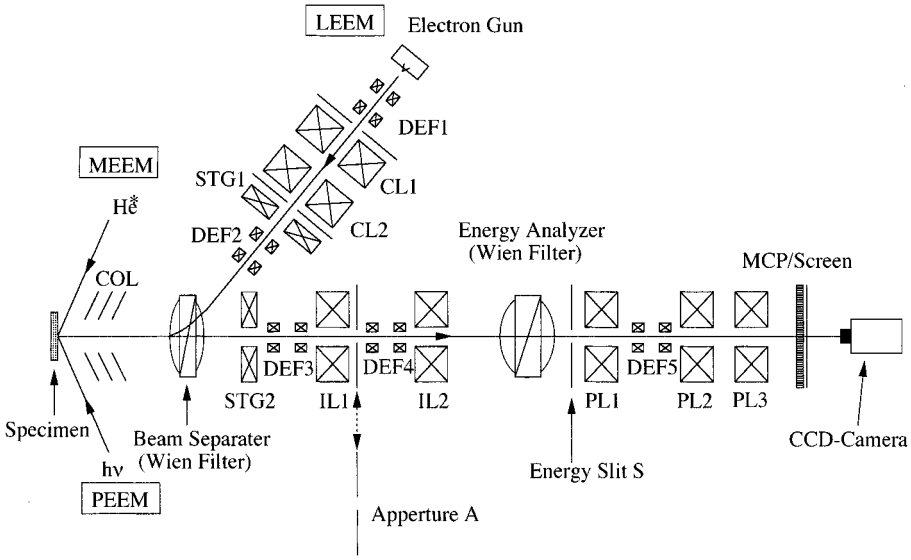

Figure 79. Schematic diagram of the microscope for low-energy electron emission microscopy (LEEM), photoelectron emission microscopy (PEEM), and metastable electron emission microscopy (MEEM). See text for details.

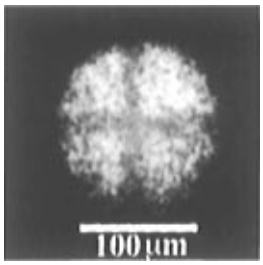

Figure 80. Metastable electron emission micrograph of ClAlPc monolayer islands on a grafoil substrate.

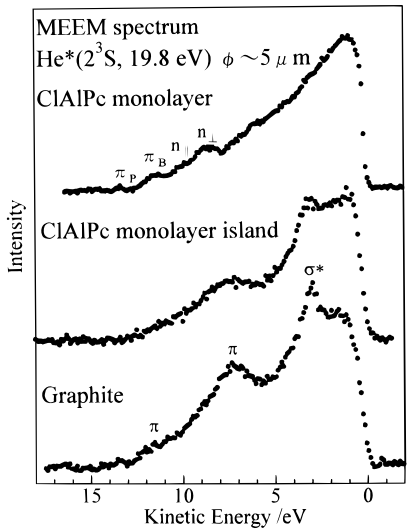

Figure 81. Local MAES of a ClAlPc monolayer, ClAlPc monolayer island and grafoil substrate. The spectra of the monolayer and monolayer island were measured 3 h after the deposition of ClAlPc.

plane by IL2 is set at the entrance of the Wien filter, which gives the energy-dispersed diffraction spot at the position of the energy slit. The diffraction spot with a certain energy selected by the slit is transferred to the real image by the projective lenses. The lateral resolution of the present MEEM is the order of 0.1 μm. It will be much improved by the use of a more intense metastable source and a better image processing system.

Figure 80 shows a metastable electron-emission micrograph of monolayer islands of chloroaluminum phthalocyanine (ClAlPc), which were grown by vacuum deposition using a net mask placed just above a graphite surface. In the figure all the energies of emitted electrons (0−15 eV) were used to produce the image. The light regions are due to ClAlPc islands showing that the ClAlPc monolayer has a higher total emission yield than the graphite substrate. The image of islands is rather vague owing to the diffusion of ClAlPc molecules (see below). Figure 80 indicates that MEEM is not only surface sensitive but also nondestructive. In fact LEEM gave no sign of ClAlPc for monolayers on graphite owing to electron spattering.

Figure 81 shows local MAES of a ClAlPc monolayer, a ClAlPc monolayer island on graphite, and the graphite substrate.[283] The diameter of the probe area ϕ is about 5 μm. The spectra of the monolayer and monolayer island were measured 3 h after the deposition of the sample. In the monolayer spectrum the four bands were already assigned in section

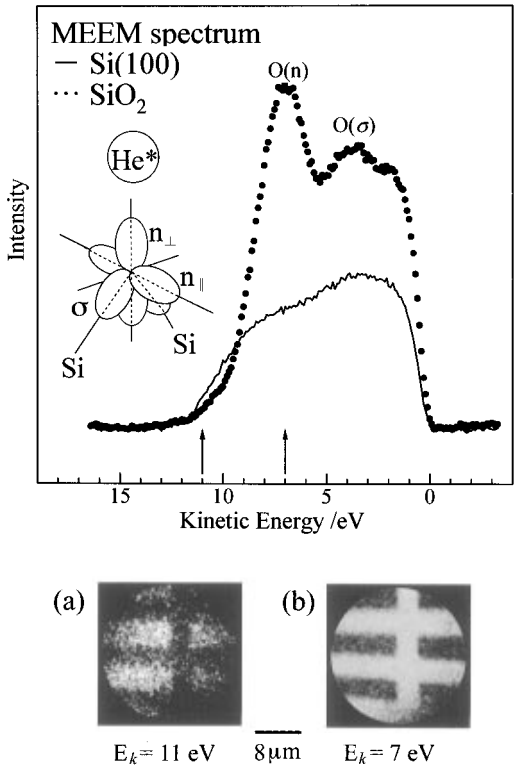

Figure 82. (Top) Local MAES of Si(100) and silicon oxide on Si(100) and (bottom) energy-filtered MEEM micrographs of silicon oxide islands on Si(100) using (a) 11 and (b) 7 eV electrons (indicated by arrows in the spectra, respectively).

V.C.3.b; the first band is related to a π MO of inner porphine-like ring (π_P MO), the second band to π MO's with large contribution from benzene rings (π_B MO's), and the third and fourth bands to the nonbonding MO's of the Cl atom (Cl($n_{||}$) and Cl($n_\perp$)), which are distributed parallel and normal to the molecular plane, respectively (see Figure 69b1). As described in section V.C.3b, the enhancement of the Cl($n_{||}$), Cl($n_\perp$), and π_B bands relative to the π_P indicates that phthalocyanine rings are oriented flat to the substrate with the chlorine atom protruding outside the film surface. (The monolayer spectrum in Figure 81 was measured with the electron emission angle of about 90°, while the corresponding spectrum in Figure 69a was taken with the angle of 60°. Therefore, the former spectrum is more affected by secondary electrons and hence more diffuse than the latter.) Next, in Figure 81 the spectrum of the ClAlPc island is a mixture of the monolayer spectrum and the graphite spectrum, indicating the diffusion of molecules of the ClAlPc island on graphite. From the intensity of the peak due to graphite conduction bands σ^* in the island spectrum, the proportion of ClAlPc molecules diffused from the islands is estimated to be 35%. Thus, the spectrum obtained by MEEM probes the molecular diffusion in the monolayer, as well as the orientation of molecules at the outermost surface layer with high spatial resolution.

Figure 82 shows the local MAES of Si(100) and silicon oxide on Si(100) together with energy-filtered images of silicon oxide on Si(100).[327] The thickness of silicon oxide layer is about 20 μm. Helium metastable atoms deexcite through the AD (PI) process on silicon oxide and through the RI+AD on silicon.[41] In the spectrum of silicon oxide the bands

around 7 and 3 eV are due to the O2p nonbonding ($n_{\parallel}$ and $n_{\perp}$) and bonding orbital (σ), respectively.[41]

The energy-filtered MEEM micrographs of silicon oxide islands on the Si(100) surface are shown in Figure 82a,b, where 11 and 7 eV electrons are imaged, respectively, and the energy width of electrons is about 2 eV in both cases. In Figure 82a the light region is due to silicon, because the spectral intensity of silicon is stronger than that of silicon oxide at 11 eV. It is of note that the contrast of the micrograph reflects the slight difference in the spectral intensity. The contrast is reversed in Figure 82b, where the silicon oxide region is much lighter than the silicon owing to the presence of the strong O2p-(n) band. Thus, using energy-filtered MEEM, we can make the map of the distribution of individual orbitals at the outermost surface layer. This feature of MEEM enables us characteristic surface topological studies, such as the mapping of the molecular orientation of monolayers, the observation of molecular diffusion at the outermost layer, etc.

VII. Conclusions

In this review we have described the characteristics of metastable atom electron spectroscopy (MAES) and its application to various clean and adsorbed surfaces. The advantage of this method is the ability to study the outermost surface layer selectively. In particular, we can probe by MAES the local distribution of individual orbitals exposed outside the surface, which is difficult to observe by other methods. On the surfaces of ordinary metals or semiconductors metastable atoms deexcite through resonance ionization (RI) followed by Auger neutralization (AN). In this case the deconvolution of electron spectra is necessary to obtain the electron distributions of occupied states. On the surfaces of insulators, on the other hand, metastable atoms deexcite through Auger deexcitation (AD, or Penning ionization (PI)), in which the relative intensity of electron spectra directly reflects the electron distribution of individual occupied states. On surfaces with very low work function (<2 eV) an alternate pathway involving intermediate negative ion formation may become dominant.

The information obtained by MAES is unique but rather qualitative compared to other electron spectroscopic techniques such as UPS, XPS, EELS, etc. This is due to the fact that the processes of electron emission from solid surfaces by metastables are more complicated than those by photons or electrons. Advances in the theoretical treatment are needed to derive quantitative information from metastable atom electron spectra, although a semiquantitative procedure for the simulation of the spectra is present.[84,85] Particularly, further theoretical studies are required to interpret the results of the observations involving electron spin such as the singlet-triplet conversion of helium metastables and spin-polarized MAES. The field of the surface study using metastable atoms is far from being mature and further interesting observations will appear in the near future.

VIII. References

(1) Penning, F. M. *Naturwissenshaften* **1927**, *15*, 818.
(2) Čermák, V. *J. Chem. Phys.* **1966**, *44*, 3781.
(3) Hotop, H. *Electronic and Atomic Collisions*; Oda, N., Takayanagi, K., Eds.; North-Holland: Amsterdam, 1980; p 271.
(4) Niehaus, A. *Adv. Chem. Phys.* **1981**, *45*, 399.
(5) Haberland, H.; Lee, Y. T.; Siska, P. E. *Adv. Chem. Phys.* **1981**, *45*, 487.
(6) Yencha, A. J. *Electron Spectroscopy: Theory, Techniques and Applications*; Brundle, C. R., Baker, A. D., Eds.; Academic: London, 1984; Vol. 5, p 197.
(7) Siska, P. E. *Comments At. Mol. Phys.* **1984**, *15*, 155.
(8) Beijerinck, H. C. W. *Comments At. Mol. Phys.* **1987**, *19*, 227.
(9) Morgner, H. *Comments At. Mol. Phys.* **1988**, *21*, 195.
(10) Harada, Y. *Pure Appl. Chem.* **1990**, *62*, 457.
(11) Niehaus, A. *Phys. Rep.* **1990**, *186*, 149.
(12) Ohno, K.; Harada, Y. *Theoretical Models of Chemical Bonding*; Maksic, Z. B., Ed.; Springer: Berlin, 1991; Part 3, p 199.
(13) Siska, P. E. *Rev. Mod. Phys.* **1993**, *65*, 337.
(14) Webb, H. W. *Phys. Rev.* **1924**, *24*, 113.
(15) Oliphant, M. L. E. *Proc. R. Soc. (London) A* **1929**, *124*, 228.
(16) Greene, D. *Proc. R. Soc. (London)* **1950**, *63*, 876.
(17) Stebbings, R. F. *Proc. R. Soc. (London) A* **1957**, *241*, 270.
(18) McLennan, D. A. *Phys. Rev.* **1966**, *148*, 218.
(19) Delchar, T. A.; McLennan, D. A.; Landers, A. M. *J. Chem. Phys.* **1969**, *50*, 1779.
(20) Dunning, F. B.; Smith, A. C. H.; Stebbings, R. F. *J. Phys. B* **1971**, *4*, 1683.
(21) Dunning, F. B.; Smith, A. C. H. *J. Phys. B* **1971**, *4*, 1696.
(22) Allison, W.; Dunning, F. B.; Smith, A. C. *J. Phys. B* **1972**, *5*, 1175.
(23) Shibata, T.; Hirooka, T.; Kuchitsu, K. *Chem. Phys. Lett.* **1975**, *30*, 241.
(24) Conrad, H.; Ertl, G.; Küppers, J.; Wang, S. W.; Gérard, K.; Haberland, H. *Phys. Rev. Lett.* **1979**, *42*, 1082.
(25) Boiziau, C.; Garot, C.; Nuvolone, R.; Roussel, J. *Surf. Sci.* **1980**, *91*, 313.
(26) Munakata, T.; Ohno, K.; Harada, Y. *J. Chem. Phys.* **1980**, *72*, 2880.
(27) Bozso, F.; Arias, J.; Yates, J. T., Jr.; Martin, R. M.; Metiu, H. *J. Chem. Phys.* **1983**, *78*, 4256.
(28) Hagstrum, H. D. *Phys. Rev. Lett.* **1979**, *43*, 1050.
(29) Hemmen, R.; Conrad, H. *Phys. Rev. Lett.* **1991**, *67*, 1314.
(30) Sesselmann, W.; Woratschek, B.; Ertl, G.; Küppers, J.; Haberland, H. *Surf. Sci.* **1983**, *130*, 245.
(31) Keller, W.; Morgner, H.; Müller, W. A. *Mol. Phys.* **1986**, *58*, 1039.
(32) Harada, Y. *Surf. Sci.* **1985**, *158*, 455.
(33) Ertl, G.; Küppers, J. *Low Energy Electrons and Surface Chemistry*, 2nd ed.; Verlag Chemie: Weinheim, 1985; p 147.
(34) Ertl, G. *Phil. Trans. R. Soc. (London) A* **1986**, *318*, 51.
(35) Harada, Y.; Ozaki, H. *Jpn. J. Appl. Phys.* **1987**, *26*, 1201.
(36) Hagstrum, H. D. *Chemistry and Physics of Solid Surfaces*; Fiermans, L., Vennik, J., Dekeyser, W., Eds.; Springer: Berlin, 1988; Vol. 7, p 341.
(37) Boiziau, C.; Dose, V.; Roussel, J. *Surf. Sci.* **1976**, *61*, 412.
(38) Conrad, H.; Ertl, G.; Küppers, J.; Sesselmann, W.; Haberland, H. *Surf. Sci.* **1982**, *121*, 161.
(39) Nishigaki, S.; Sugihara, M.; Ohara, M.; Fukui, S.; Matsuo, K.; Noda, T. *Jpn. J. Appl. Phys.* **1986**, *25*, L501.
(40) Chaban, E. E.; Hagstrum, H. D.; Petrie, P. *Rev. Sci. Instrum.* **1989**, *60*, 3647.
(41) Ishii, H.; Masuda, S.; Harada, Y. *Surf. Sci.* **1990**, *239*, 222.
(42) Maus-Friedrichs, W.; Dieckhoff, S.; Kempter, V. *Surf. Sci.* **1990**, *237*, 257.
(43) Capena, M.; Guarnaschelli, C.; Mattera, L.; Polese, M.; Terreni, S. *Rev. Sci. Instrum.* **1991**, *62*, 1431.
(44) Santo, K.; Hongo, S.; Saito, S.; Urano, T.; Kanaji, T. *Appl. Surf. Sci.* **1992**, *60/61*, 172.
(45) Morgner, H.; Oberbrodhage, J.; Richter, K.; Roth, K. *J. Phys.: Condens. Matter* **1991**, *3*, 5639.
(46) Morgner, H.; Oberbrodhage, J.; Richter, K. *Mol. Phys.* **1992**, *76*, 813.
(47) Harada, Y.; Masuda, S. Unpublished results.
(48) Leasure, E. L.; Mueller, C. R.; Ridley, T. Y. *Rev. Sci. Instrum.* **1975**, *46*, 635.
(49) Fahey, D. W.; Parks, W. F.; Schearer, L. D. *J. Phys. E* **1980**, *13*, 381.
(50) Hotop, H.; Niehaus, A.; Schmeltekopf, A. L. *Z. Phys.* **1969**, *229*, 1.
(51) Dunning, F. B.; Nordlander, P. *Nucl. Instrum. Methods Phys. Res., Sect. B* **1995**, *100*, 245 and references therein.
(52) Oró, D. M.; Soletsky, P. A.; Zhang, X.; Dunning, F. B.; Walters, G. K. *Phys. Rev. A* **1994**, *49*, 4703.
(53) Riddle, T. W.; Onellion, M.; Dunning, F. B.; Walters, G. K. *Rev. Sci. Instrum.* **1981**, *52*, 797.
(54) Recently P_z values of almost 1 have been obtained by use of diode lasers for optical pumping; see: Wallace, C. D.; Bixler, D. L.; Monroe, T. J.; Dunning, F. B.; Walters, G. K. *Rev. Sci. Instrum.*

1995, *66*, 265. Granitza, B.; Salvietti, M.; Torello, E.; Mattera, L. *Rev. Sci. Instrum.* **1995**, *66*, 4170.
(55) Burnett, G. C.; Monroe, T. J.; Dunning, F. B. *Rev. Sci. Instrum.* **1994**, *65*, 1893.
(56) Gray, L. G.; Hart, M. W.; Dunning, F. B.; Walters, G. K. *Rev. Sci. Instrum.* **1984**, *55*, 88.
(57) Čermák, V. *Collect. Czeck. Chem. Commun.* **1966**, *31*, 649.
(58) Miller, W. H. *J. Chem. Phys.* **1970**, *52*, 3563.
(59) Movre, M.; Meyer, N.; Merz, A.; Ruf, M.-W.; Hotop, H. *Chem. Phys. Lett.* **1994**, *230*, 276 and references therein.
(60) Merz, A.; Müller, M. W.; Ruf, M.-W.; Hotop, H.; Meyer, W.; Movre, M. *Chem. Phys. Lett.* **1989**, *160*, 377.
(61) Kimura, M.; Lane, N. F. *Phys. Rev. A* **1990**, *41*, 5938.
(62) Ohno, K.; Mutoh, H.; Harada, Y. *J. Am. Chem. Soc.* **1983**, *105*, 4555.
(63) Ohno, K.; Matsumoto, S.; Harada, Y. *J. Chem. Phys.* **1984**, *81*, 4447.
(64) Hotop, H.; Niehaus, A. *Z. Phys.* **1969**, *228*, 66.
(65) Hagstrum, H. D. *Electron and Ion Spectroscopy of Solids*; Fiermans, L., Vennik, J., Dekeyser, W., Eds.; Plenum: New York, 1978; p 273.
(66) Hagstrum, H. D.; Petrie, P.; Chaban, E. E. *Phys. Rev. B* **1988**, *38*, 10264.
(67) Sesselmann, W.; Woratschek, B.; Küppers, J.; Ertl, G.; Haberland, H. *Phys. Rev. B* **1987**, *35*, 1547.
(68) Hagstrum, H. D. *Phys. Rev.* **1966**, *150*, 495.
(69) Craig, J. H.; Dickinson, J. T. *J. Vac. Sci. Technol.* **1973**, *10*, 319.
(70) Boiziau, C.; Nuvolone, R.; Roussel, J. *Rev. Phys. Appl.* **1978**, *13*, 571.
(71) Titley, D. J.; Delchar, T. A. *Surf. Sci.* **1981**, *103*, 438.
(72) Titley, D. J.; Delchar, T. A.; Johnson, P. D. *Surf. Sci.* **1981**, *102*, L59.
(73) Boiziau, C.; Mucchielli, F.; Nuvolone, R.; Reynaud, C.; Roussel, J. *Surf. Sci.* **1981**, *102*, L63.
(74) Roussel, J.; Boiziau, C.; Nuvolone, R.; Reynaud, C. *Surf. Sci.* **1981**, *110*, L634.
(75) Conrad, H.; Doyen, G.; Ertl, G.; Küppers, J.; Sesselmann, W.; Haberland, H.*Chem. Phys. Lett.* **1982**, *88*, 281.
(76) Conrad, H.; Ertl, G.; Küppers, J.; Sesselmann, W.; Woratschek, B.; Haberland, H. *Surf. Sci.* **1982**, *117*, 98.
(77) Doyen, G. *Surf. Sci.* **1982**, *117*, 85.
(78) Hotop, H. Atomic, Molecular, and Optical Physics: Atoms and Molecules. In *Experimental Methods in the Physical Sciences*; Dunning, F. B., Hulet, R. G., Eds.; Academic: New York, 1996; Vol. 29B, p 191 and references therein.
(79) Swan, A.; Marynowski, M.; Franzen, W.; El-Batanouny, M.; Martini, K. M. *Phys. Rev. Lett.* **1993**, *71*, 1250.
(80) Swan, A.; Marynowski, M.; Franzen, W.; El-Batanouny, M.; Martini, K. M. *J. Vac. Sci. Technol. A* **1994**, *12*, 2219.
(81) Marynowski, M.; Franzen, W.; El-Batanouny, M.; Swan, A.; Martini, K. M. *Surf. Interface Anal.* **1995**, *23*, 105.
(82) Varga, P. *Comments At. Mol. Phys.* **1989**, *23*, 111. Andrä, H. J. *Physics of Highly Ionized Atoms*; Marrus, R., Ed.; NATO ASI Series B; Plenum: New York, 1989; p 377. Niehaus, A. *Phys. Rep.* **1990**, *186*, 149. Niehaus, A. *Ionization of Solids by Heavy Particles*; Baragiola, R. A., Ed.; NATO ASI Series B; Plenum: New York, 1993; p 66. Brenten, H.; Müller, H.; Kempter, V. *Ionization of Solids by Heavy Particles*; Baragiola, R. A., Ed.; NATO ASI Series B; Plenum: New York, 1993; p 105. Aumayr, F.; Winter, H. P. *Ionization of Solids by Heavy Particles*; Baragiola, R. A., Ed.; NATO ASI Series B; Plenum: New York, 1993; p 129 and references therein.
(83) Niehaus, A. *Chem. Phys.* **1994**, *179*, 183.
(84) Eken, P.; Fluit, J. M.; Niehaus, A.; Urazgil'din, I. *Surf. Sci.* **1992**, *273*, 160.
(85) Zeijlmans van Emmichoven, P. A.; Wouters, P. A. A. F.; Niehaus, A. *Surf. Sci.* **1988**, *195*, 115.
(86) Pülm, S.; Hitzke, A.; Günster, J.; Müller, H.; Kempter, V. *Radiat. Eff. Defects Solids* **1994**, *128*, 151.
(87) Hitzke, A.; Günster, J.; Kołaczkiewicz, J.; Kempter, V. *Surf. Sci.* **1994**, *318*, 139.
(88) Günster, J.; Mayer, Th.; Brause, M.; Maus-Friedrichs, W.; Busmann, H. G.; Kempter, V. *Surf. Sci.* **1995**, *336*, 341.
(89) Appelbaum, J. A.; Hamann, D. R. *Phys. Rev. B* **1972**, *6*, 1122.
(90) Schmidt, J.; Lucas, A. A. *Solid State Commun.* **1972**, *11*, 419.
(91) Hagstrum, H. D. *Phys. Rev.* **1954**, *96*, 336.
(92) Masuda, S.; Hayashi, H.; Harada, Y. *J. Electron Spectrosc. Relat. Phenom.* **1990**, *51*, 167.
(93) Masuda, S.; Hayashi, H.; Harada, Y. *Phys. Rev. B* **1990**, *42*, 3582.
(94) Masuda, S.; Harada, Y. *Surf. Sci.* **1993**, *283*, 78.
(95) Masuda, S; Aoki, M.; Harada, Y.; Hirohashi, M.; Watanabe, Y.; Sakisaka, Y.; Kato, H. *Phys. Rev. Lett.* **1993**, *71*, 4214.
(96) Roussel, J. *Phys. Scr.* **1983**, *T4*, 96.
(97) Lee, J.; Hanrahan, C.; Arias, J.; Bozso, F.; Martin, R. M.; Metiu, H. *Phys. Rev. Lett.* **1985**, *54*, 1440.
(98) Woratschek, B.; Sesselmann, W.; Küppers, J.; Ertl, G.; Haberland, H. *Phys. Rev. Lett.* **1985**, *55*, 611.
(99) Woratschek, B.; Sesselmann, W.; Küppers, J.; Ertl, G.; Haberland, H. *Surf. Sci.* **1987**, *180*, 187.
(100) Hemmen, R.; Conrad, H. *Appl. Phys. A* **1992**, *55*, 411.
(101) Brenten, H.; Müller, H.; Kempter, V. *Z. Phys. D* **1992**, *22*, 563.
(102) Böttcher, A.; Morgante, A.; Grobecker, R.; Greber, T.; Ertl, G. *Phys. Rev. B* **1994**, *49*, 10607.
(103) Makoshi, K.; Newns, D. M. *Surf. Sci.* **1985**, *159*, 149.
(104) Kasai, H.; Okiji, A. *Surf. Sci.* **1989**, *224*, 31.
(105) Nedeljkovic, N. N.; Nedeljkovic, Lj. D.; Janev, R. K. *Radiat. Eff. Defects Solids* **1989**, *109*, 91.
(106) Makoshi, K.; Yoshimori, A.; Lundqvist, B. I. *Surf. Sci.* **1990**, *230*, 350.
(107) Teillet-Billy, D.; Gauyacq, J. P. *Surf. Sci.* **1990**, *239*, 343.
(108) Yoshimori, A.; Makoshi, K. *Solid State Commun.* **1990**, *74*, 693.
(109) Makoshi, K. *Surf. Sci.* 1991, *254*, 281.
(110) Yoshimori, A. *Surf. Sci.* **1993**, *283*, 21.
(111) Borisov, A. G.; Teillet-Billy, D.; Gauyacq, J. P. *Surf. Sci.* **1993**, *284*, 337.
(112) Borisov, A. G.; Teillet-Billy, D.; Gauyacq, J. P. *Surf. Sci.* **1995**, *325*, 323.
(113) Makhmetov, G. E.; Borisov, A. G.; Teillet-Billy, D.; Gauyacq, J. P. *Surf. Sci.* **1995**, *339*, 182.
(114) Schultz, G. J. *Rev. Mod. Phys.* **1973**, *45*, 378.
(115) Müller, H.; Hausmann, R.; Brenten, H.; Niehaus, A.; Kempter, V. *Z. Phys. D* **1993**, *28*, 109.
(116) Lu, Q. B.; O'Connor, D. J.; King, B. V.; Shen, Y. G.; MacDonald, R. J. *Surf. Sci.* **1995**, *341*, 19.
(117) Aruga, T.; Murata, Y. *Prog. Surf. Sci.* **1989**, *31*. 61.
(118) Ishii, H. Thesis; Tokyo Univ., 1991.
(119) Masuda, S.; Ishii, H.; Harada, Y. *Solid State Commun.* **1991**, *79*, 453.
(120) Roussel, J.; Labois, E. *Surf. Sci.* **1980**, *92*, 561.
(121) Johnson, P. D.; Delchar, T. A. *Surf. Sci.* **1978**, *77*, 400.
(122) Johnson, P. D.; Delchar, T. A. *Surf. Sci.* **1979**, *82*, 237.
(123) Hammond, M. S.; Dunning, F. B.; Walters, G. K.; Prinz, G. A. *Phys. Rev. B* **1992**, *45*, 3674.
(124) Morgner, H.; Tackenberg, M. *Surf. Sci.* **1994**, *301*, 19.
(125) Onellion, M.; Hart, M. W.; Dunning, F. B.; Walters, G. K. *Phys. Rev. Lett.* **1984**, *52*, 380.
(126) Lee, J.; Arias, J.; Hanrahan, C.; Martin, R.; Metiu, H. *Surf. Sci.* **1985**, *159*, L460.
(127) Hart, M. W.; Hammond, M. S.; Dunning, F. B.; Walters, G. K. *Phys. Rev. B* **1989**, *39*, 5488.
(128) Dunning, F. B.; Nordlander, P.; Walters, G. K. *Phys. Rev. B* **1991**, *44*, 3246.
(129) Sesselmann, W.; Conrad, H.; Ertl, G.; Küppers, J.; Woratschek, B.; Haberland, H. *Phys. Rev. Lett.* **1983**, *50*, 446.
(130) Sesselmann, W.; Woratschek, B.; Küppers, J.; Ertl, G.; Haberland, H. *Phys. Rev. B* **1987**, *35*, 8348.
(131) Besenthal, K.; Chiarello, G.; Kordesch, M. E.; Conrad, H. *Surf. Sci.* **1986**, *178*, 667.
(132) Tochihara, H.; Rocker, G.; Martin, R. M.; Matiu, H.; Yates, J. T., Jr. *Surf. Sci.* **1988**, *203*, 44.
(133) Canepa, M.; Salvietti, M.; Campora, A.; Mattera, L. *J. Electron Spectrosc. Relat. Phenom.*, in press.
(134) Canepa, M.; Mattera, L.; Polese, M.; Terreni, S. *Chem. Phys. Lett.* **1991**, *177*, 123.
(135) Dunning, F. B.; Oró, D. M.; Soletsky, P. A.; Zhang, X.; Nordlander, P.; Walters, G. K. *Z. Phys. D* **1994**, *30*, 239.
(136) Cobas, A.; Lamb, W. E. *Phys. Rev.* **1944**, *65*, 327.
(137) Janev, R. K.; Nedeljkovic, N. N. *J. Phys. B* **1974**, *7*, 1506; **1981**, *14*, 2995; **1985**, *18*, 915.
(138) Hood, E.; Bozso, F.; Metiu, H. *Surf. Sci.* **1985**, *161*, 491.
(139) Penn, D. R.; Apell, P. *Phys. Rev. B* **1990**, *41*, 3303.
(140) (a) Salmi, L. A.; Monreal, R. M. C.; Apell, S. P. *Solid State Commun.* **1991**, *77*, 495. (b) Salmi, L. A. *Phys. Rev. B* **1992**, *46*, 4180.
(141) Hagstrum, H. D.; Becker, G. E. *Phys. Rev. B* **1971**, *4*, 4187.
(142) (a) Mularie, W. M.; Peria, W. T. *Surf. Sci.* **1971**, *26*, 125. (b) Tagle, J. A.; Martinez Saez, V.; Rojo, J. M.; Salmeron, M. *Surf. Sci.* **1978**, *79*, 77. (c) Martinez Saez, V. *J. Electron Spectrosc. Relat. Phenom.* **1979**, *17*, 33. (d) Szabo, P.; Roussel, G. J. *J. Electron Spectrosc. Relat. Phenom.* **1984**, *33*, 115.
(143) (a) Onsgaard, J. H.; Morgan, P. *J. Vac. Sci. Technol.* **1978**, *15*, 44. (b) Dose, V.; Scheidt, H. *Appl. Phys.* **1979**, *19*, 19.
(144) Masuda, S.; Ishii, H.; Harada, Y. *Solid State Commun.* **1992**, *82*, 587.
(145) Louie, S. G. *Phys. Rev. Lett.* **1979**, *42*, 476.
(146) Wimmer, E.; Freeman, A. J.; Krakauer, H. *Phys. Rev. B* **1984**, *30*, 3113.
(147) (a) Getzlaff, M.; Egert, D.; Rappolt, P.; Wilhelm, M.; Steidl, H.; Baum, G.; Raith, W. *J. Magn. Magn. Mater.* **1995**, *140−144*, 727. (b) Getzlaff, M.; Egert, D.; Rappolt, P.; Wilhelm, M.; Steidl, H.; Baum, G.; Raith, W. *Surf. Sci.* **1995**, *331−333*, 1404. (c) Salvietti, M.; Moroni, R.; Canepa, M.; Mattera, L. *J. Electron Spectrosc. Relat. Phenom.*, in press. (d) Getzlaff, M.; Egert, D.; Steidl, H.; Baum, G.; Raith, W. *Z. Phys. D* **1994**, *30*, 245.
(148) Oró D. M.; Lin, Q.; Soletsky, P. A.; Zhang, X.; Dunning, F. B.; Walters, G. K. *Phys. Rev. B* **1992**, *46*, 9893.
(149) Butler, W. H.; Oró, D. M.; Dunning, F. B.; Walters, G. K. *Surf. Sci.* **1992**, *261*, 382.
(150) Pasquali, L.; Fantini, P.; Nannarone, S.; Canepa, M.; Mattera, L. *J. Electron Spectrosc. Relat. Phenom.*, in press.

(151) Aoyama, M.; Masuda, S.; Ohno, K.; Harada, Y.; Mok, C. Y.; Huang, H. H.; Lee, L. S. *J. Phys. Chem.* **1989**, *93*, 1800.
(152) Masuda. S.; Aoyama, M.; Ohno, K.; Harada, Y. *Phys. Rev. Lett.* **1990**, *65*, 3257.
(153) Takami, T.; Mitsuke, K.; Ohno, K. *J. Chem. Phys.* **1991**, *95*, 918.
(154) Nishigaki, S.; Matsuda, S.; Sasaki, T.; Kawanishi, N.; Ikeda, Y.; Takeda, H. *Surf. Sci.* **1990**, *231*, 271.
(155) Masuda, S.; Ishii, H.; Harada, Y. *Surf. Sci.* **1991**, *242*, 400.
(156) Hongo, S.; Urano, T.; Kanaji, T. *Appl. Surf. Sci.* **1991**, *48/49*, 143.
(157) Ishii, H.; Masuda, S.; Harada, Y. *J. Electron Spectrosc. Relat. Phenom.* **1990**, *52*, 127.
(158) Ludviksson, A.; Xu, M.; Martin, R. M. *Surf. Sci.* **1992**, *277*, 282.
(159) Pasquali, L.; Plesanovas, A; Ruocco, A.; Tarabini, A. C.; Nannarone, S.; Canepa, M.; Mattera, L.; Terreni, S. *J. Electron Spectrosc. Relat. Phenom.* **1995**, *72*, 59.
(160) Aoki, M.; Masuda, S.; Harada, Y. Unpublished results.
(161) Takayanagi, K.; Tanishiro, Y.; Takahashi, M.; Takahashi, S. *J. Vac. Sci. Technol.* **1985**, *A3*, 1502; *Surf. Sci.* **1985**, *164*, 367.
(162) Wachs, A. L.; Miller. T.; Hsieh, T. C.; Shapiro, A. P.; Chaing, T. C. *Phys. Rev. B* **1985**, *32*, 2326 and references therein.
(163) Homers, R. J.; Tromps, R. M.; Demuth, J. E. *Phys. Rev. Lett.* **1986**, *56*, 1972.
(164) Hagstrum, H. D. *Phys. Rev.* **1961**, *122*, 83.
(165) Houston, J. E.; Moore, G.; Lagally, M. G. *Solid State Commun.* **1977**, *21*, 879.
(166) Nishigaki, S.; Takao, K.; Yamada, T.; Arimoto, M.; Komatsu, T. *Surf. Sci.* **1985**, *158*, 473.
(167) Fuggle, J. C. *Electron Spectroscopy: Theory, Techniques and Applications*; Brundle, C. R., Becker, A. D., Eds.; Academic: New York, 1981; Vol. 4, p 86.
(168) McGovern, I. T.; Williams, R. H.; Parke, A. W. *J. Phys. C* **1979**, *12*, 2689 and references therein.
(169) Abbati, I.; Braicovich, L.; Carbone, C.; Nogami, J.; Yeh, J. J.; Lindau, I.; del Pennino, U. *Phys. Rev. B* **1985**, *32*, 5459.
(170) Huisman, R.; de Jonge, R.; Haas, C.; Jellinek, F. *J. Solid State Chem.* **1971**, *3*, 56.
(171) Munakata, T.; Harada, Y.; Ohno, K.; Kuchitsu, K. *Chem. Phys. Lett.* **1981**, *84*, 6.
(172) Masuda, S.; Aoyama, S.; Harada, Y. *J. Am. Chem. Soc.* **1990**, *112*, 6445.
(173) Takahashi, T.; Tokailin, H.; Sagawa, T. *Solid State Commun.* **1984**, *52*, 765 and references therein.
(174) Frétigny, C.; Saito, R.; Kamimura, H. *J. Phys. Soc. Jpn.* **1989**, *58*, 2098.
(175) Munakata, T.; Hirioka, T.; Kuchitsu, K. *J. Electron Spectrosc. Relat. Phenom.* **1980**, *18*, 51.
(176) Maus-Friedrichs, W.; Dieckhoff, S.; Kempter, V. *Surf. Sci.* **1991**, *253*, 137.
(177) Dieckhoff, S.; Müller, H.; Maus-Friedrichs, W.; Brenten, H.; Kempter, V. *Surf. Sci.* **1992**, *279*, 233.
(178) Hitzke, A.; Pülm, S.; Müller, H.; Günster, J.; Hausmann, R.; Dieckhoff, S.; Maus-Friedrichs, W.; Kempter, V. *Surf. Sci.* **1993**, *291*, 67.
(179) Pülm, S.; Hitzke, A.; Günster, J.; Maus-Friedrichs, W.; Kempter, V. *Surf. Sci.* **1995**, *325*, 75.
(180) Masuda, S. *J. Electron Spectrosc. Relat. Phenom.* **1995**, *76*, 359.
(181) Vogt, B.; Kessler, B.; Müller, N.; Schönhense, G.; Schmiedeskamp, B.; Heizmann, U. *Phys. Rev. Lett.* **1991**, *67*, 1318 and references therein.
(182) Ebding, T.; Niehaus, A. *Z. Phys.* **1974**, *270*, 43.
(183) Yencha, A. J.; Kubota, H.; Fukuyama, T.; Kondow, T.; Kuchitsu, K. *J. Electron Spectrosc. Relat. Phenom.* **1981**, *23*, 431.
(184) Oró, D. M.; Lin, Q.; Zhang, X.; Dunning, F. B.; Walters, G. K. *J. Chem. Phys.* **1992**, *97*, 7743.
(185) Hotop, H.; Niehaus, A. *Int. J. Mass Spectrom. Ion Phys.* **1970**, *5*, 415.
(186) Yee, D. S. C.;Stewart, W. B.; MacDowell, C. A.; Brion, C. E. *J. Electron Spectrosc. Relat. Phenom.* **1975**, *7*, 93.
(187) Čermák, V. *Electron Spectrosc. Relat. Phenom.* **1976**, *9*, 419.
(188) Rutherford, G. H.; Soletsky, P. A.; Bryan, W. H.; Dunning, F. B.; Walters, G. K. *Phys. Rev. A* **1992**, *46*, 230.
(189) Ohno, K.; Hoshino, S.; Yamakado, H.; Kishimoto, N.; Takami, T.; Ogawa, T. To be published.
(190) Harada, Y.; Ohno, K.; Mutoh, H. *J. Chem. Phys.* **1983**, *79*, 3251.
(191) Masuda, S; Harada, Y. *J. Chem. Phys.* **1992**, *96*, 2469.
(192) Cotton, F. A.; Wilkinson, G. *Advanced Inorganic Chemistry*, 3rd ed.; Wiley-Interscience: New York, 1972.
(193) Johnson, B. J.; Klemperer, W. G. *J. Am. Chem. Soc.* **1976**, *99*, 7918.
(194) See, for example: Plummer, E. W.; Salaneck, W. R.; Miller, J. S. *Phys. Rev. B* **1978**, *18*, 1673.
(195) Bozso, F.; Yates, J. T., Jr.; Arias, J.; Martin, R. M.; Metiu, H. *Chem. Phys. Lett.* **1983**, *94*, 243.
(196) Bozso, F.; Arias, J.; Hanrahan, C.; Martin, R. M.; Yates, J. T., Jr.; Metiu, H. *Surf. Sci.* **1984**, *136*, 257.
(197) Lee, J.; Arias, J.; Hanrahan, C. P.; Martin, R. M.; Metiu, H. *J. Chem. Phys.* **1985**, *82*, 485.
(198) Sesselmann, W.; Woratschek, B.; Ertl, G.; Küppers, J.; Haberland, H. *Surf. Sci.* **1984**, *146*, 17.
(199) Mucchielli, F.; Boiziau, C.; Nuvolone, R.; Roussel, J. *J. Phys. C: Solid State Phys.* **1980**, *13*, 2441.
(200) Rocker, G.; Tochihara, H.; Martin, R. M.; Metiu, H. *Surf. Sci.* **1987**, *181*, 509.
(201) Maus-Friedrichs, W.; Dieckhoff, S.; Kempter, V. *Surf. Sci.* **1991**, *249*, 149.
(202) Lee, J.; Hanrahan, C. P.; Arias, J.; Martin, R. M.; Metiu, H. *Phys. Rev. Lett.* **1983**, *51*, 1803.
(203) Lee, J.; Arias, J.; Hanrahan, C.; Martin, R. M.; Metiu, H. *Phys. Rev. Lett.* **1983**, *51*, 1991.
(204) Arias, J.; Lee, J.; Dunaway, J.; Martin, R. M.; Metiu, H. *Surf. Sci.* **1985**, *159*, L433.
(205) Jänsch, H. J.; Huang, C.; Ludviksson, A.; Redding, J. D.; Metiu, H.; Martin, R. M. *Surf. Sci.* **1989**, *222*, 199.
(206) Rocker, G. H.; Cobb, C. L.; Huang, C.; Tochihara, H.; Metiu, H.; Martin, R. M. *Surf. Sci.* **1989**, *222*, 181.
(207) Rocker, G. H.; Huang, C.; Cobb, C. L.; Metiu, H.; Martin, R. M. *Surf. Sci.* **1991**, *244*, 103.
(208) Mariani, C.; Middelmann, H. U.; Iwan, M.; Horn, K. *Chem. Phys. Lett.* **1982**, *93*, 308 and references therein.
(209) Wang, S. W.; Ertl, G. *Surf. Sci.* **1980**, *93*, L75. Wang, S. W. *J. Vac. Sci. Technol.* **1982**, *20*, 600.
(210) Takeishi, Y; Hagstrum, H. D. *Phys. Rev.* **1969**, *137*, A641.
(211) Rosén, A.; Baerends, E. J.; Ellis, D. E. *Surf. Sci.* **1979**, *82*, 139.
(212) Blyholder, G. *J. Chem. Phys.* **1964**, *68*, 2772; *J. Vac. Sci. Technol.* **1974**, *11*, 865.
(213) Kuhlenbeck, H.; Saalfeld, H. B.; Buskotte, U.; Neumann, M.; Freund, H. J.; Plummer, E. W. *Phys. Rev. B* **1989**, *39*, 3475.
(214) Newn, D. M. *Phys. Rev.* **1969**, *178*, 1123. Muscat, J. P.; Newns, D. M. *Prog. Surf. Sci.* **1978**, *9*, 1. Muscat, J. P. *Prog. Surf. Sci.* **1985**, *18*, 59.
(215) Gumhalter, B.; Wandelt, K.; Avouris, Ph. *Phys. Rev.* **1988**, *37*, 8048. Avouris, Ph. *Phys. Scr.* **1987**, *35*, 47.
(216) Drakova, D.; Doyen, G. *Phys. Rev. B* **1994**, *50*, 4701.
(217) Edquist, O.; Åsbrink, L.; Lindholm, E. *Z. Naturforsch.* **1971**, *26a*, 1407.
(218) Hotop, H.; Kolb, E.; Lorenzen, J. *J. Electron Spectrosc. Relat. Phenom.* **1979**, *16*, 213.
(219) Hotop, H. Dissertation, Freiburg, 1971.
(220) Bozso, F.; Arias, J.; Hanrahan, C. P.; Yates, J. T., Jr.; Martin, R. M.; Metiu, H. *Surf. Sci.* **1984**, *141*, 591.
(221) Sesselmann, W.; Woratschek, B.; Küppers, J.; Doyen, G.; Ertl, G.; Haberland, H.; Morgner, H. *Phys. Rev. Lett.* **1988**, *60*, 1434.
(222) Jänsch, H. J.; Huang, C.; Ludviksson, A.; Rocker, G.; Redding, J. D.; Metiu, H.; Martin, R. M. *Surf. Sci.* **1989**, *214*, 377.
(223) Drakova, D.; Doyen, G. *Phys. Rev. B* **1994**, *49*, 13787.
(224) Yoshimori, *Surf. Sci.* **1995**, *342*, L1101.
(225) Rocker, G. H.; Cobb, C. L.; Jun, C. S.; Metiu, H.; Martin, R. M. *Surf. Sci.* **1989**, *208*, 205.
(226) Greuter, F.; Eberhardt, W.; DiNardo, J.; Plummer, E. W. *J. Vac. Sci. Technol.* **1981**, *18*, 433. Eberhardt, W.; Greuter, F.; Plummer, E. W. *Phys. Rev. Lett.* **1981**, *46*, 1085.
(227) Conrad, H.; Ertl, G.; Küppers, J.; Sesselmann, W.; Haberland, H. *Surf. Sci.* **1980**, *100*, L461.
(228) Lee, J.; Hanrahan, C. P.; Arias, J.; Martin, R. M.; Metiu, H. *Surf. Sci.* **1985**, *161*, L543.
(229) Woratschek, B.; Sesselmann, W.; Küppers, J.; Ertl, G.; Haberland, H. *Phys. Rev. Lett.* **1985**, *55*, 1231.
(230) Nishigaki, S.; Ohara, M.; Murakami, A.; Fukui, S.; Matsuda, S. *Appl. Surf. Sci.* **1988/89**, *35*, 121.
(231) Nishigaki, S.; Oishi, N.; Matsuda, S.; Kawanishi, N.; Sasaki, T. *Phys. Rev. B* **1989**, *39*, 8048.
(232) Greber, T.; Freihube, K.; Grobecker, R.; Böttcher, A.; Hermann, K.; Ertl, G. *Phys. Rev. B* **1994**, *50*, 8755.
(233) Diekholff, S.; Maus-Friedrichs, W.; Kempter, V. *Nucl. Instrum. Methods Phys. Res., Sect. B* **1992**, *65*, 488.
(234) Brenten, H.; Müller, H.; Maus-Friedrichs, W.; Dieckhoff, S.; Kempter, V. *Surf. Sci.* **1992**, *262*, 151.
(235) Maus-Friedrichs, W.; Dieckhoff, S.; Kempter, V. *Surf. Sci.* **1992**, *273*, 311.
(236) Maus-Friedrichs, W.; Dieckhoff, S.; Wehrhahn, M.; Pülm, S.; Kempter, V. *Surf. Sci.* **1992**, *271*, 113.
(237) Günster, J.; Brause, M.; Mayer, Th.; Hitzke, A.; Kempter, V. *Nucl. Instrum. Methods Phys. Res., Sect. B* **1993**, *100*, 411.
(238) Kubiak, R.; Morgner, H.; Rakhovskaya, O. *Surf. Sci.* **1994**, *321*, 229.
(239) Bozso, F.; Hanrahan, C. P.; Arias, J.; Metiu, H.; Yates, J. T., Jr.; Martin, R. M. *Surf. Sci.* **1983**, *128*, L197.
(240) Bozso, F.; Arias, J. M.; Hanrahan, C. P.; Yates, J. T., Jr.; Metiu, H.; Martin, R. M. *Surf. Sci.* **1984**, *138*, 488.
(241) Tochihara, H.; Rocker, G.; Redding, J. D.; Yates, J. T., Jr.; Metiu, H.; Martin, R. M. *Surf. Sci.* **1986**, *176*, 1.
(242) Lee, J.; Arias, J.; Hanrahan, C.; Martin, R. M.; Metiu, H. *Surf. Sci.* **1986**, *165*, L95.
(243) Hoffmann, F. M.; Rocker, G.; Tochihara, H.; Martin, R. M.; Matiu, H. *Surf. Sci.* **1988**, *205*, 397.
(244) Rocker, G. H.; Huang, C.; Cobb, C. L.; Redding, J. D.; Metiu, H.; Martin, R. M. *Surf. Sci.* **1991**, *250*, 33.
(245) Nooney, M.; Liberman, V.; Xu, M.; Lundviksson, A.; Martin, R. M. *Surf. Sci.* **1994**, *302*, 192.

(246) Nishigaki, S.; Sasaki, T.; Matsuda, S.; Kawanishi, N.; Takeda, H.; Yamada, Y. *Surf. Sci.* **1991**, *242*, 358.
(247) Woratschek, B.; Ertl, G.; Küppers, J.; Sesselmann, W.; Haberland, H. *Phys. Rev. Lett.* **1986**, *57*, 1484.
(248) Woratschek, B.; Sesselmann, W.; Küppers, J.; Ertl, G.; Haberland, H. *J. Chem. Phys.* **1987**, *86*, 2411.
(249) Hemmen, R.; Kordesch, M. E.; Conrad, H. *Surf. Sci.* **1989**, *211/212*, 857.
(250) Böttcher, A.; Grobecker, R.; Imbeck, R.; Morgante, A.; Ertl, G. *J. Chem. Phys.* **1991**, *95*, 3756.
(251) Böttcher, A.; Grobecker, R.; Greber, T.; Morgante, A.; Ertl, G. *Surf. Sci.* **1993**, *280*, 170.
(252) Grobecker, R.; Shi, H.; Bludau, H.; Hertel, T.; Greber, T.; Böttcher, A.; Jacobi, K.; Ertl, G. *Phys. Rev. Lett.* **1994**, *72*, 578.
(253) Böttcher, A.; Imbeck, R.; Morgante, A.; Ertl, G. *Phys. Rev. Lett.* **1990**, *65*, 2035.
(254) Canepa, M.; Cantini, P.; Mattera, L.; Terreni, S.; Valdenazzi, F. *Phys. Scr. T.* **1992**, *41*, 226.
(255) Canepa, M.; Cantini, P.; Mattera, L.; Narducci, E.; Salvietti, M.; Terreni, S. *Surf. Sci.* **1995**, *322*, 271.
(256) Nørskof, J. K.; Newns, D. M.; Lundqvist, B. I. *Surf. Sci.* **1979**, *80*, 179.
(257) Munakata, T.; Hirooka, T.; Kuchitsu, K. *J. Electron Spectrosc. Relat. Phenom.* **1978**, *13*, 219.
(258) Kubota, H.; Munakata, T.; Hirooka, T.; Kuchitsu, K.; Harada, Y. *Chem. Phys. Lett.* **1980**, *74*, 409.
(259) Kubota, H.; Hirooka, T.; Fukuyama, T.; Kondow, T.; Kuchitsu, K.; Yencha, A. J. *J. Electron Spectrosc. Relat. Phenom.* **1981**, *23*, 417.
(260) Ohno, K.; Mutoh, H.; Harada, Y. *Surf. Sci.* **1982**, *115*, L128.
(261) Reynaud, C.; Juret, C.; Boiziau, C. *Surf. Sci.* **1982**, *126*, 733.
(262) Reynaud, C.; Boiziau, C.; Lecayon, G.; Le Gressus, C. *Scanning Electron Microsc.* **1982**, 961.
(263) Reynaud, C.; Richard, A.; Juret, C.; Nuvolone, R.; Boiziau, C.; Lecayon, G.; Le Gressus, C. *Thin Solid Films* **1982**, *92*, 355.
(264) Harada, Y.; Ozaki, H.; Ohno, K. *Phys. Rev. Lett.* **1984**, *52*, 2269.
(265) Harada, Y.; Ozaki, H.; Ohno, K.; Kajiwara, T. *Surf. Sci.* **1984**, *147*, 356.
(266) Kubota, H.; Munakata, T.; Hirooka, T.; Kondow, T.; Kuchitsu, K.; Ohno, K.; Harada, Y. *Chem. Phys.* **1984**, *87*, 399.
(267) Suzuki, T.; Hirooka, T.; Kondow, K.; Kuchitsu, K. *Surf. Sci.* **1985**, *158*, 515.
(268) Perreau, J.; Reynaud, C.; Boiziau, C.; Lécayon, G.; Makram, C.; Le Gressus, C. *Surf. Sci.* **1985**, *162*, 776.
(269) Lee, J.; Hanrahan, C.; Arias, J.; Martin, R. M.; Metiu, H. *Phys. Rev. B* **1985**, *32*, 8216.
(270) Harada, Y.; Masuda, S.; Ozaki, H. *Oyo Buturi [Appl. Phys.]* **1986**, *55*, 863.
(271) Perreau, J.; Reynaud, C.; Boiziau, C.; Lécayon, G. *Ann. Phys. (Paris)* **1986**, *11* (*1, Suppl. Journ. Films Org. Modif. Surf. Propr. Induites*), 71.
(272) Perreau, J.; Reynaud, C.; Lécayon, G.; Ellinger, Y. J. *Phys. B: At. Mol. Phys.* **1986**, *19*, 1497.
(273) Ozaki, H.; Harada, Y. *J. Am. Chem. Soc.* **1987**, *109*, 949.
(274) Ozaki, H.; Harada, Y.; Nishiyama, K.; Fujihira, M. *J. Am. Chem. Soc.* **1987**, *109*, 950.
(275) Mitsuya, M.; Ozaki, H.; Harada, Y.; Seki, K.; Inokuchi, H. *Langmuir* **1988**, *4*, 569.
(276) Suzuki, T.; Suzuki, K.; Kondow, T.; Kuchitsu, K. *J. Phys. Chem.* **1988**, *92*, 3953.
(277) Harada, H.; Hayashi, H.; Ozaki, H.; Kamata, T.; Umemura, J.; Takenaka, T. *Thin Solid Films* **1989**, *178*, 305.
(278) Ozaki, H.; Harada, Y. *J. Chem. Phys.* **1990**, *92*, 3184.
(279) Ozaki, H.; Harada, Y. *J. Am. Chem. Soc.* **1990**, *112*, 5735.
(280) Harada, Y.; Hayashi, H.; Masuda, S.; Fukuda, T.; Sato, N.; Kato, S.; Kobayashi, K.; Kuroda, H.; Ozaki, H. *Surf. Sci.* **1991**, *242*, 95.
(281) Masuda, S.; Hayashi, H.; Harada, Y.; Kato, S. *Chem. Phys. Lett.* **1991**, *180*, 279.
(282) Ozaki, H.; Mori, S.; Miyashita, T.; Tsuchiya, T.; Mazaki, Y.; Aoki, M.; Masuda, S.; Harada, Y.; Kobayashi, K. *J. Electron Spectrosc. Relat. Phenom.* **1994**, *68*, 531.
(283) Harada, Y.; Yamamoto, S.; Aoki, M.; Masuda, S.; Ichinokawa, T.; Kato, M.; Sakai, Y. *Nature* **1994**, *372*, 657.
(284) Brückner, M.; Heinz, B.; Morgner, H. *Surf. Sci.* **1994**, *319*, 370.
(285) Ozaki, H.; Funaki, T.; Mazaki, Y.; Masuda, S.; Harada, Y. *J. Am. Chem. Soc.* **1995**, *117*, 5596.
(286) Ozaki, H.; Kasuga, M.; Tsuchiya, T.; Funaki, T.; Mazaki, Y.; Aoki, M.; Masuda, S.; Harada, Y. *J. Chem. Phys.* **1995**, *103*, 1226.
(287) Aoki, M.; Masuda, S.; Einaga, Y.; Kamiya, K.; Ueno, N.; Harada, Y. *Mol. Cryst. Liq. Cryst.* **1995**, *267*, 217
(288) Pasinszki, T.; Aoki, M.; Masuda, S.; Harada, Y.; Ueno, N.; Hoshi, H.; Maruyama, Y. *J. Phys. Chem.* **1995**, *99*, 12858.
(289) Ozaki, H. *J. Electron Spectrosc. Relat. Phenom.* **1995**, *76*, 377.
(290) Aoki, M.; Masuda, S.; Einaga, Y.; Kamiya, K.; Kitamura, A.; Momose, M.; Ueno, N.; Harada, Y.; Miyazaki, T.; Hasegawa, S.; Inokuchi, H.; Seki, K. *J. Electron Spectrosc. Relat. Phenom.* **1995**, *76*, 259.
(291) Ozaki, H.; Harada, Y. To be published.
(292) Ozaki, H. Thesis; Tokyo Univ., 1987.
(293) Keller, W.; Morgner, H.; Müller,W. A. *Mol. Phys.* **1986**, 57, 623.
(294) Keller, W.; Morgner, H.; Müller, W. A. *Electronic and Atomic Collisions*; Lorents, D. C., Meyerhof, W. E., Peterson, J. R., Eds.; Elsevier: Amsterdam, 1986.
(295) Morgner, H.; Oberbrodhage, J.; Richter, K.; Roth, K. *Mol. Phys.* **1991**, *73*, 1295.
(296) Morgner, H.; Oberbrodhage, J.; Richter, K.; Roth, K. *J. Electron Spectrosc. Relat. Phenom.* **1991**, *57*, 61.
(297) Morgner, H.; Oberbrodhage, J.; Wulf, W. *J. Electron Spectrosc. Relat. Phenom.* **1993**, *61*, 183.
(298) Morgner, H.; Richter, K.; Wulf, M. *Mol. Phys.* **1993**, *79*, 169.
(299) Morgner, H.; Wulf, M. *J. Electron Spectrosc. Relat. Phenom.* **1995**, *74*, 91.
(300) Gaines, G. L., Jr. *Insoluble Monolayers at Liquid-Gas Interfaces*; Wiley-Interscience: New York, 1966.
(301) Fukuda, K.; Nakahara, H.; Kato, T. *J. Colloid Interface Sci.* **1976**, *54*, 430.
(302) Kjems, J. K.; Passell, L.; Taub, H.; Dash, J. G.; Navaco, A. D. *Phys. Rev. B* **1976**, *13*, 1446.
(303) Firment, L. E.; Somorjai, G. A. *J. Chem. Phys.* **1977**, *66*, 2901.
(304) Firment, L. E.; Somorjai, G. A. *J. Chem. Phys.* **1978**, *69*, 3940.
(305) Sato, N.; Seki, K.; Inokuch, H. *J. Chem. Soc., Faraday Trans. 2* **1981**, *77*, 1621.
(306) Seki, K.; Ueno, N.; Karlsson, U. O.; Engelhardt, R.; Koch, E. E. *Chem. Phys.* **1986**, *105*, 247 and references therein.
(307) Seki, H.; Hashimoto, S.; Sato, N.; Harada, Y.; Ishii, K.; Inokuchi, H.; Kanbe, J. *J. Chem. Phys.* **1977**, *66*, 3644.
(308) Hashimoto, S.; Seki, K.; Sato, N.; Inokuch, H. *J. Chem. Phys.* **1982**, *76*, 163.
(309) Kamata, T.; Umemura, J.; Takenaka, T. *Chem. Lett.* **1988**, 1231.
(310) Maruyama, Y.; Iwasaki, N. *Chem. Phys. Lett.* **1974**, *24*, 26.
(311) Müller, H.; Bässler, H.; Vaubel, G. *Chem. Phys. Lett.* **1974**, *29*, 102.
(312) Kamura, Y.; Seki, K.; Inokuchi, H. *Chem. Phys. Lett.* **1975**, *30*, 35.
(313) Lee, K. O.; Gan, T. T. *Chem. Phys. Lett.* **1977**, *51*, 120.
(314) Bastianssen, O.; Traetteberg, M. *Tetrahedron* **1962**, *17*, 147.
(315) Höchst, H.; Goldmann, A.; Hüfner, S.; Malter, H. *Phys. Status Solidi B* **1976**, *76*, 559.
(316) Battye, F. L.; Goldmann, A.; Kasper, L. *Phys. Status Solidi B* **1977**, *80*, 425.
(317) Koch, E. E.; Grobman, W. D. *J. Chem. Phys.* **1977**, *67*, 837.
(318) Iwan, M.; Eberhardt, W.; Kalkoffen, G.; Koch, E. E.; Kunz, C. *Chem. Phys. Lett.* **1979**, *62*, 344.
(319) Berkowitz, J. *J. Chem. Phys.* **1979**, *70*, 2819.
(320) Permien, T.; Engelhardt, R.; Feldmann, C. A.; Koch, E. E. *Chem. Phys. Lett.* **1983**, *98*, 527.
(321) Khandelwal, S. C.; Roebber, J. L. *Chem. Phys. Lett.* **1975**, *34*, 355.
(322) Kitagawa, S.; Morishima, I.; Yonezawa, T.; Sato, N. *Inorg. Chem.* **1979**, *18*, 1345.
(323) Almlöf, J. *Int. J. Quantum Chem.* **1974**, *8*, 915.
(324) Spangler, D.; Maggiora, G. M.; Shipman, L. L.; Christoffersen, R. E. *J. Am. Chem. Soc.* **1977**, *99*, 7470; 7478.
(325) Kashiwagi, H.; Obara, S. *Int. J. Quantum Chem.* **1981**, *20*, 843.
(326) Sakai, Y.; Kato, M.; Masuda, S.; Harada, Y.; Ichinokawa, T. *Surf. Sci.* **1995**, *336*, 295.
(327) Yamamoto, S.; Masuda, S.; Yasufuku, H.; Ueno, N.; Harada, Y.; Ichinokawa, T.; Kato, M.; Sakai, Y. *J. Appl. Phys.* **1987**, *82*, in press.

CR940315V